Development of Electrostatic Actuation Techniques for Close-Proximity Formation Flying in Low Earth Orbit Plasma Wakes

by

Jordan H. Maxwell

B.S., Montana State University,

Bozeman, Montana, 2015

M.S., University of Colorado Boulder,

Boulder, Colorado, 2018

Doctoral committee members: Prof. Hanspeter Schaub, Prof. Jay McMahon, Prof. Zoltan Sternovsky, Prof. Dale Ferguson, Prof. Jeffrey Thayer

A thesis submitted to the

Faculty of the Graduate School of the

University of Colorado in partial fulfillment

of the requirements for the degree of

Doctor of Philosophy

Anne and H.J. Smead Department of Aerospace Engineering Sciences

2020

Maxwell, Jordan H. (Ph.D., Aerospace Engineering Sciences)

Development of Electrostatic Actuation Techniques for Close-Proximity Formation Flying in Low Earth Orbit Plasma Wakes

Thesis directed by Prof. Hanspeter Schaub

Electrostatic actuation is a highly fuel and power efficient technique which applies Coulomb forces and torques between close-proximity charged spacecraft to achieve desired relative motion. The technology is most applicable to Geosynchronous Equatorial Orbit (GEO) spacecraft, as the plasma environment in that regime is amenable. However, the fiscal and access challenges in launching an untested technology into GEO motivates demonstration of the technique in a representative environment. This dissertation demonstrates the feasibility of a technology demonstration in Low Earth Orbit (LEO) plasma wakes.

An initial investigation of electrostatic interactions between close-proximity objects in motion is undertaken. The Multi-Sphere Method (MSM) shown to accurately replicate electric fields of static systems is investigated for application to time varying geometries. An MSM model is initialized for a prototypical shape and is deformed significantly without reinitialization. Analytic expressions for the capacitance and electric fields are compared with the MSM model and it is shown that shape change is well-modeled without MSM reconfiguration unless MSM spheres come in close proximity.

With a model for Coulomb interactions between spacecraft, the plasma effects in LEO are considered. Through extensive simulations with the Nascap-2k spacecraft charging code, it is determined that small negative potentials should be applied for electrostatic actuation in LEO wakes. Experiments are described providing insight into wake shaping techniques which apply positively charged sparse structures to expand the working volume for electrostatic actuation in LEO. Improved experimental facility design for such investigations is described in detail.

Finally, four controllers are derived to bring a close-proximity leader-follower formation to rest using electrostatic actuation. A conventional control approach is initially applied with significant challenges resulting from nonlinear Coulomb force interactions. Two additional controls designed to mitigate these challenges are presented, but prove highly sensitive to noise and reference trajectory design. A final controller is presented that improves upon those before. A rendezvous scenario between a cubesatellite and the ISS is considered feasible given results gleaned from orbit control and Nascap-2k simulations.

Acknowledgements

I would first like to thank my advisor, Dr. Hanspeter Schaub, for his guidance and mentorship. His willingness to support research outside his field allowed me to follow my passions and interest. Throughout this degree, Dr. Schaub has always pushed me improve as a researcher, an engineer, and a communicator. The experience of teaching Spacecraft Attitude, Dynamics, and Control under his tutelage is one I will cherish. Thanks also to my committee members Dr. Jay McMahon, Dr. Zoltan Sternovsky, Dr. Dale Ferguson, and Dr. Jeffrey Thayer for their support and guidance with this project.

I would also like to acknowledge Miles Bengtson for several years of engaging physics conversations and chamber work sessions. He was a great sounding board for any research obstacle I was facing and an excellent research partner during our months at AFRL. Ryan Hoffmann's and Dan Engelhart's mentorship during this time and their help since has proven invaluable. Without their mentorship and assistance, this project could not have been completed.

It has been a pleasure working with the researchers in the AVS lab and in CCAR. I am lucky to have been encouraged by my classmates, coworkers, and professors throughout this experience. I want to thank my friends in Colorado and elsewhere for a lifetime of support.

Finally I would like to thank my family. Thanks to my brothers, Hayden and Kaleb, for putting up with me working frantically during our vacations; to my sister Jessica for always looking out for and supporting me; and to my parents Hugh and Lori for giving me the opportunities that have enabled me to achieve this. I love you all.

Contents

Tables

Table

Figures

Figure

Chapter 1

Introduction

1.1 Motivation

In recent years, a method called electrostatic actuation has been developed to facilitate on-orbit proximity operations in Geosynchronous Equatorial Orbit (GEO). The technique utilizes induced charge distributions on objects' surfaces to generate Coulomb forces and torques to affect relative position and attitude between nearby craft. This technology has the key benefits of being touchless, using virtually no fuel, and being capable of despinning an object as depicted in Figure 1.1.[15] These are significant advantages over modern actuation techniques especially in the contexts of debris mitigation and long-term maintenance of spaceborne structures and formations.

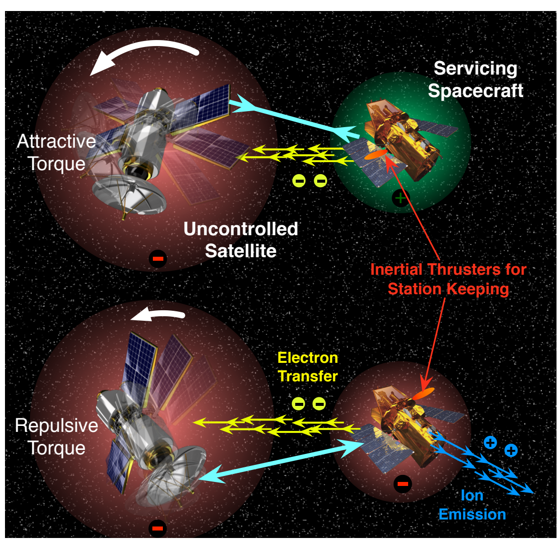

Figure 1.1: Electrostatic detumble of uncooperative spinning spacecraft. Image from reference [15]

Figure 1.1 illustrates a hybrid approach to stabilize a tumbling spacecraft. A servicer charges itself and the tumbling craft to desired potentials via charged particle beams to generate stabilizing Coulomb forces and torques. The servicer maintains the desired relative position and attitude against the equal-and-opposite Coulomb force using inertial thrusters. The lack of any mechanical grappling system reduces the risk inherent in interacting with a tumbling spacecraft.

Many additional electrostatic actuation applications have been developed in recent years, including the GEO Large Debris Reorbiter mission concept illustrated in Figure 1.2.[76] A hybrid approach is again applied, this time to raise GEO debris into a graveyard orbit.

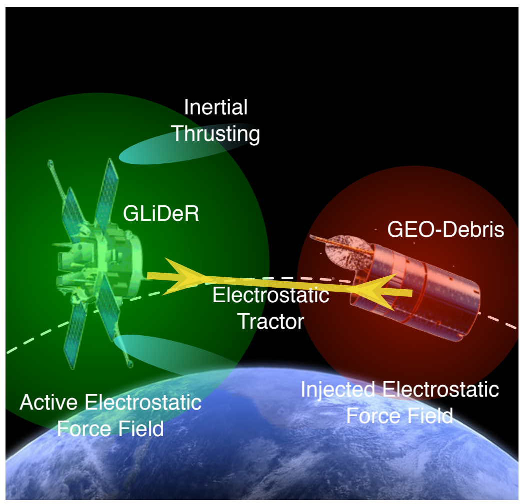

Figure 1.2: Electrostatic reorbit of uncooperative debris object. Image from reference [76]

A major challenge to application of electrostatic actuation are the many practical, legal, and financial obstacles to launching any novel actuation technique for spacecraft control. This is especially true of spacecraft launched into GEO. While a wealth of publications on simulated applications of electrostatic actuation in this regime exist, only terrestrial experiments in standard atmospheric conditions have demonstrated the technique.

A key step in establishing the Technology Readiness Level (TRL) of electrostatic actuation is demonstration in a relevant environment.[51] The extreme difficulty in replicating the low density, high energy plasma representative of GEO terrestrially therefore proves a significant challenge to overcome if the benefits of the technique are to be realized. On the other hand, Low Earth Orbit (LEO) plasma wakes — which replicate the GEO environment in several key ways — are feasible to simulate with modern technologies. The fundamental goal of the research project described throughout this dissertation is to establish feasibility of electrostatic actuation for demonstration in LEO.

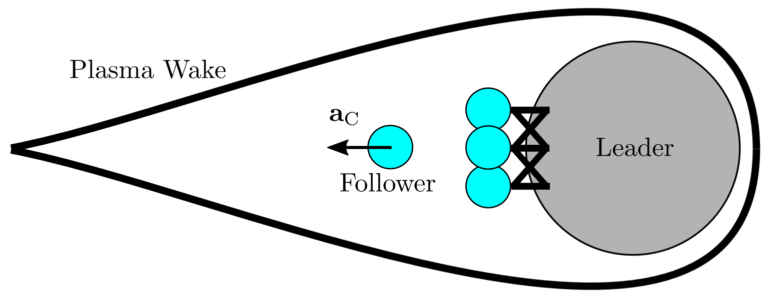

Figure 1.3: Electrostatic actuation in spacecraft wake

The proposed technique is pictured in Figure 1.3. A large leader craft forms a plasma wake as it travels at orbital speeds supersonic to the ionosphere. This wake region is characterized by a sharp decrease in ion density relative to ambient. While the high mobility of the electrons allows them to penetrate into the wake — meaning the environment here is significantly more electron-rich than GEO — the lack of ions mitigates plasma shielding enabling demonstration of electrostatic actuation.

The colored spheres in Figure 1.3 are charged to proscribed voltages by a controller, generating Coulomb accelerations between the charge structure rigidly fixed to the leader craft and the free-flying follower. Models for the electrostatic forces between the two craft and for the plasma wake behavior as objects are charged within are needed in addition to control strategies conformable to the environment before feasibility of electrostatic actuation in LEO can be established.

1.2 Literature Review & Challenges

1.2.1 Modeling of Electrostatic Forces and Torques Between Objects in Motion

A fundamental challenge to electrostatic actuation techniques in all orbits is that of modeling the electric fields around spacecraft geometries. In general, analytic expressions exist only for prototypical shapes. For this reason, early electrostatic actuation investigations considered either spherical craft [98, 97, 36] or applied numerical techniques.[45] Later work[13, 14, 12, 11, 5, 6, 4, 7, 3] expanded the electrostatic modeling to account for three-dimensional spacecraft shapes using the new Multi-Sphere Method (MSM) approximation method to determine force and torque vectors.[85, 87, 42] Application of MSM to a two-spacecraft configuration is shown in Figure 1.4.

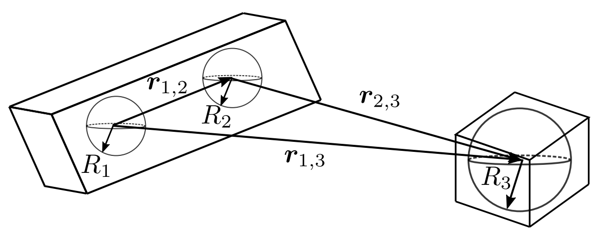

Figure 1.4: MSM Model of two-craft system

MSM is an effective means of approximating electrostatic force and torque interactions due to its low computational requirements and high accuracy.[85] Earlier work assumes the spacecraft is a rigid body with a conducting outer surface. This is a good approximation as most spacecraft are designed to minimize differential charging across spacecraft surfaces. Reference [40] studies how to include hybrid conducting and dielectric outer surface materials into the MSM modeling technique. Recently the homogeneous surface sphere constraint was relaxed yielding a heterogenous SMSM modeling technique.[41] However, none of the prior work has considered the accuracy of a single MSM modeled applied over variations in system geometries. That is a primary contribution of this work and key to the application of electrostatic actuation, as errors in this model affect the conclusions drawn from its application.

1.2.2 LEO Plasma Wake Modeling for Charged Craft

The attainable potential of an object in the space environment is constrained by the current balance equation. The large electron thermal current and ion ram current prevent objects from attaining large potentials in LEO. Additionally, Debye screening prevents electric fields from propagating an appreciable distance from an object's surface. These two conditions have led researchers to the conclusion that electrostatic actuation is unconformable to this orbit regime. The wake region, however, has much lower density and higher temperatures than ambient [34], ionospheric plasma so these currents and the screening effect are less substantial. An ambient plasma wake simulated by the Nascap-2k software is pictured in Figure 1.5.

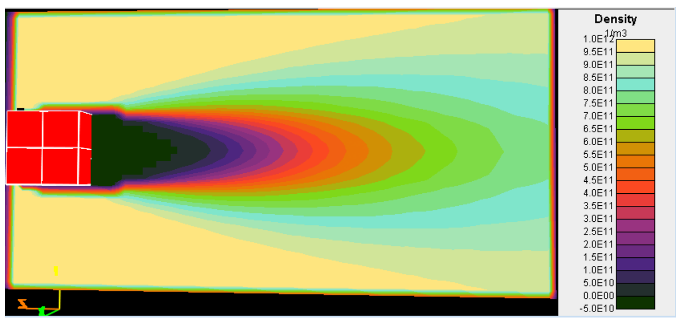

Figure 1.5: Ambient LEO plasma wake simulated in Nascap-2k

Wakes form behind orbiting objects in LEO because the orbital velocity is supersonic with respect to the plasma ions and neutrals. This creates a region antiparallel to the object's velocity that is nearly devoid of these species.[34] Electrons, which have extremely low mass, move much more rapidly and are therefore able to penetrate into the wake. However, the lack of ions in this region creates a negative space charge which screens out lower-energy electrons, so the electron density is decreased and the temperature increased. Additionally, the geomagnetic field will affect the behavior of the electrons in particular because of their low mass.[93] Because the wake always forms in the direction antiparallel to the velocity, the angle between the spacecraft's velocity vector and the local magnetic field must be taken into account. Therefore, the wake's properties will depend on the spacecraft's orbit.

An important feature of the wake is that it contains a nearly pure electron plasma, meaning that the canonical Debye-Hückle theory is inapplicable. Reference [27] provides a discussion and develops an analytic framework which describes screening in a pure electron plasma. This investigation finds that the screening affect is asymmetric in potential — positive potentials are screened effectively while negative potentials are not. Indeed, a negatively charged object in an electron plasma creates a localized, evacuated region that exhibits little to no screening. This proves beneficial to electrostatic actuation in that negatively signed electric fields will propagate much farther in the wake and reduce the thermal electron current by thinning out the electron density in that region.

A substantial body of research supports the development of the proposed technique. References [52, 60] numerically model wake structures in LEO-like plasmas for objects of various sizes, geometries, and voltages, while [90, 59] use simulation chambers to analyze wake structures behind objects of different sizes, geometries, speeds, and voltages. A variety of missions have been conducted to analyze spacecraft charging and beam structures within LEO, including CHAWS [24] and SEPAC [72], the latter of which showed that objects in the wake can be charged to $\sim$ 5kV with a $\sim$ 800W electron gun.

The primary concern with LEO electrostatic actuation is wake collapse — a physical scenario in which a large negative potential in the wake causes an inrush of ambient plasma, destroying the wake. This would compromise the electrostatic actuation system, as excessive power draws and enhanced shielding between spacecraft would result. Therefore, wake behavior resulting from charged craft must be investigated in order to develop feasible LEO electrostatic actuation techniques.

The contributions of this dissertation include just such a study, as well as the development of a technique called wake shaping in which positively charged appendages on the leader craft can be charged to generate a wake with larger geometry. Numerical, experimental, and analytic techniques are applied to provide insight into charged wake dynamics.

1.2.3 Terrestrial Experiments on Charged Wake Dynamics

To develop higher-fidelity models than currently exist in the literature, the design of the Electrostatic Charging Laboratory for Interactions of Spacecraft and Plasma (ECLIPS) being built as part of the proposed project is informed by other wake-investigating facilities including those described in reference [22] and [92]. These publications describe the difficulty in accurately simulating the space environment terrestrially and provide insight on best practices, though the objectives of the ECLIPS chamber motivate the development of novel space simulation techniques. An image depicting the chamber and a subset of its capabilities is included is shown in Figure 1.6.

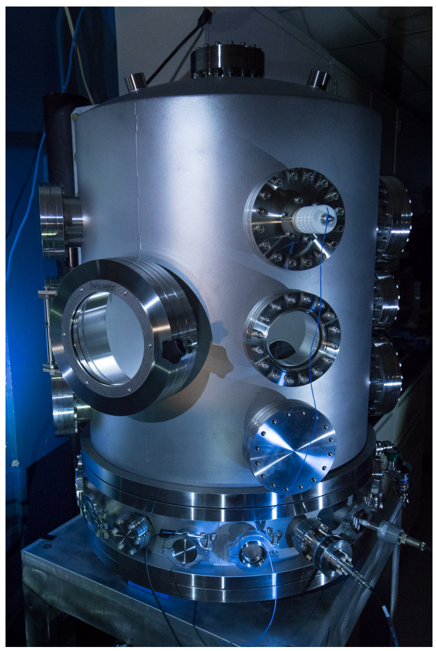

Figure 1.6: The ECLIPS simulation facility

As the acronym implies, ECLIPS is being developed to investigate a wide array of topics relevant to electrostatic actuation including voltage sensing techniques for craft on orbit[9, 99], High Area to Mass Ratio (HAMR) objects charged dynamics [57], and plasma wake dynamics. This latter item is a focus of this dissertation, as the concerns of wake collapse cited previously indicate this phenomenon must be understood for designing electrostatic actuation systems in LEO.

A novel method for generating a wide, dense collimated ion flux in the ECLIPS chamber is proposed in this dissertation. The fundamental goal of the design — motivated by wake shaping experiment results — is closure of the plasma wake. In this case, the wake geometry can be clearly defined, providing insight into electrostatic actuation and potential wake shaping applications.

1.2.4 Electrostatic Actuation Control Techniques

The use of Coulomb forces for spacecraft formation keeping was first studied in 2002 and was predicted be highly efficient compared with conventional thrusters across various scenarios.[45] This thorough investigation applied numerical simulations to estimate the electrostatic forces and torques between spacecraft across a variety of simulated GEO environments. Equilibria of multi-spacecraft systems are derived using the perturbed Hill Clohessy-Wiltshire equations including the approximated Coulomb accelerations. Estimates of power requirements and a discussion of charging mechanisms lead the author to the conclusion that electrostatic actuation can provide fuel savings of up to 98% compared to current techniques.

The results of this initial study motivated a great many investigations of formations controlled using only Coulomb forces [77, 73, 64, 74, 16, 94] or incorporating traditional thrusters to create a hybrid control approach.[70] Once electrostatically controlled formations had been studied in some detail, investigations into Coulomb-force driven on-orbit collision avoidance [97], orbit element corrections [37, 38], relative attitude control [80, 14, 10, 89], and debris mitigation [76, 79, 39] demonstrated that electrostatic actuation could facilitate a variety of operations on orbit.

Multiple experimental campaigns have been undertaken to demonstrate the feasibility of electrostatic actuation for relative position and attitude control between nearby objects. Reference [81] describes a 1-dimensional air bearing track used to demonstrate a variety of control scenarios achieved through electrostatic actuation.[82] A different testbed was developed to demonstrate that the technique could bring an object spinning about a single axis to rest.[88] While these testbeds provided a baseline for future electrostatic actuation experiments, the presence of atmospheric drag and both testbeds' 1-dimensional nature limit the amount of insight gained for on-orbit applications. While vacuum chamber experiments would provide a more GEO-like environment, the large gravitational force on Earth's surface overwhelms any Coulomb forces that can reasonably be generated.

This provides yet another motivation for demonstration of electrostatic actuation in LEO plasma wakes. If feasibility of the technique can be established terrestrially through the projects described in this dissertation and others, opportunities for a LEO technology demonstration mission could be sought. The electrostatic actuation system proposed in this project is pictured in Figure 1.7.

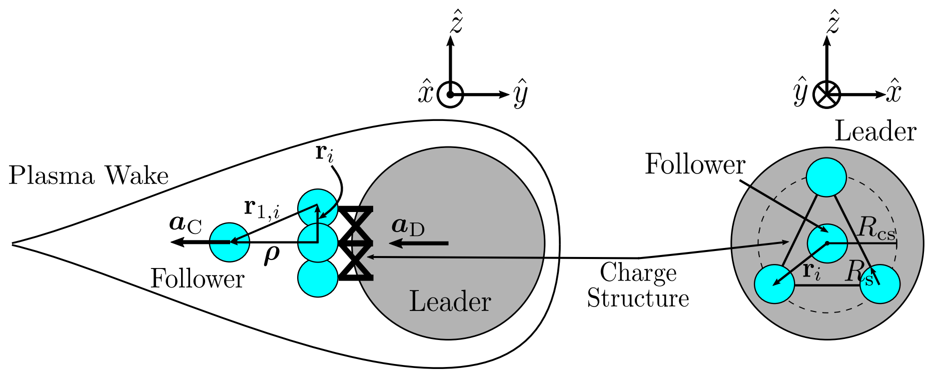

Figure 1.7: LEO electrostatic actuation system for leader-follower formation

The wake geometry dictates the implementation of a close-proximity leader follower system. While the wealth of electrostatic actuation control techniques for GEO inform application to LEO, the limiting hazard of wake collapse necessitates careful development of highly-specific control strategies. This is the primary contribution of the final chapter of this dissertation.

1.3 Research Overview

This ongoing, interdisciplinary project aims to combine astrodynamics, electrostatics, plasma physics, and Guidance, Navigation, and Control (GNC) techniques to accomplish the overall project goal: to develop electrostatic actuation techniques conformable to LEO plasma wakes for future demonstrations of the technology.

The primary challenge of the project is finding a balance between the nonlinear Coulomb acceleration evidenced by the MSM formulation; the highly erratic plasma phenomenon, wake collapse in particular; and the control techniques which dictate the voltages sourced by the electrostatic actuation system. This project addresses each of these items, attempting to modify current techniques or develop new ones to widen the feasible parameter space for electrostatic actuation in LEO plasma wakes.

The proposed project is defined by the overall project objective — restated for convenience — and four stated goals as listed below.

Develop electrostatic actuation techniques conformable to LEO plasma wakes for future demonstrations of the technology

1 Develop a model for electrostatic interactions between maneuvering, close-proximity craft

2 Develop a model for plasma wake behavior for different applied magnetic fields and craft sizes, geometries, and potentials

3 Design a LEO plasma simulation technique appropriate for the study of plasma wake behavior in terrestrial vacuum chambers

4 Derive efficient electrostatic actuation control strategies for use within LEO plasma wakes

Chapter 2

Electrostatic Interactions between Spacecraft in Motion

Fundamental to the development of electrostatic actuation is a means for rapidly estimating electrostatic interactions between nearby objects in motion. Specifically, the model applied must provide Coulomb accelerations faster than real time so that it can be applied for control applications. Numerically approximating the electric field around an object can be difficult, especially if it exhibits complex geometries. A variety of techniques exist for electric field estimation including the Method of Moments (MoM)[32], but these generally require evaluation of either an integral or differential equation. This makes these methods ill-suited for control applications, as the frequency of the controller is bottlenecked by the time taken to calculate the electric field.

The recently developed Multi-Sphere Method (MSM) [86] provides a means for estimating the electric field around complex geometries. The method is algebraic and therefore highly computationally efficient. It has been shown to match MoM and other methods to high accuracy, though until recently had not been analyzed for time-varying shapes. To accurately estimate the electrostatics around an object, an MSM model is tuned to some electrostatic parameter.[86, 20, 42] The question of applicability to time-varying shapes comes down to the degree to which the model must be retuned as the system undergoes configuration change. If high accuracy and efficiency can be maintained, then MSM can be used to model Coulomb acceleration between spacecraft in electrostatic actuation simulations.

The first goal of the proposed research project is to develop a method for rapidly and accurately estimating electrostatic interactions between multiple charged craft in motion — a novel

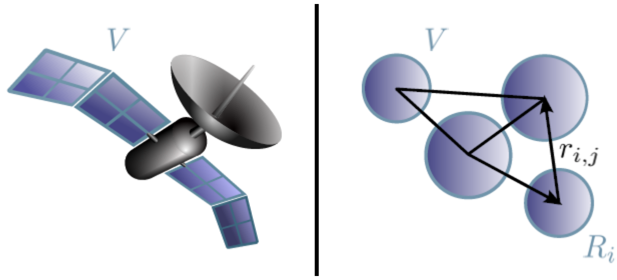

Figure 2.1: Replacement of complex geometries with MSM spherical shells

contribution. This goal is fundamental to the overall project thesis because the development of electrostatic actuation control techniques requires an analytical model of Coulomb forces and torques between charged spacecraft in motion.

2.1 Multi-Sphere Method Overview

MSM [86] is an accurate, computationally efficient technique for determining the charge-to-voltage relationship of general objects and systems — a key step in efficiently estimating electric fields. The fundamental concept is pictured in Figure 2.1. A spacecraft exhibiting complex geometries is modeled by a set of spherical conducting shells placed and sized such that some electrostatic parameter — the Coulomb force [86], capacitance [20], or electric field [42] — matches between the model and some truth metric defined via a Finite Element Method (FEM) software package, MoM, or some other means. The benefit of the method is that this computationally expensive matching process is only conducted once to initialize the MSM sphere radii $R_1, R_2, ..., R_n$, after which the electric field can be approximated efficiently as described immediately below.

The voltage on each of the spheres shown in Figure 2.1 is calculated as a sum of its own charge's contribution and those from the other nearby spheres.

$$V_i = k_c \frac{Q_i}{R_i} + k_c \sum_{j=1, j\neq i}^{n} \frac{Q_j}{r_{i,j}} \tag{2.1}$$

Here, $k_c = 8.99 \times 10^9$ Nm^2/C^2 is Coulomb's constant, R_i is the radius of the i^{th} sphere, and $r_{i,j}$ is the distance between the i^{th} and j^{th} spheres. Given this definition, $r_{i,j} = r_{j,i}$ for all i and j. These relations are rewritten into the following matrix equation

$$\begin{pmatrix} V_1 \\ V_2 \\ \vdots \\ V_n \end{pmatrix} = k_c \begin{bmatrix} 1/R_1 & 1/r_{1,2} & \dots & 1/r_{1,n} \\ 1/r_{1,2} & 1/R_2 & \dots & 2/r_{2,n} \\ \vdots & \vdots & \ddots & \vdots \\ 1/r_{1,n} & 1/r_{2,n} & \dots & 1/R_n \end{bmatrix} \begin{pmatrix} Q_1 \\ Q_2 \\ \vdots \\ Q_n \end{pmatrix}, \quad \mathbf{V} = [S]\mathbf{Q} \tag{2.2}$$

The matrix $[S]$ is called the elastance.[84] The charge-to-voltage relationship, $\mathbf{Q} = [C]\mathbf{V}$, illustrates that the capacitance is the inverse of the elastance matrix.

$$\mathbf{Q} = [S]^{-1}\mathbf{V} \tag{2.3}$$

This form is preferable in the electrostatic force and torque evaluation process as the voltage is usually known and the dynamics are dependent on charge. Given the set of charges calculated from Eq. (2.3), Poisson's electrostatic field equation allow for calculation of the resulting electric field via superposition. This allows MSM to model the electric field at a point $\boldsymbol{r}$ about an object modeled with n MSM spheres using Eq. (2.4). Below, $\boldsymbol{r}_i$ represents the vector between the query position $\boldsymbol{r}$ and the i^{th} sphere.

$$\boldsymbol{E} = k_{\text{C}} \sum_{i=1}^{n} \frac{Q_i}{r_i^2} \boldsymbol{r}_i \tag{2.4}$$

With this expression for the electric field, the forces and torques on the object can be determined via super particle theorem [75] and knowledge of the object's center of mass and charge. Losses in numerical accuracy occur because the MSM model provides only an approximation of the true electric field about the object. However, prior work has shown that for two bodies separated by distances on the order of the spacecraft dimensions these approximations have errors in electric field of 1% or less.[42]

Notably, the above discussion of the MSM technique considers only a single, isolated craft. Application to an electrostatically-controlled formation naturally requires additional computation. A novel contribution of this project is the demonstration that MSM can be applied to accurately simulate forces and torques between charged objects in time-varying systems.

2.2 Application of MSM to Time-Varying Systems

The prime difference in applying MSM to a formation rather than a single craft is a time-varying charge-to-voltage relationship for the system. Inspection of equations (2.3) and (2.4) indicates this will also affect the electric field around the objects, even for constant voltages. If multiple rigid bodies are modeled, the diagonal blocks of the elastance matrix remain constant while the off-diagonal blocks vary with time as the formation geometry changes.[87, 85, 42]

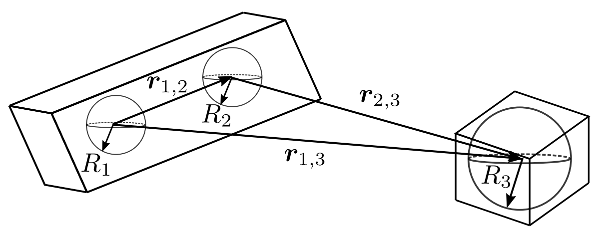

Figure 2.2: MSM Model of Two-Craft System

To illustrate how a time-varying MSM model for a system is set up, consider Figure 2.2. The charge-to-voltage relationship is developed according to the MSM formulation to yield the following elastance matrix.

$$\begin{bmatrix} V_1 \\ V_2 \\ V_3 \end{bmatrix} = k_c \left[\begin{array}{cc:c} 1/R_1 & 1/r_{1,2} & 1/r_{1,3} \\ 1/r_{1,2} & 1/R_2 & 1/r_{2,3} \\ \hdashline 1/r_{1,3} & 1/r_{2,3} & 1/R_3 \end{array}\right] \begin{bmatrix} Q_1 \\ Q_2 \\ Q_3 \end{bmatrix} \tag{2.5}$$

As discussed above, the upper-left and lower-right blocks of the elastance matrix — which represent the self-elastance of the two-sphere and one-sphere spacecraft, respectively — remain constant as the spacecraft maneuver relative to one another, while the off-diagonal elements must be updated each time step with the current relative positions of the spheres.

Similar to the classical MSM process described in Section 2.1, the MSM sphere radii R_i are initialized given some truth value. However, as the two craft in Figure 2.2 move relative to one another these MSM sphere radii no longer hold as they were generated for a different system. Prior work on time-varying MSM re-optimized these sphere radii as the objects moved, resulting in a substantial increase in computational effort.

The novel contribution of this goal is the study of the accuracy of time-varying MSM without re-optimizing as crafts in the modeled system move. The primary focus is the trade-off between the computational savings of recomputing only $r_{1,3}$ and $r_{2,3}$ and the resulting decrease in accuracy. While the electric field computation requires an inverse regardless of re-optimization, the structure of the generalized elastance matrix in Eq. (2.2) is such that the Schur complement [100] can be applied — iteratively for more than two craft — to calculate the capacitance without requiring a full $n \times n$ inverse. This enables efficient computation of more complex multi-spacecraft systems than specifically considered in this dissertation.

2.3 Comparison of MSM and Analytical Electrostatic Models

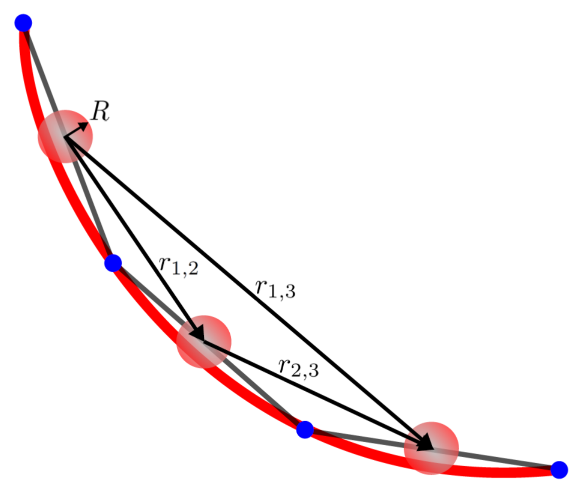

Figure 2.3: MSM model of multi-link pendulum

To investigate the application of MSM to time-varying shapes, an MSM model is developed for a thin conducting wire. The model is then reconfigured into a ring shape without changing the MSM sphere radii and the system capacitance and electric field are compared with truth models. These shapes were chosen because analytic capacitance and electric field models have been derived

— this is not the case for most geometries hence the need for techniques like MSM and MoM. Figure 2.3 shows such a wire object modeled as a multi-link pendulum with MSM spheres placed at the center of each link.

The capacitance of a long, thin, straight wire is given by Reference [43] as

$$C = \frac{l}{k_c \Lambda} \left[1 + \frac{1}{\Lambda}(1 - \ln 2) + \frac{1}{\Lambda^2} \left(1 + (1 - \ln 2)^2 - \frac{\pi^2}{12} \right) + \mathcal{O}\left(\frac{1}{\Lambda^3} \right) \right] \tag{2.6}$$

where

$$\Lambda = \ln \left(\frac{l}{a} \right), \tag{2.7}$$

the variable l is the length of the wire and a is its radius. This equation is valid for large Λ, which requires that the wire length is much greater than the radius. This scalar capacitance value is used to optimize the sphere radius R used in the model. The comparison to the capacitance described in Eq. (2.3) is accomplished by summing the members of the matrix capacitance as in Eq. (2.8).

$$C_{\text{scalar}} = \sum_{j=1}^{n} \sum_{i=1}^{n} C_{i,j} \tag{2.8}$$

If the wire changes shape, Eq. (2.6) no longer holds. However, the optimization to generate the sphere radii for the diagonal of the elastance matrix is computationally expensive, and determining the nominal capacitance to which to optimize is non-trivial for complicated shapes such as a flexing wire. The error resulting from holding these diagonal components constant while letting the off-diagonal terms in Eq. (2.5) vary as the shape changes is investigated to determine if re-optimization is necessary.

In addition to the straight line, an analytical approximation exists for the capacitance of an anchor ring with uniform charge. Reference [91] shows that the capacitance of a charged ring whose cross sectional radius r is small compared to the ring radius ρ is

$$C = \frac{\pi \rho}{k_c \ln \left({}^{8\rho}/_{r} \right)} \tag{2.9}$$

Two configurations of a 20-link system similar to that shown in Figure 2.3 are compared. First, the link is arrayed as a 3 m straight line and the MSM sphere radii are optimized to match the capacitance in Eq. (2.6). The MSM system is then rearranged into a ring shape of radius ∼0.5 m — calculated by equating the length of the wire and circumference of the ring — as in Figure 2.4 without changing the MSM sphere locations within each link, or the sphere radii to match the capacitance of the ring. The off-diagonal terms of the capacitance matrix account for this new geometry and the sum of all matrix elements is compared to the analytical result in Eq. (2.9).

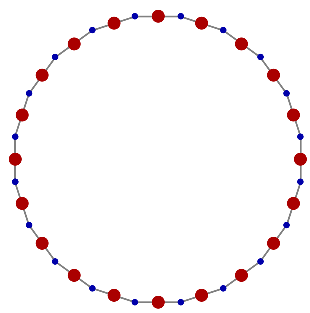

Figure 2.4: 20-link MSM model of an anchor ring. The blue circles indicate the hinge locations, while the red accurately represent the MSM sphere radii optimized using Eq. (2.6)

Figure 2.5 shows the error between the MSM capacitance derived from the process described above and the analytic ring capacitance in Eq. (2.9) for a given number of links (n_l) and number of spheres on each link (n_s). Note that, for a 20-link system, the MSM capacitance matches the analytic to within 3%, though high accuracy is still achieved in lower-fidelity models. Interestingly, the addition of more spheres on a given link (i.e. the cases where $n_s > 1$) negatively impacts capacitance matching. A larger number of spheres per segment provides a better model of the n_l-sided polygon, not the true circular shape. Thus if a continuous deflection is modeled with the flexible MSM approach, only a single sphere should be assigned per segment. Higher accuracy is achieved by incorporating more segments. On the other hand, if the time-varying shape is due to the articulation of a rigid component of a solar panel, then adding more spheres to the panel model can improve overall accuracy. For this reason, all future discussions for the continuous wire model deflections consider only a single MSM sphere on a given link of the model. The high accuracy discussed above indicates that the capacitance can be well-approximated by an MSM model without re-optimizing at each time step.

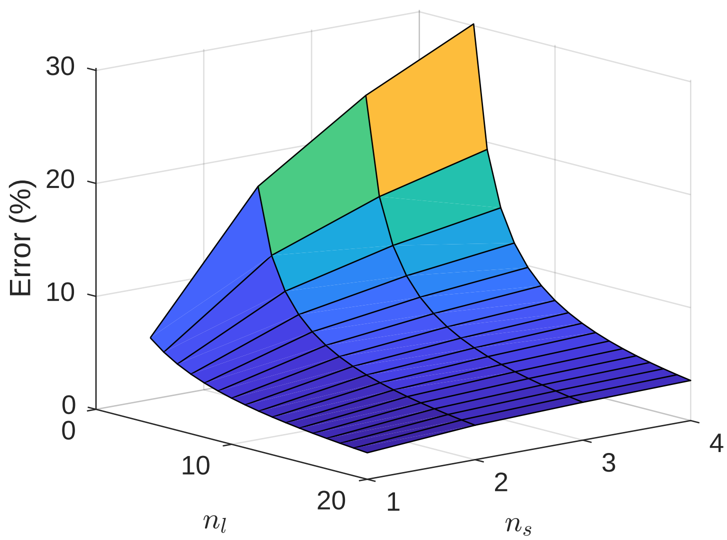

Figure 2.5: Percent difference between MSM and analytic anchor ring capacitance for various numbers of links and MSM spheres

The accurate capacitance matching indicates that, for a given voltage, the total charge on the MSM model will match that on an anchor ring. However, the goal of flexible MSM is to accurately model dynamics resulting from electrostatic interactions. This requires that the electric fields match as well. Reference [101] presents a method for approximating the electric field near a ring of charge. This is compared with the MSM model's electric field, calculated via superposition of the individual field of each MSM sphere.

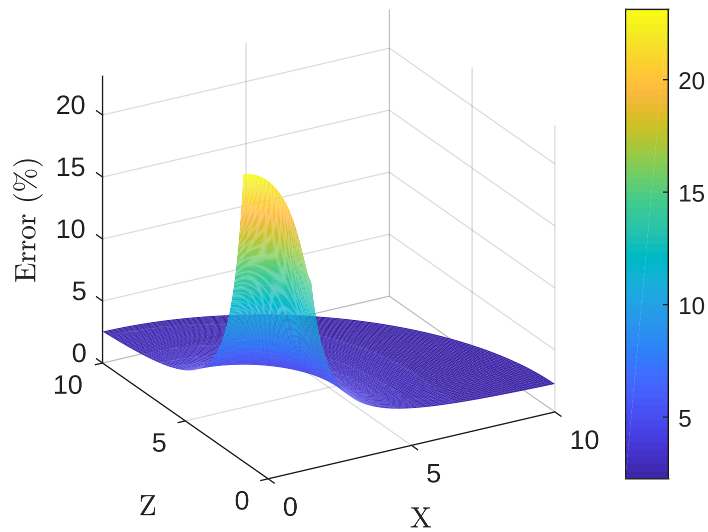

Figure 2.6: Percent difference between electric field magnitudes for a 20-link MSM model and analytic anchor ring approximation. The **X** and **Z** axes are in units of the ring radius (∼0.5 m).

Figure 2.6 shows the percent difference between the two electric fields of the same ∼0.5 m radius ring discussed above charged to 1 kV. The distances along the X and Z axes are displayed in units of the ring radius. For this coordinate system, the Z axis is aligned with the anchor ring's axis and X lies in the plane of the picture in Figure 2.4. The origin of the system is at the edge of the anchor ring (i.e. the space inside the ring is not analyzed). Because an anchor ring exhibits symmetry about its axis, so does its electric field. Therefore, the complete field can be analyzed by consideration of the single plane pictured in Figure 2.6.

Note that, for distances less than ∼two ring radii, the electric field error is large due to the discrete nature of the charge distribution present in the MSM model, but not in the approximation presented by reference [101]. At farther points, the error converges to the same 3% exhibited by the capacitance as shown in Figure 2.5. While various proximity operations are subject to different model error constraints, an accuracy of <5% at a few body radii after significant deformation indicates that — for this system — there is no need to re-optimize the MSM model as deformations occur.

The results of the investigation above indicate that MSM can be used to accurately model time-varying systems subject to application-specific constraints. While discrete system geometries were considered, the fundamental insight gleaned that accuracy is maintained over significant system reconfiguration applies to general geometries. The exception illustrated in Figure 2.6 is that accuracy is lost when objects are in close proximity — an already well-known challenge of MSM and similar models. This can be mitigated by initializing the MSM model with higher n_l as discretization is the source of error.

2.4 Results & Summary of Goal 1

The investigation described considers the accuracy of an MSM model over large system reconfiguration. It is shown that as objects move relative to one another, the system capacitance is well-described by a set of MSM spheres optimized with some initial state. Limitations to the model certainly exist — consider the $1/r_{i,j}$ dependence in Eqs. (2.2)-(2.4) and the scenario of overlapping spheres — but the results shown above indicate that the expensive sphere-optimization process can be avoided in applying MSM to time-varying systems. Therefore, the method can be used to rapidly and accurately estimate electrostatic forces and torques between spacecraft in motion and in developing spacecraft orbit controllers. The development of this capability was the fundamental goal of this chapter and is considered achieved.

Chapter 3

Plasma Wake Modeling

Understanding plasma wake behavior under various environmental configurations and charging scenarios is essential to the development of electrostatic actuation techniques conformable to the LEO environment. The primary concern is that a selected control methodology sources enough voltage that the plasma wake collapses and the ion-void nature of the wake is compromised. The spatial decay of voltages means that wake collapse conditions vary for different system configurations. For example, a small charged object deep in the wake of a large craft — a charged cubesat behind the ISS, for instance — can source large potentials without risking wake collapse as the distance from the voltage source to the edge of the wake is large. However, limitations exist if the in-wake craft is roughly the same size as the wake-generating craft.

The significant variability in spacecraft geometries and sizes makes it challenging to find a one-size-fits-all solution to the question of wake behavior. In this chapter the Nascap-2k [50] spacecraft charging and environment simulation suite is applied to investigate general trends for prototypical spacecraft and formations. Nascap-2k has shown success in modeling complex spacecraft-plasma interactions including replicating the results of the Charging Hazards and Wake Studies Experiment (CHAWS).[26] This on-orbit experiment is particularly applicable to LEO electrostatic actuation, as it considers the ion plasma current onto a highly-charged object in another's wake.

The collapse of the wake would exacerbate two undesirable phenomena — plasma shielding and enhanced current at a given voltage. Unfortunately, these effects both result in larger power requirements and compound one another. Enhanced plasma shielding means that electric fields decay more quickly in the plasma, resulting in a larger required voltage to achieve the same electrostatic force and/or torque. The increase in plasma density resulting from the collapse of the wake means that more current is sourced for a given voltage — which now must be amplified due to the enhanced shielding — driving up power requirements.

As with all on-orbit control methodologies, a primary concern is cost. A major benefit of electrostatic actuation is that it uses only electrical power, a renewable resource. That being said, essentially every spacecraft subsystem also depends on this same resource. Therefore, electrostatic actuation techniques should be developed such that they can be applied without requiring excessive power.

The environmental currents between a conductor charged to a given potential and the surrounding environment must sum to zero — this physical condition is called current balance.[30] For most craft in LEO, the dominant currents are those from the plasma ions I_{i} and electrons I_{e}; photoelectron emission I_{pe} when the spacecraft is sunlit; and secondary I_{se} and backscattered I_{bs} electrons resulting from plasma impinging on spacecraft surfaces. Generally speaking, the plasma currents vary strongly with the surface potential because the spacecraft acts as a source or sink to plasma elements. Generally speaking, the ion current is lower than the electron because the current is proportional to the particle velocity which is far lower for these heavy constituents. The photoelectron current depends on the sunlit area of the craft and its orbit whereas electron emission from plasma impact depends on the the particle, material, and details of the collision.

For electrostatic actuation techniques, an additional current must be assumed, referred to as the active current I_{act}. This is a current sourced by the spacecraft through ejection of plasma into the environment or some other method affecting current balance such that a desired potential is sourced on the spacecraft.[66] A wealth of literature exists describing the physics of spacecraft charging and mechanisms for achieving a desired potential on a spacecraft surface. [48, 47, 29, 35] Notably, magnetic fields will affect the plasma currents and wake geometry. These effects depend on the orbit inclination and orbit position and therefore require significant study to generate overall trends. Even in the worst case, the changes in shielding and power are small and mission specific, so magnetic field effects are neglected in this dissertation.

The power requirement P_{ea} for electrostatic actuation comes down to the required active current I_{act} to achieve a desired applied potential V_{app}.

$$P_{\mathrm{ea}} = V_{\mathrm{app}} I_{\mathrm{act}} \tag{3.1}$$

For the purposes of this project, charging via electron or ion beam emission is assumed. In this case, the spacecraft can charge up to — but not exceeding — the beam energy E_{b}.[48] Potentials lower than the beam energy result from the beam current $I_{\mathrm{b}} = I_{\mathrm{act}}$ being insufficient to achieve current balance at the desired voltage. As indicated above, the electron emission currents I_{pe}, I_{se} and I_{bs} do not vary significantly with the spacecraft potential. Therefore, the primary concern for electrostatic actuation techniques are excessive plasma currents I_{i} and I_{e} that cannot be balanced with the plasma beams on board. Such currents could result if wake collapse were to occur, bringing the ambient plasma down onto the spacecraft. As discussed above, wake collapse depends on the wake size and sourced potentials.

The discussion immediately above indicates that the size of a follower craft relative to the wake of the leader is a strong indicator of the power requirements of electrostatic actuation techniques in LEO. Therefore, the development of techniques that expand the plasma wake of a given leader — referred to as wake shaping — could result in an overall lower power requirement, subject to system configuration.

One way to enhance the size of the wake is to expand the ram-facing area of the leader craft. An obvious problem here is an increase to launch mass costs as well as area-dependent perturbations like drag or SRP. Instead, wake shaping techniques developed as part of this research project apply positive voltages to thin, sparse structures to expand the wake with electrostatic repulsion. Experimental methods must be applied in this case as Nascap-2k and similar Finite Element Method (FEM) dependent techniques face convergence issues when thin geometries are simulated.

The project described in this chapter provides great insight into the application of electrostatic actuation in LEO. First, the ambient wake simulation is shown to match previous theory and experiments. Motivation is then provided for the application of electrostatic actuation in plasma wakes rather than ambient LEO. This is followed by parametric studies across potential sign, potential magnitude, and craft size which provides practical limits on electrostatic actuation techniques. Finally, two wake shaping experiments are run which provide insight into the feasibility and cost of expanding a plasma wake.

3.1 Investigation of Plasma Wake Dynamics with Nascap-2k

The complexity of plasma dynamics precludes analytic investigations and challenges of running experiments across large parameter sets motivate the use of Nascap-2k to investigate wake dynamics given a charged follower craft. As discussed previously, this simulations software package has shown success in replicating experimental plasma wake measurements highly relevant to this project.

This section outlines a series of Nascap-2k simulations run to investigate wake dynamics resulting from a variety of spacecraft and formation geometries and applied potentials. The results of these simulations provide invaluable data about power requirements and wake geometry essential to the application of electrostatic actuation in LEO.

In all simulations to follow, the spacecraft velocity vectors are in the leftward direction so that the wake will form in the -Z direction behind the leader spacecraft. Spacecraft orbital speed is assumed to be 7.7 km/s to indicate a 400 km orbit. This is roughly consistent with the 10^{12} m^{-3} plasma density and 0.1 eV plasma thermal energy chosen in the environment definition. Unless otherwise indicated, a single-specifies oxygen plasma is simulated. All spacecraft are considered to be composed entirely of aluminum, and therefore each has a single body potential at all times. All environmental currents discussed previously — plasma electron, plasma ion, photoelectron, secondary electron, and backscattered electron — are included in all Nascap-2k simulations. All objects are considered sunlit for all simulations. The environmental simulation parameters used in all simulations are identical to those in the CHAWS simulation which replicated on-orbit plasma

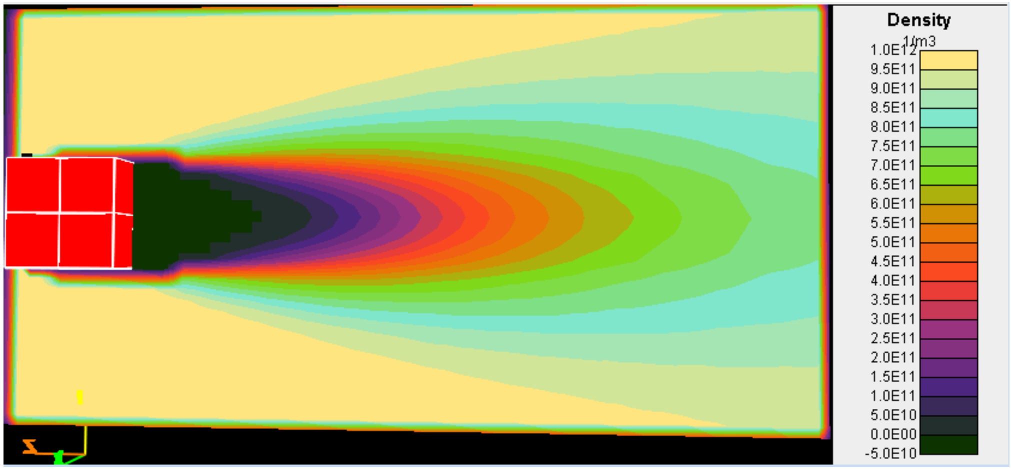

Figure 3.1: Ambient ion density behavior near 1 m spacecraft charged to 0 V in LEO

wake experiments.

It should be clearly noted that these simulations do not apply Particle-in-Cell (PIC) methods, but instead use a non-linear spacecharge model as recommended in the Nascap-2k user's guide. This model accounts for spacecharge interactions between plasma elements — an important feature for the ion-void plasma wake — and applies the charge density model from reference [17]. A key feature of this model for application of electrostatic actuation in LEO plasma wakes is a smooth transition between different plasma screening regimes.[25] As mentioned previously, this solution technique was applied in replicating CHAWS data.

3.1.1 Ambient Plasma Wakes

An initial control simulation is run to determine the ambient wake behavior for the LEO small sat of side length 1 m shown in Figure 3.1. The spacecraft is assumed to be in electrostatic equilibrium with the ionosphere here. The geometry of the wake shown agrees well with the predictions, simulations, and experiments summarized in reference [34]. However, this same reference indicates that the "floating" potential — the steady-state potential at which all currents to the spacecraft balance — for small satellites in LEO, is slightly negative due to the higher electron than ion ram current.

Consider the same cubic spacecraft biased -1 V relative to the ionosphere. The ion and electron density in the vicinity are shown in Figure 3.2 and 3.3, respectively. While certain aspects of the wake shown in Figure 3.1 are preserved, complex plasma structures result from even this slight charging. Of the various observable differences, the most relevant to this research is the geometry change to the wake. This is characterized by a contraction along the axis of the wake, and the creation of a second low-density region. This latter result is qualitatively consistent with DiP3D simulations of wakes behind negative objects.[58] This wake contraction is a serious practical consideration for electrostatic actuation, as it makes wake collapse more likely.

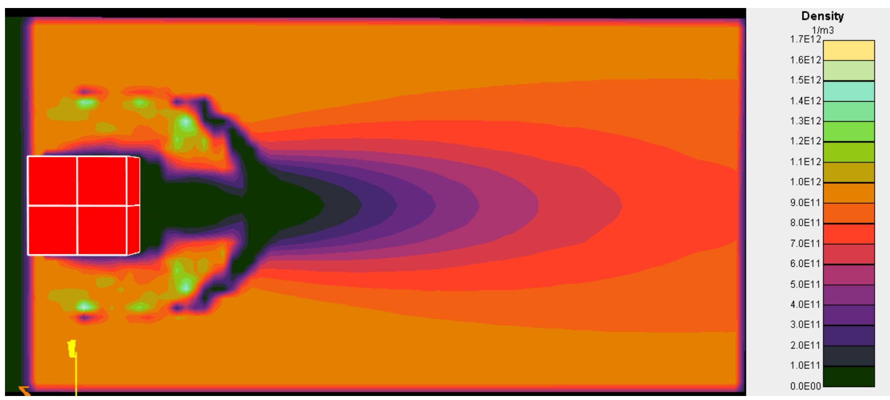

Figure 3.2: Ambient ion density behavior near 1 m spacecraft charged to -1 V in LEO

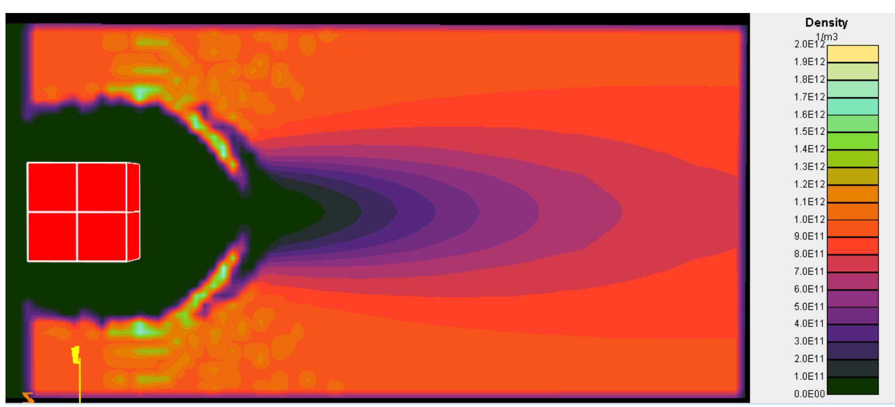

Figure 3.3: Ambient electron density behavior near 1 m spacecraft charged to -1 V in LEO

Unless otherwise indicated, the leader craft is assumed to be held at -1 V. This is reasonable as current balance usually brings LEO spacecraft to slight negative potentials. Additionally, technologies like plasma contactors can be applied to equilibrate the leader with the ambient plasma if desired.

3.1.2 Wake Collapse

To illustrate why wake collapse is undesirable, a dual-spacecraft simulation was run with body potentials roughly representative of electrostatic actuation. The geometry shown consists of two cubic spacecraft each side length 1 m separated by 0.5 m. The ion and electron densities in the vicinity of the craft are shown in Figures 3.4 and 3.5.

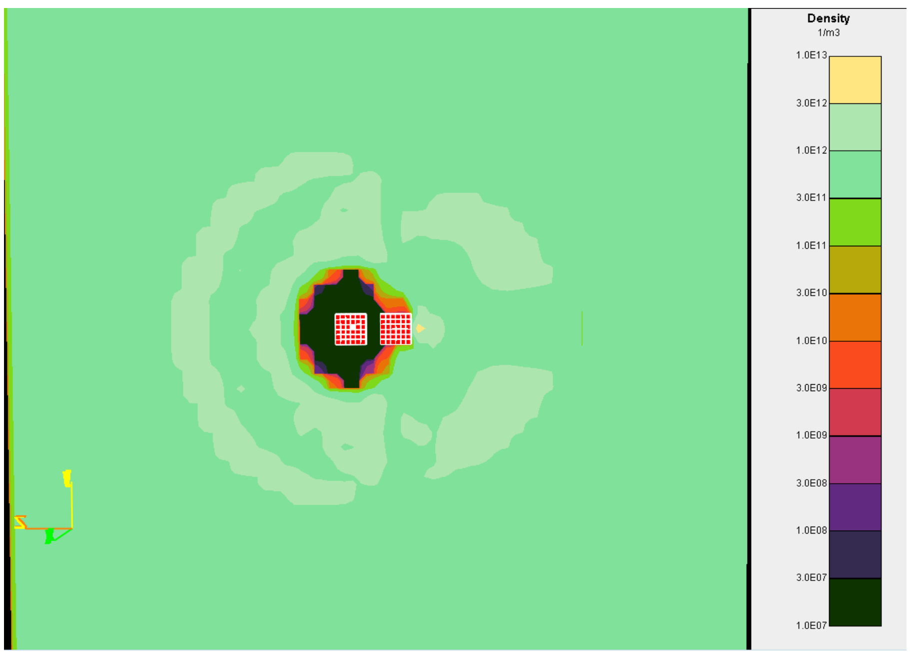

Figure 3.4: Ion density of wake collapse between leader (left) charged to 1000 V and follower craft (right) charged -1000 V

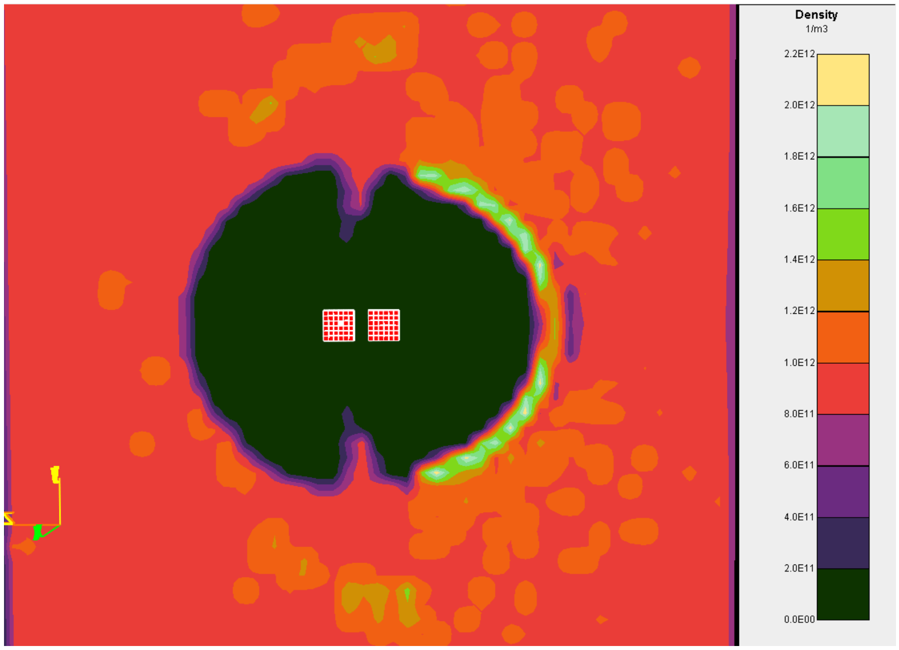

Figure 3.5: Electron density of wake collapse between leader (left) charged to 1000 V and follower craft (right) charged -1000 V

Several consequences for electrostatic actuation arise from this wake collapse demonstration. Firstly, the excessive potentials relative to the ionosphere's thermal energy ($\sim$ 0.1 eV) has sucked all the nearby plasma down onto the craft. This is evidenced by the extremely large plasma currents to both craft. Assuming a power system with perfect efficiently, Nascap-2k predicts that the negatively charged object experience a maximum power draw of $\sim$3000 W, while the positively charged craft draws a massive $\sim$3,600 W. The differences in power values makes sense given the higher mobility of electrons. These are clearly not sustainable values for modern spacecraft power systems.

Interestingly, the potentials and formation geometry result in a completely evacuated region between the two spacecraft, indicating that electric fields would experience little to no shielding. Other examples of wake collapse are shown later in which both excessive power draw and plasma shielding result. Regardless of this circumstance in Figures 3.4 and 3.5, the large power requirement makes this application unfeasible. Therefore, it is determined that LEO electrostatic actuation can only take place in coherent plasma wakes.

3.1.3 Positive Charging in the Wake

The analysis presented in reference [27] indicates asymmetric potential shielding in the wake. The result that negative potentials experience little shielding in the wake motivates their use. Prior results and discussion in this chapter contradict this, as positive potentials do not risk wake collapse and in fact expand its geometry.

Consider the close-proximity leader-follower configuration pictured in Figures 3.6-3.9 for various positive follower potentials. The leader craft is biased to -1 V and is 1 m in diameter. The follower craft has side length 0.1 m and is placed in the deep wake at 0.5 m.

Figure 3.6 shows the ion and densities for the follower craft biased to 5 V. Notice here the non-intuitive result that a positive voltage nearly causes the wake to collapse as the plasma reconfigures itself to mitigate the resulting electric field.

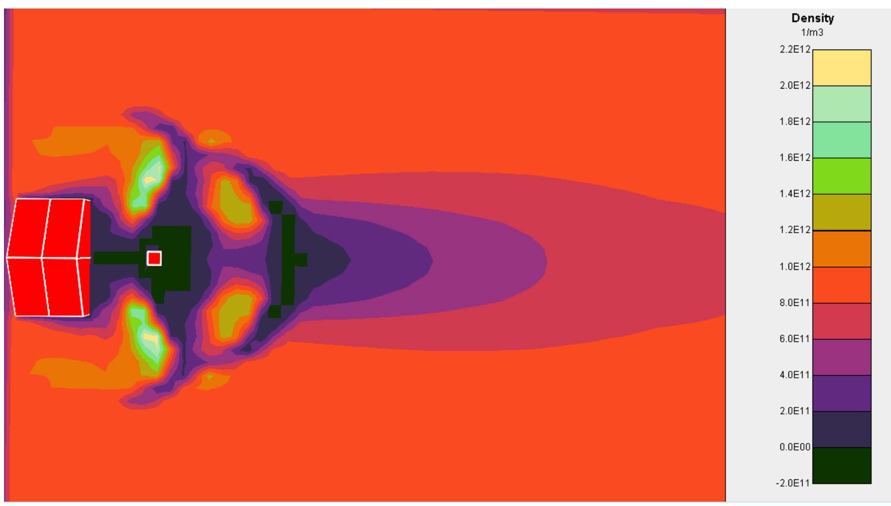

Figure 3.6: Ion density of close-proximity formation with $D_l = 1$ m, $V_f = 5$ V

The electron density for the 5 V follower simulation is shown in Figure 3.7. Notice that the electron-devoid region is expanded relative to Figure 3.3, as the follower craft voltage — though small compared to typical electrostatic actuation potentials — is large compared to the electron temperature set to 0.1 eV in the simulation.

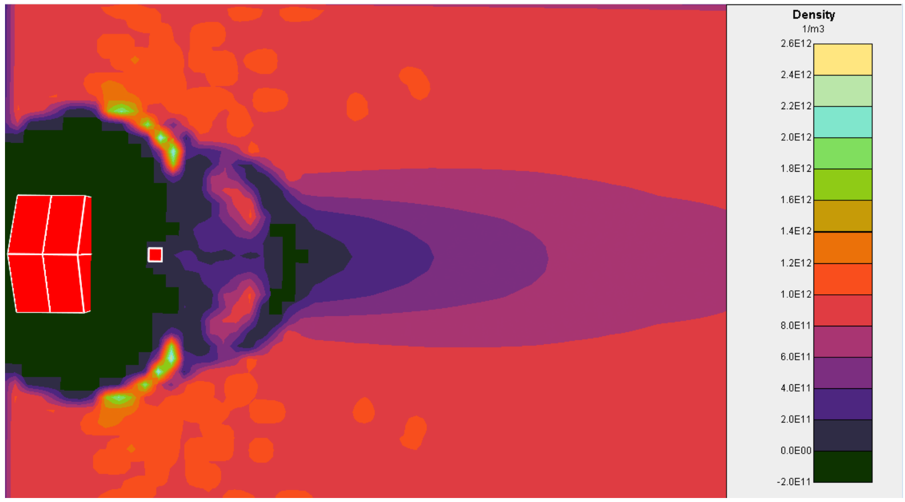

Figure 3.7: Electron density of close-proximity formation with $D_l = 1$ m, $V_f = 5$ V

The densities for a much larger positive follower voltage are shown in Figures 3.8 and 3.9 for the same geometry. As expected the large positive follower voltages serves to expand the wake, enabling a larger area for electrostatic actuation techniques. This benefit comes at the steep cost of massive power requirements as nearly all electrons for 1 m around are sucked on to the follower as shown in Figure 3.9.

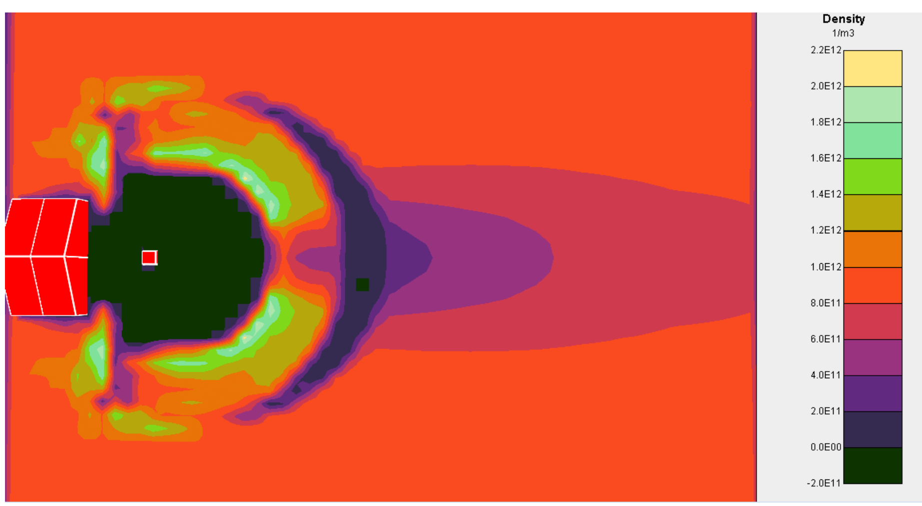

Figure 3.8: Ion density of close-proximity formation with $D_l = 1$ m, $V_f = 500$ V

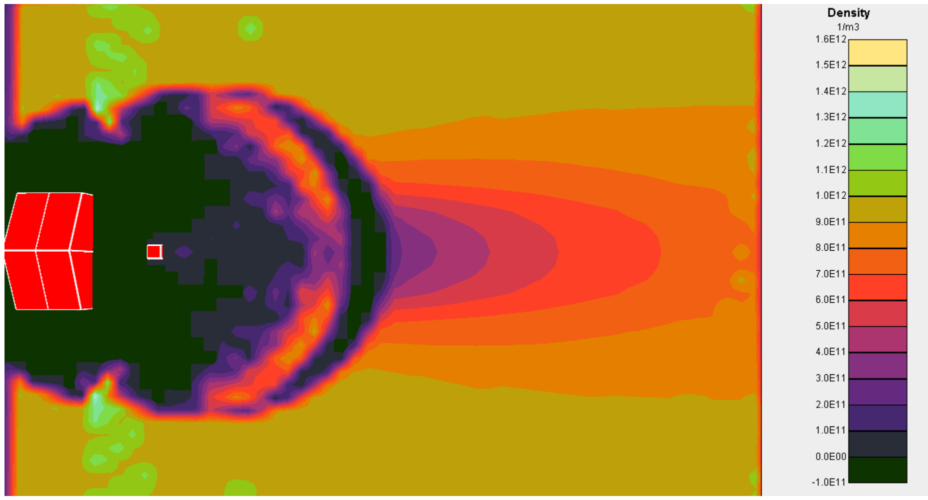

Figure 3.9: Electron density of close-proximity formation with $D_l = 1$ m, $V_f = 500$ V

The maximum instantaneous power requirement for four such simulations are shown in Figure 3.10 as predicted from Nascap-2k's tracked plasma current onto the follower surface. For this formation geometry, it appears that even voltages around 50 V have power requirements significant for common cubesatellite power systems. This potential is extremely small compared with the voltages sourced in electrostatic actuation, indicating positive charging is inherently expensive.

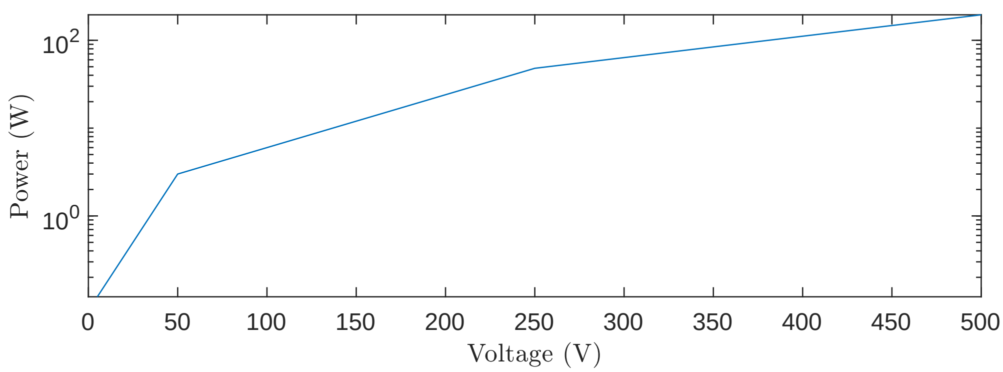

Figure 3.10: Maximum instantaneous power required to bias follower craft

An additional effect not considered here is the attenuation of the positive electric field in the wake's electron plasma. The results throughout this chapter indicate that positive charging is inferior to negative charging for the purpose of electrostatic actuation, so this effect is neglected.

3.1.4 Negative Charging in the Wake

The simulations above indicate that the feasibility of electrostatic actuation depends on the ability to source sufficient negative potentials such that relative orbit control is achieved without collapsing the wake. This motivates a parametric study wake behavior across leader ram area and follower potential. Only ion density is shown for the simulations run, as the large negative potentials will thin out the nearby electrons in a fairly predictable fashion.

The first parameter sweep shown in Figures 3.11-3.14 considers constant follower voltage -1000 V with increasing leader craft sizes. The follower is placed at 0.5 m for all simulations, as leader craft size not formation spatial scale is under consideration.

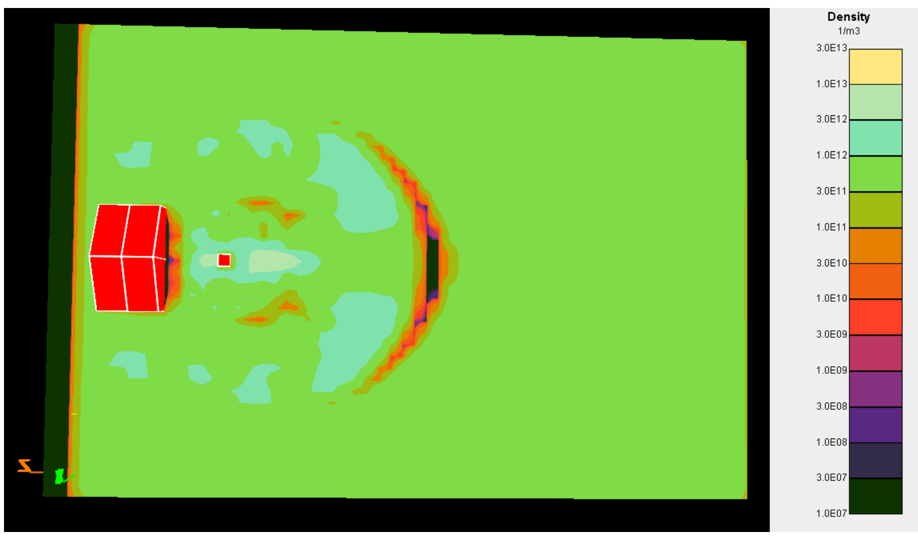

Figure 3.11: Ion density of close-proximity formation with D_l = 1 m, V_f = -1000 V

As a baseline, consider Figure 3.11 in which a cylindrical, uncharged small satellite with 1 m diameter leads a 10 cm cubesat charged to -1000 V — a reasonable follower voltage for electrostatic actuation. Note here that the wake has utterly collapsed in a way that would result in significant shielding between leader and follower unlike the collapse shown in Section 3.1.2.

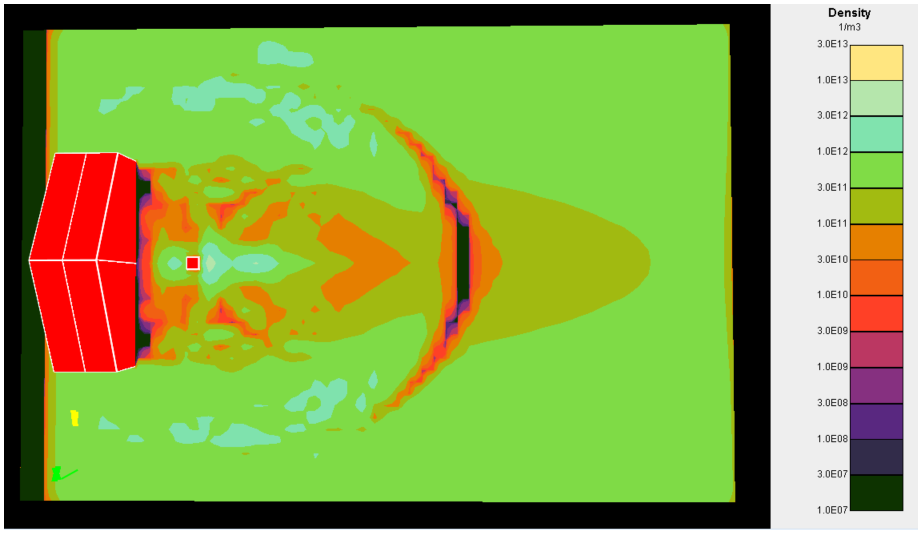

Figure 3.12: Ion density of close-proximity formation with R_l = 2 m, V_f = -1000 V

Holding the follower potential constant, progressively larger leader craft are considered in Figures 3.12-3.14 Wake collapse occurs for craft smaller than about 3 m at this potential for this geometry, indicating electrostatic actuation is not feasible for craft smaller than this without considering wake expansion techniques.

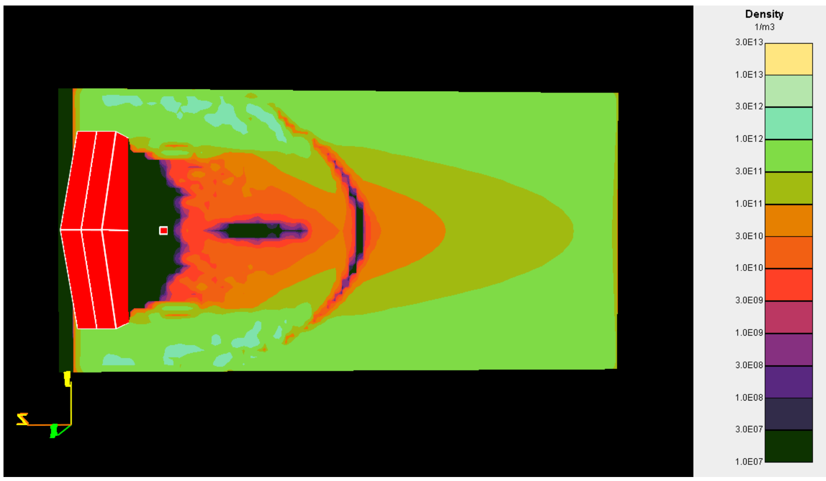

Figure 3.13: Ion density of close-proximity formation with R_l = 3 m, V_f = -1000 V

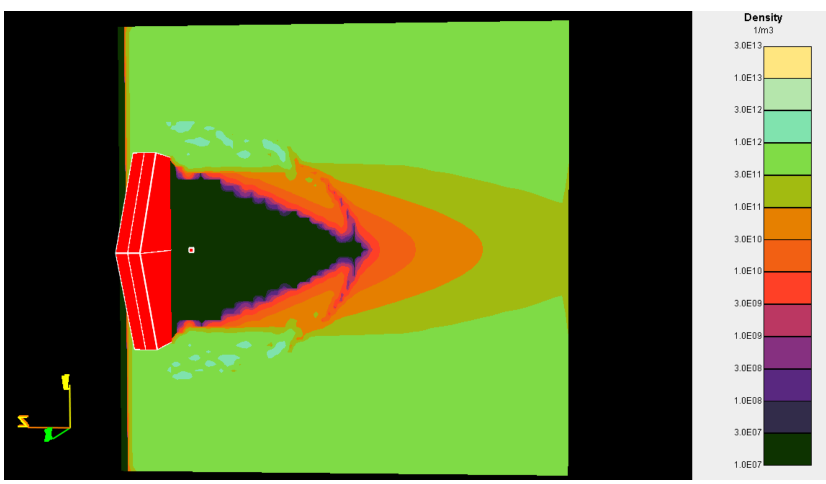

Figure 3.14: Ion density of close-proximity formation with R_l = 5 m, V_f = -1000 V

Figure 3.13 shows an edge case immediately before wake collapse occurs. Generally speaking, such critical configurations are difficult to find, as not analytic tools exist and simulations are instead run based on trial-and-error. Figure 3.14 shows a wake nearly unperturbed by the large potential within. This is an important result, as it indicates that a technological demonstration of electrostatic actuation behind a large spacecraft — the ISS, for example — would be unlikely to cause wake collapse.

Electrostatic actuation simulations discussed in the final chapter of this dissertation indicate that a follower voltage on the order of kilovolts is required to stabilize a cubesatellite in LEO. Given that the 3 m craft did not experience wake collapse an investigation of ion density and power is conducted across increasing follower voltages for this leader size.

Figure 3.15 shows the described geometry for -2000 V follower bias. This potential increase relative to the simulation in Figure 3.13 results in wake collapse. Given that this is still a reasonable voltage for electrostatic actuation applications, it is determined that a larger leader diameter than 3 m is desired. Few such craft exist, motivating consideration of techniques for expanding the wake region

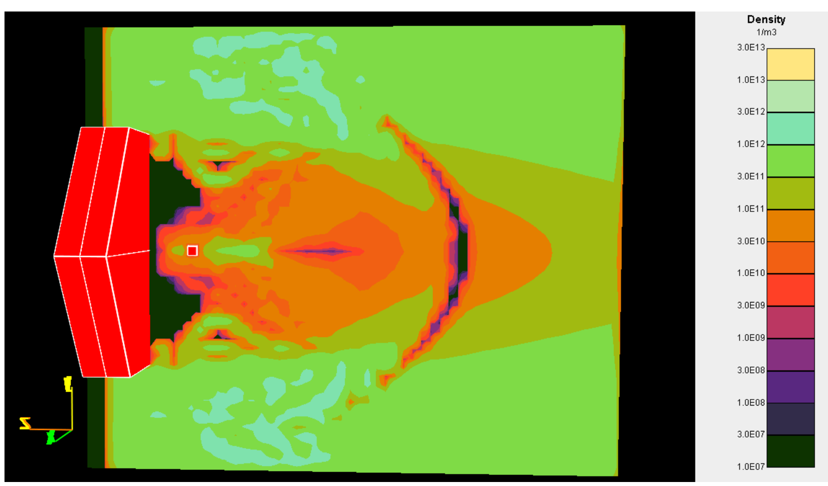

Figure 3.15: Ion density of close-proximity formation with R_l = 3 m, V_f = -2000 V

The power requirements the parametric study described in this section are shown in Figures 3.16 and 3.17. The two sweeps share a point in common ($R_l = 3$ m, $V_f = -1$ kV). The leader diameter sweep shows the expected behavior for wake collapse — namely a steep decrease in power consumption when the wake does not collapse.

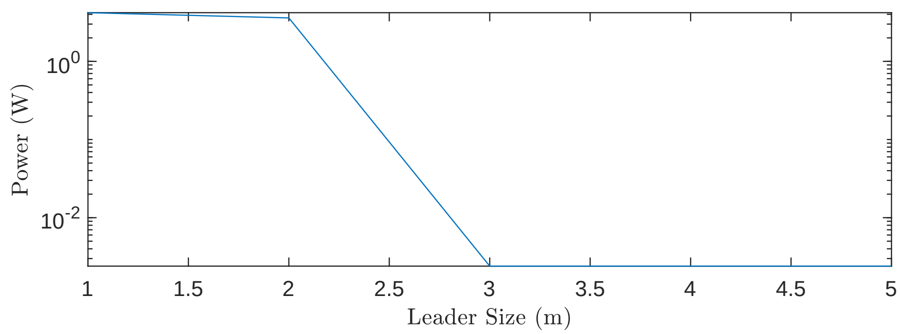

Figure 3.16: Maximum instantaneous power required to bias follower craft to -1 kV for various leader sizes R_l

Figure 3.17 on the other hand does not match intuition, as very low power is sourced onto the follower craft even when wake collapse has occurred. This occurs because the motion of the ions become dominated by the electrostatic energy, causing them to shoot off in hyperbolic orbits with the follower craft at the focus rather than impinge on the spacecraft surfaces. This low power cost does not make electrostatic actuation in collapsed wakes feasible, as Figure 3.15 indicates near-ambient plasma densities between the leader and follower. The 2 mm Debye length based on the environment definition indicates that electric fields would die off rapidly in the space between the leader and follower.

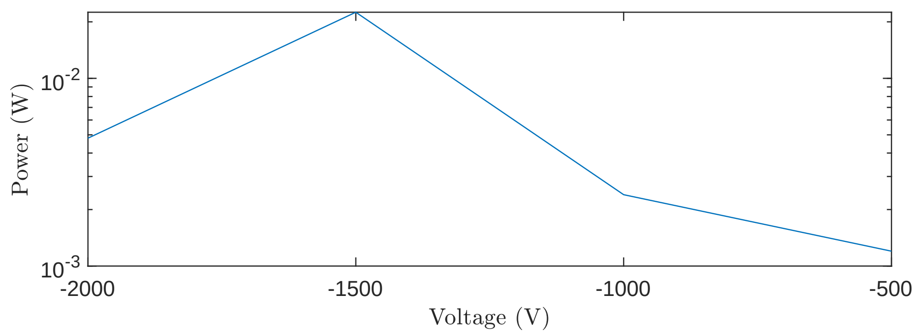

Figure 3.17: Maximum instantaneous power required to bias follower craft to various voltages for leader diameter of 3 m

3.1.5 Wake Expansion

The results presented thus far in this chapter indicate that electrostatic actuation in LEO must be applied in plasma wakes. Nascap-2k simulations motivated the use of negative potentials due to power considerations, but also showed wake collapse behind extremely large craft for relative small follower voltages. This motivates the development of techniques to expand the plasma wake without substantially increasing the ram-facing area.

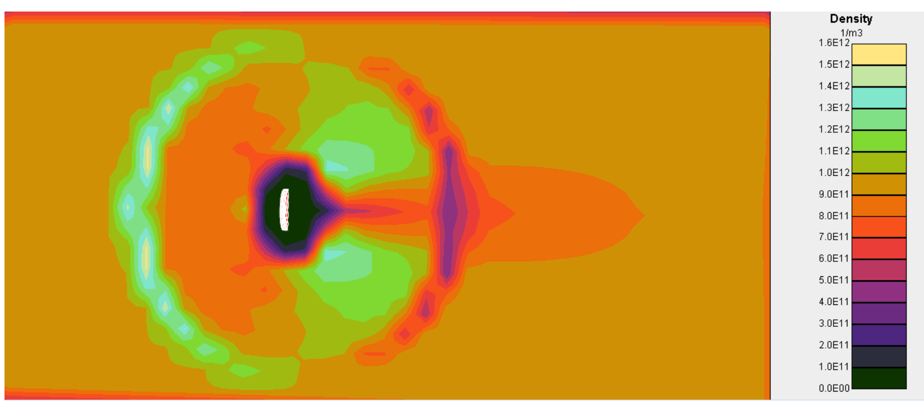

Figure 3.18: Ion density near craft charged to 10 V positive

Consider Figure 3.18. Here, a leader craft of diameter 1 m charges to 10 V, resulting in an expanded ion wake. While this enables a larger working volume for electrostatic actuation techniques, the expanded wake shown in Figure 3.18 comes at the cost of $\sim$ 80 W power draw. This is in part due to the extremely large surface area of the craft shown. This motivates consideration of thin, positively charged structures. Nascap-2k and similar methods struggle in simulating such objects. Therefore, experimental methods are applied.

3.2 Plasma Wake Shaping Experiments

This section describes a set of experiments conducted to determine the effectiveness of wake expanding and shaping using applied voltages and sparse geometries. A detailed explanation of these experiments is followed by a discussion of the data analysis method applied to the measurements of the wake. Two different experimental campaigns are described with different motivations and results. In both cases, geometries were considered not feasible investigate with Nascap-2k or similar software packages, as they include thin materials of dimension ~ 1 mm. These experimental campaigns therefore provide unique insight into feasible application of electrostatic actuation in LEO.

3.2.1 Experimental Comparison of Sparse and Solid Geometries

The first set of experiments described investigate the wakes behind solid objects of large positive and negative voltages. These are compared with results from a sparse object of similar geometry. The plasma parameters in the vicinity of these objects are measured and conclusions drawn for the effectiveness of sparse geometries for wake shaping.

3.2.1.1 Methods

Plasma wake experiments were conducted within the JUMBO chamber at the Spacecraft Charging Instrumentation and Calibration Laboratory (SCICL) at the Air Force Research Laboratory (AFRL) at Kirtland Air Force Base, NM. JUMBO is a 2 m diameter cylindrical chamber with length of roughly 3 m and is described in greater detail in [22]. The plasma source manufactured by Plasma Controls LLC uses magnetic filtering to produce a representative LEO plasma — one in which the velocity of the streaming, directional ions (5 eV) is roughly equivalent to the relative velocity of a LEO spacecraft with respect to ionospheric ions. Argon gas is ionized by a filament within the source to generate the ions which are then accelerated to the desired velocities by a system of charged grids. Argon is chosen because its mass is representative of the higher-concentration elements within the ionosphere and because Ar^+ is not as corrosive as elements such as O^+. This source is not differentially pumped, meaning that neutral Argon atoms are present within the flow, potentially allowing for charge exchange between the fast-moving ions and the slow neutrals.

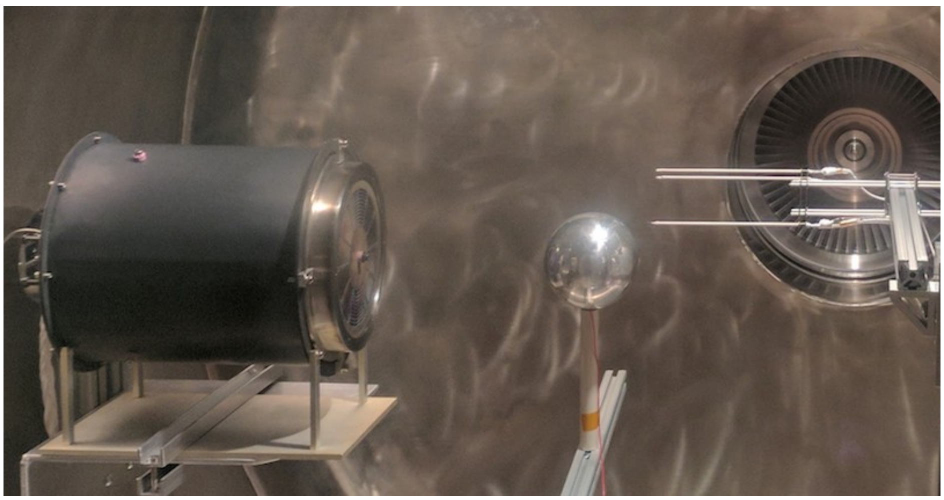

Figure 3.19: Wake Experiment Setup

Figure 3.19 shows the experimental setup. The plasma source is on the left. In the center is a solid, conducting sphere of radius 10 cm about which the wake is generated. On the right is a spherical Langmuir probe of radius ∼4 mm affixed to a 3-dimensional translation stage. A measurement is taken at each point of a 3-dimensional grid beginning 1 mm behind the spherical conductor and extending for 6.5 cm. This provides a measurement of the wake. The I-V curve from the Langmuir probe is measured using a Keithley 6487 Source-Measure Unit (SMU). This model is capable of measuring currents on the order of femtoamps given the right equipment and conditions. However, given the experimental parameters and available equipment, the lowest reliably-measurable current was 10^{-8} A.

Four experiments were carried out to investigate the wake structure under various voltages

Figure 3.20: Sparse Sphere for Experiment D

and geometries. Table 3.1 provides the values used in these experiments.

Table 3.1: Experiment Descriptions

Experiment	**Applied Voltage (V)**	**Experiment Article**
A	-1 (V_{Float})	Solid Conducting Sphere
B	-50	Solid Conducting Sphere
C	50	Solid Conducting Sphere
D	50	Sparse Conducting Sphere

The general experimental procedure was to allow the Jumbo chamber to reach its base pressure ($\sim 5 \times 10^{-7}$ Torr) then start the plasma source. The pressure would then rise until it reached a steady state value between 10^{-6} and 5×10^{-5} Torr. As discussed previously, the source is not differentially pumped, so charge exchange leading to a bi-modal ion energy distribution unrepresentative of the LEO environment is a concern. Research grade (99.9995%) Ar was used for all experiments. The closed nature of the gas delivery system coupled to the significant rise in pressure after the source is activated indicates that Ar and Ar^+ are the dominant constituents. Therefore, charge exchange between these two species will dominate. Reference [95] shows that the cross section for Ar-Ar^+ charge exchange reactions at 5.6 eV is 3.1×10^{-19} m^2. To consider a worst-case scenario, a pressure of 5×10^{-5} Torr is assumed. Converting this pressure into density is complex, as the temperature distribution of the two populations (Ar and Ar^+) are not well known. Again assuming worst-case parameters, all particles are considered to have a temperature of 5 eV, though the neutrals in the chamber are likely much less energetic as they are not accelerated by the grids in the source. The ideal gas law in used to calculate the number density within the chamber given its geometry and the worst-case pressure and temperature values.

$$n = \frac{p}{kT} = 4.05 \times 10^{15} \tag{3.2}$$

Finally, a conservative bound on the mean free path for a charge-exchange reaction is calculated.

$$\lambda_{\text{cc}} = (n\sigma_{\text{cc}})^{-1} = 796 \text{ m} \tag{3.3}$$

Given that the characteristic lengths of the experiment is on the order of ∼10 cm and the value shown above is conservative, it can be reasonably assumed that charge-exchange reaction are extremely rare, and therefore the energy distribution is predominantly uni-modal as in LEO.

Another potential experimental artifact that could lead to an environment unrepresentative of LEO is secondary electron generation at the chamber walls. Reference [68] indicates that the secondary electron yield due to bombardment of 10 eV Ar^+ is less that 0.1, and is vanishingly small for neutral Ar bombardment at the same energy. Given that the experiment was carried out many Debye lengths from the chamber walls, and the secondary electron yield is low at the relevant energies, it is concluded that secondary electrons do not significantly affect the results presented below.

The plasma source operating conditions are listed in Table 3.2.

Table 3.2: Plasma Source Voltages & Currents

Source Property	**Value**
$V_{\text{Discharge}}$ (V)	30-40
$I_{\text{Discharge}}$ (A)	0.9
V_{Keeper} (V)	15-20
I_{Keeper} (A)	1
Mass Flow Rate (sccm)	10

The parameters given in Table 3.2 generate a plasma with density of roughly 10^{14} m^{-3} at the experiment location. These properties are consistent with the calibration provided by Plasma Controls LLC [28] and an independent calibration performed within SCICL [67]. While the density reported in the experiments below is higher than these calibrations, they were performed at distances much farther from the source. Table 3.3 shows the density given the source parameters at three different locations along the axis of the chamber. The decrease in density as the distance from the source increases is qualitatively consistent with the expansion of plasma in vacuum described by [62].

Table 3.3: Ion Density Measurements

Measurement Source	**Distance (cm)**	**Ion Density (m^{-3})**
Experiment A	20	$\sim 2 \times 10^{14}$
SCICL	40	$\sim 7.5 \times 10^{13}$
Plasma Controls LLC	100	$\sim 7.5 \times 10^{12}$

The experiments were carried out close to the source in order to attain this higher density. The goal of this investigation is to gain insight into the wakes forming behind LEO objects of varying geometries and voltages. Consider a small satellite with radius 1 m flying through a LEO plasma of density 10^{12} m^{-3}. Applying the body scaling transformation described by [19] given the experiment articles' radius of 10 cm, the required experiment ion density to achieve self-similarity is calculated.

$$n_{\text{Exp}} = \left(\frac{r_{\text{LEO}}}{r_{\text{Exp}}}\right)^2 n_{\text{LEO}} \approx \left(\frac{1}{0.1}\right)^2 10^{12} = 10^{14}\ \text{m}^{-3} \tag{3.4}$$

Therefore, the higher experiment density provides insight into the wake behind a LEO small satellite.

It is worth noting that, while the plasma source is expected to have directionally streaming ions at roughly 5 eV, no calibration is provided to validate this. Characterization of the source is an ongoing effort. Additionally, the calibrations performed by both SCICL and Plasma Controls LLC report an electron temperature of ~0.2 eV independent of distance from the source. Due to fitting challenges in the Langmuir probe analysis used in this work which especially affect the electron temperature calculation, the calibration value (0.2 eV) is assumed accurate.

Given this ion drift energy (E_d) and electron thermal energy (T_e), the Mach number can be calculated from the ratio of the ion drift velocity V_d and ion acoustic velocity C_s.

$$M = \frac{V_d}{C_s} = \frac{\sqrt{2E_d/m_{\text{Ar}}}}{\sqrt{2T_e/m_{\text{Ar}}}} = \sqrt{\frac{E_d}{T_e}} = \sqrt{\frac{5}{0.2}} = 5 \tag{3.5}$$

While this mach number is slightly smaller than the M=8 for LEO objects, the experiments described below still achieve supersonic ion flow around an object. For this and other reasons, the results below are not considered identical to those in LEO, but provide insight into spacecraft-plasma interactions nonetheless. While the resulting wake from this Mach number will be smaller in size and more squat in dimension, the wake will behave similarly until collapse occurs. The potential and location at which this happens can be used to inform estimates for the $M = 8$ circumstance in LEO.

Figure 3.20 shows the sparse sphere used as the wake-forming object in experiment D. This spherical object has a radius of approximately 10 cm — the same as the solid sphere used in other experiments. The object was made by spot welding stainless steel wires into a spherical shape.

As seen in Figure 3.19, the plasma source is located at one end of the chamber and is aligned perpendicular to the axis of the chamber. Based on the Langmuir probe data collected, the grounded rear and side of the chamber are at approximately -1 V with respect to the plasma, meaning that the ions in the plasma flow are attracted to the walls, sides, and floor of the chamber, while the electrons are repelled. This is seen in the data shown in the next section.

Each Langmuir sweep taken throughout all experiments spans -10 V to 10 V with 50 equally spaced points at which current measurements are taken throughout each sweep. These limits were chosen to be large compared with the constituents' energies and plasma potential so that electron and ion current saturation would be reached at the positive and negative limits of the sweep, respectively. Each sweep runs from negative to positive. The integration time on the Keithley 6487 SMU is set to minimize the sweep time while maintaining enough accuracy to collect quality data. Each sweep takes less than one second and is separated from the previous sweep by the amount of time the 3-dimensional translation stage requires to move 1 cm to the next grid point — about 1 second. The floating potential on the charged conducting sphere was determined empirically using a non-contact electrostatic field probe (Trek model 341B). This device can accurately measure voltages at sub-volt levels but due to the limitations of the voltage display panel, shows only a single digit of precision. This means that, while the Trek unit indicated a floating potential of -1 V, the actual value is bounded between 0 V and -2 V. This error source has little bearing on the experimental results, as the goal of Experiment A was to provide a baseline measurement for the wake behind a passively-charged object. Knowledge that the experiment was carried out at a low, negative voltage is sufficient for this investigation.

3.2.1.2 Data Analysis

The Langmuir curves generated by the Keithley 6487 SMU are analyzed using the method described by [8] in which the 4-parameter fitting function shown in Equation (3.6) is fit to the data and used to extract the properties of the plasma. This method was chosen because it is a simple and computationally efficient fitting method that provides reasonable fits for smooth I-V curves such as that shown in Figure 3.21. Given the large data volume, computation efficiency was required to analyze the data on a reasonable time frame.

$$I(V) = \exp\left[a_1 \tanh\left(\frac{V + a_2}{a_3}\right)\right] + a_4 \tag{3.6}$$

Here, V is the probe potential and the a_i are the fitting parameters. This fitting method provides varying degrees of success, and the amount of data collected prohibits individual tuning of fit parameters. Figures 3.21-3.23 shows examples of experimental data. Note that the RMS of the fit residuals is indicated within the caption on each figure.

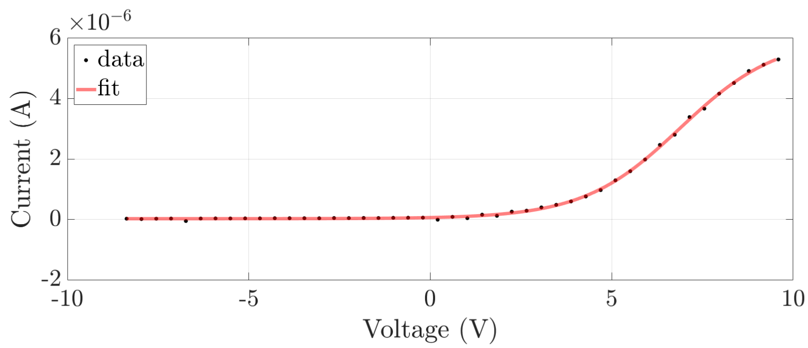

Figure 3.21: Instance of Good Fit to Reliable Data (RMS = 6.3568×10^{-3})

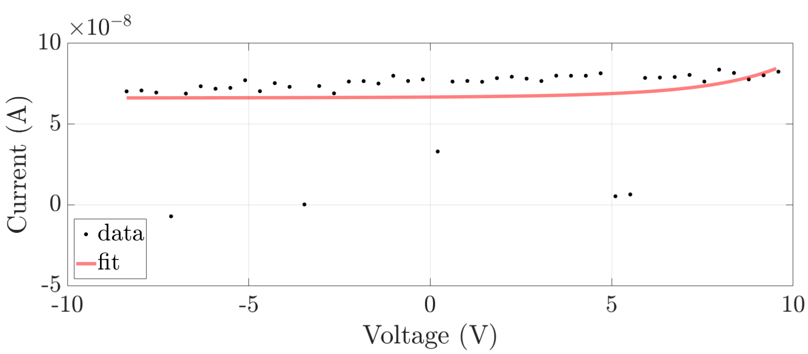

Figure 3.22: Instance of Fit to Unreliable Data RMS = 2.6292×10^{-1})

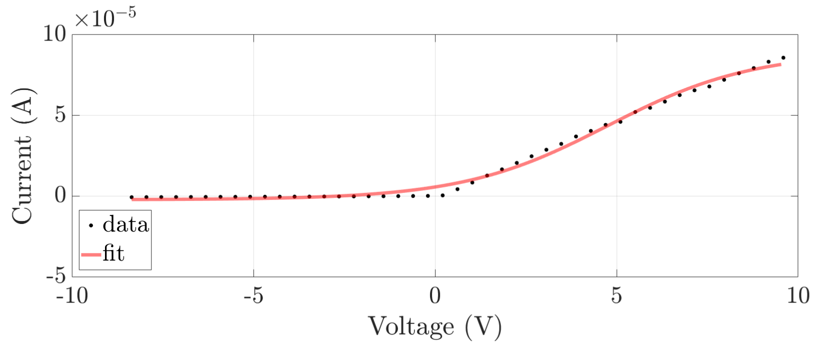

Figure 3.23: Instance of Bad Fit to Reliable Data (RMS = 2.6656×10^{-2})

Figure 3.21 shows a data set that is well described by Equation (3.6). The plasma properties extracted according to reference [8] for similar data sets are considered accurate as they are consistent with calibrations as discussed previously. Figure 3.22 shows a case where the detector floor was hit, providing unreliable data that the model is nevertheless able to fit. Data sets with RMS fit residuals greater than 3.50×10^{-2} are excluded from the data set. This value was chosen to eliminate significant outliers from the data sets discussed below (i.e. a significant increase in density between two adjacent measurements).

Due to the large amount of data collected, each fit cannot be considered individually. The RMS value provides a good means of identifying good fits from poor, but given that plasma properties are extracted from different voltage regimes within each Langmuir probe sweep, the RMS value does not provide the full picture. For example, a data set whose fit is good on the negative end of the I-V curve will provide an accurate measure of the ion density of the plasma, while that same fit may be poor in the positive regime and therefore provide inaccurate values for the electron density and temperature. This is seen in Figure 3.23, as the fit is much better for negative voltage values than for those from roughly -1 V and above.

Additionally, the properties of the wake described previously — such as its non-quasi-neutral nature — mean that many of the assumptions outlined in [8] and other conventional Langmuir probe analyses are invalid. Future iterations of this work will investigate the use of different fitting and analysis methods to determine the plasma properties in the wake. This investigation is primarily concerned with the feasibility of changing the wake geometry, rather than precise determination of the wake properties.

Each of the experiments outlined in Table 3.1 consist of a Langmuir probe sweep taken at the nodes of a 3-dimensional grid. Only the measured densities are considered in this section, as the fitting challenges discussed in the previous section especially affected the electron temperature measurement. Additionally, the wake is most recognized for the ion density decrease relative to ambient, so this geometrical investigation can continue without consideration of the electron temperature.

Each of the figures shown below is oriented as is the experiment in Figure 3.19 — with the plasma flowing from left to right. Additionally, a circle of radius equal to the radius of the conducting sphere is superimposed on the plots to show the size of the wake relative to the wake-forming object. The Z = 0 cm plane shown on the far left of each of Figures 3.24-3.37 begins directly behind the charged conducting sphere.

Note that each experimental result figure shows the electron and ion densities decreasing as the Z distance increases. This is because the plasma is expanding into the JUMBO chamber. This could affect the wake closure distance. Reference [62] provides a method of describing how ambient plasma expands, but the detailed analysis required to reconcile this aspect of the experiment with the wake physics is not within the scope of this investigation.

Finally, the ion-deficient nature of the wake means that shielding effects are asymmetric with respect to potential, as described in [27]. Therefore, the negative potentials applied to the Langmuir probe while in the wake could affect a significantly larger portion of the plasma than in ambient. Shielding effects are reduced in the positive regime as well, meaning that the sheath about the probe is larger, leading to increased current collection when the probe is charged positive. This in part describes the electron density enhancements seen in the wake in the figures below, though arcing and similar events are also sources of such inaccuracies. The short integration time discussed previously was used in part to mitigate this effect, but sampling on timescales less than the plasma frequency (roughly 10^8 Hz) was not possible with the Keithley 6487.

3.2.1.3 Experiment A

The goal of experiment A is to provide a baseline for the nominal wake behind a spacecraft in LEO. The spherical mock spacecraft shown in Figure 3.19 is allowed to float at a measured potential of roughly -1 V. The grid size beyond Z = -3cm is reduced due to time constraints for this experiment.

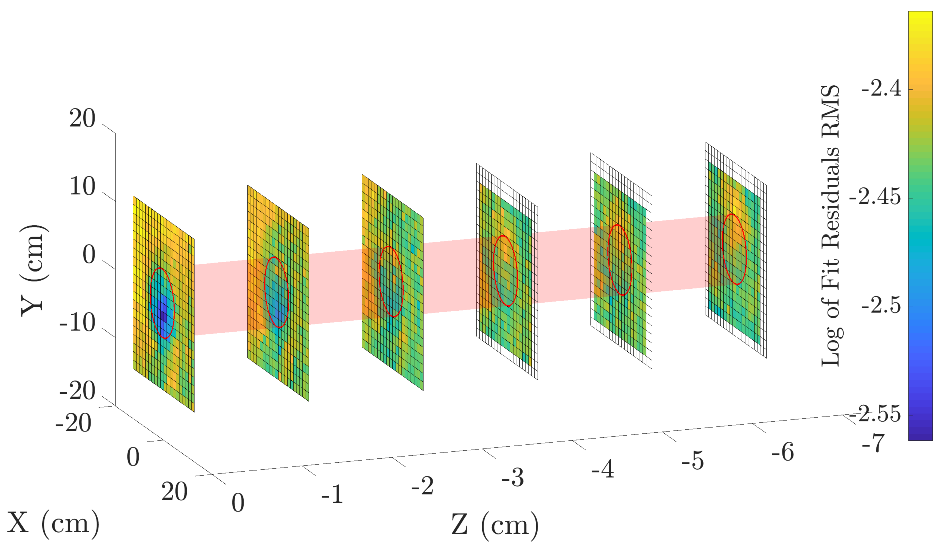

Figure 3.24: Residuals RMS for Experiment A

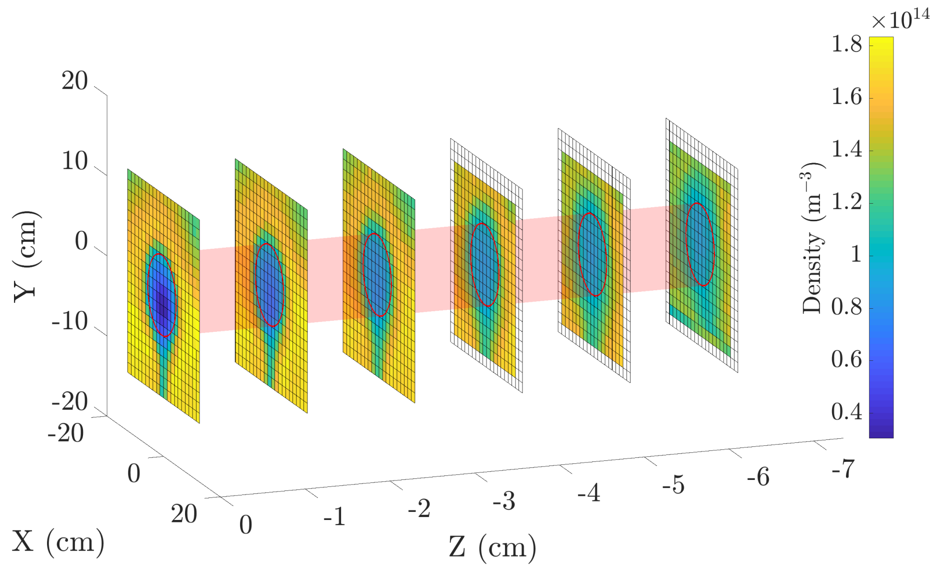

Figure 3.25: Ion Density for Experiment A

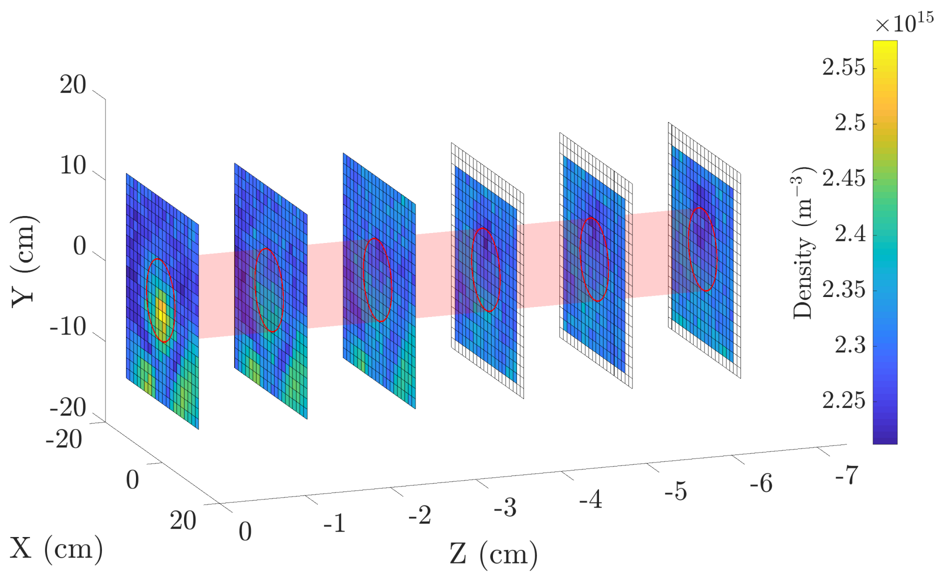

Figure 3.26: Electron Density for Experiment A

Figure 3.24 shows the RMS of the fit residuals for each measurement point in experiment A. Note that, for this and other RMS residuals plots, the colorbar has a logarithmic scale, meaning that the RMS values for this experiment are all quite small. This means that, according to the theory described in [8], the plasma parameters collected throughout this experiment should be reasonably accurate. Recall, however, that this RMS value does not indicate which parts of the Langmuir curve are well-fit and which are not. Instead, comparison with previous experiments, simulations, and theoretical work on spacecraft wakes will be applied to better interpret the data.

Figure 3.25 shows the ion density measured across the grid space. The results here indicate a decrease of $\sim 75\%$ in ion density in the wake relative to ambient. This qualitatively matches previous experimental and simulation data presented in [71, 60] among others, though the former of these present current rather than plasma parameters. Reference [96] describes that the disturbed region of a LEO plasma wake begins after the first mach line — defined as the line beginning at the RSO's edge with slope $\sim 1/M$. Figure 3.27 shows the relevant lines drawn over the ion density of experiment A in the Y=0 cm plane given the Mach number calculated in Equation (3.5). A linear interpolation scheme is applied in this figure (though not in the experiments) for clarity. Note that these Mach lines bound the disturbed region as defined by a significant ion density decrease indicating that the wakes in experiment A have shape relevant to those in LEO. This property is important in assessing similarities with the on-orbit case, as the purpose of this investigation is to better understand wake shaping under various spacecraft voltages and geometries.

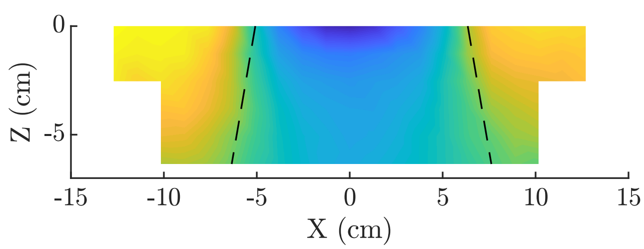

Figure 3.27: Ion Density Along the Y=0 cm Plane of Experiment A Including Appropriate Mach Lines

As discussed previously, no consensus method exists for Langmuir probe analysis in plasma wakes. Therefore, a comparison with reference [71] — which reported normalized ion current in the wake of Atmospheric Explorer C — provides a better indication of whether experiment A agrees with on-orbit data of LEO wakes. Consider Figure 3.28, which shows the ion current collected by the Langmuir probe at ~ -5 V along an arc directly behind the solid sphere normalized by the ambient ion current. Wake center is at $\theta = 180°$.

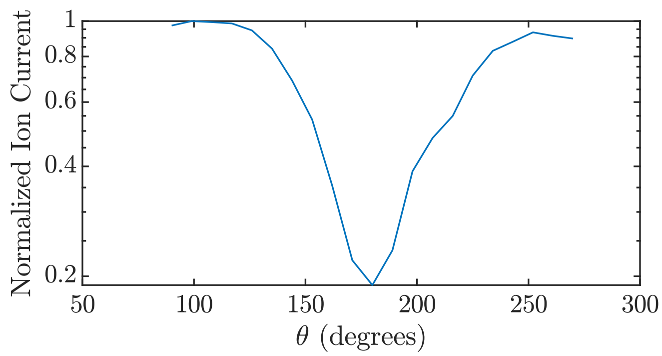

Figure 3.28: Normalized Ion Current by Angle Directly Behind Solid Sphere

The figure above shows a similar ion current dependence on angle to those in [71], including the large density changes beginning and ending between $120° - 130°$ and $230° - 240°$, respectively. Notably different between the two experiments is the magnitude of density difference between the deep wake and ambient. This discrepancy results from a variety of differences in experimental setup, primarily the physical size and different detectors of each. The data presented in reference [71] is collected using an ion mass spectrometer, which results in significantly different potential contours within the wake than the Langmuir probe system described above. This causes large differences in the ion current collection, as particle trajectories are altered as they pass through these potential contours. This effect is compounded by the much smaller physical scale of experiment A compared with the on-orbit data collected by Atmospheric Explorer C. Given the inefficiency of the shielding of negative charges described in reference [27] in an electron-dominated plasma, the potential near the Langmuir probe in experiment A is expected to fall of as $\sim 1/r$. Given the close proximity of streaming ions to the probe at -5 V due to the small scale of the experiment, a larger ion current is expected as ions fall into the generated potential well.

Despite this difference, the validation of the shape of the wake shown in Figure 3.27, the general trend of angular dependence in Figure 3.28, and the facility analysis presented in Section 3.2.1.1 are taken as sufficient evidence that the wake shown in Figures 3.25 and 3.26 is representative of a LEO wake for the purposes of this investigation.

The electron density measurements shown in Figure 3.26 indicate an enhancement in the wake, which is not predicted by previous work and is assumed to be an experimental artifact. The electron density which is determined from the positive voltage end of the Langmuir sweep called the electron saturation region also seems to be fit poorly in the sense of Figure 3.23. This could lead to a miscalculation of the electron density resulting in the enhancement seen in the data. Additionally, the shielding within the wake discussed previously could lead to increased current collection in the positive end of the Langmuir sweep, erroneously implying larger density values.

3.2.1.4 Experiment B

Experiment B was motivated by a desire to understand whether the closing distance of the wake can be shortened by charging the craft negatively with respect to the surrounding plasma. To understand the usefulness of such a technique, consider a docking scenario in which two charged spacecraft are approaching one another in the along-track direction. Reference [44] describes a plasma contactor which ejects plasma to discharge spacecraft. However, if the wake can be made smaller so the ambient plasma envelops the follower craft, the potential difference between the crafts can be lessened without including these additional systems. The -50 V potential was chosen because it is large compared to the thermal energy — or relative kinetic energy on orbit — of the plasma, and because spacecraft naturally charge to larger negative voltages than this on orbit [2].

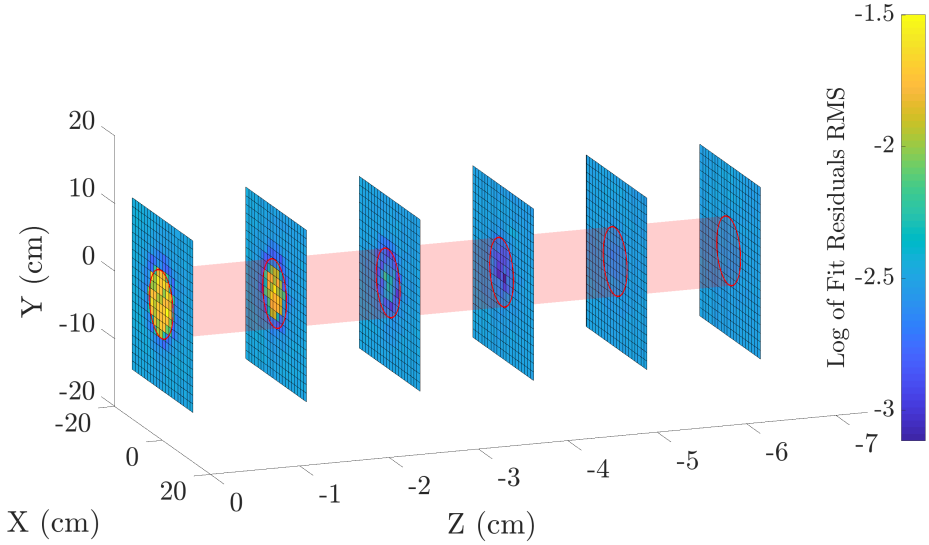

Figure 3.29: Residuals RMS for Experiment B

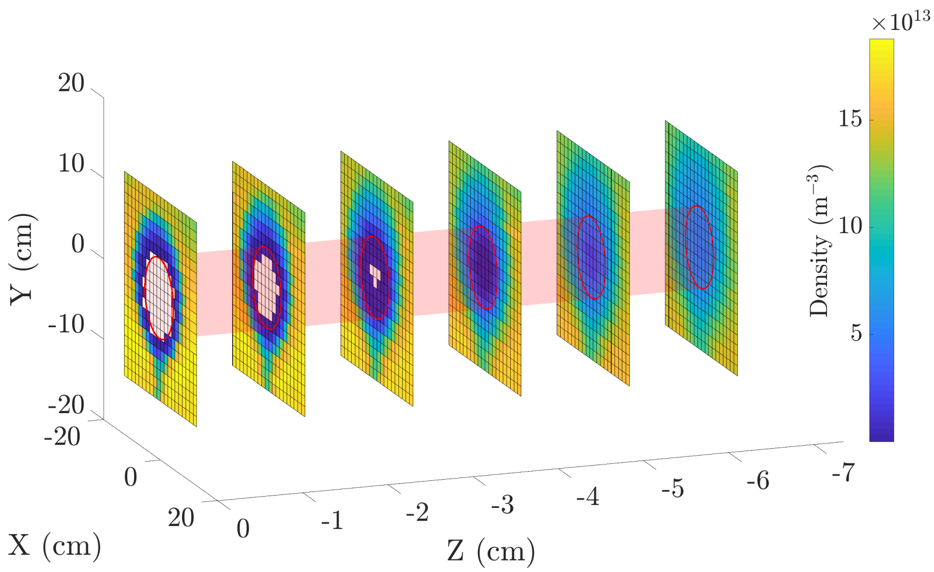

Figure 3.30: Ion Density for Experiment B

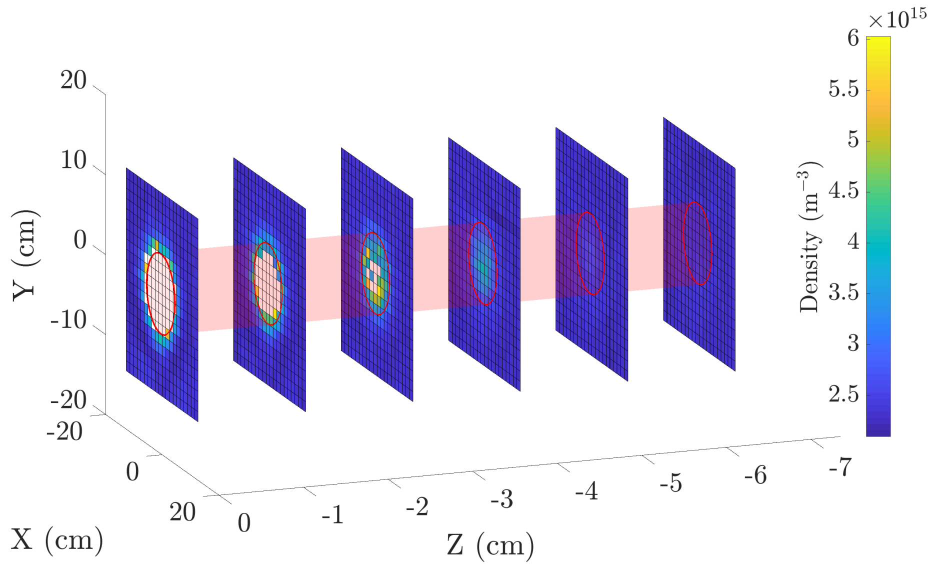

Figure 3.31: Electron Density for Experiment B

Note that the RMS fit residuals in the wake shown in 3.29 are much larger than those previous. This results from extremely low plasma density in the wake for this experiment — i.e. most Langmuir sweeps in the wake resemble Figure 3.22. While this precludes discussion of wake properties arising from this scenario, it does provide geometric information regarding closure of the wake. This can be seen in Figure 3.30.

Contrary to the expected result, charging the spacecraft negative made the closing distance of the wake larger. This is likely because the sheath surrounding the conducting sphere is large, collecting more ions than would a more positively charged object. This hypothesis could not be validated because the Agilent E3633A power supply used to charge negative did not have current resolution small enough to measure the ion current onto the sphere.

Another interesting result is the ‘deepening’ of the wake. This term is used henceforth to indicate a more significant ion density decrease relative to ambient than that shown in Figure 3.25. This is likely because any ions that are able to penetrate into the wake are promptly attracted to the negatively charged sphere and absorbed.

The electron density shown in Figure 3.31 evidences the data reliability and fitting issues described previously resulting from reaching the floor of the detector and the limit of the Langmuir probe analysis method described by reference [8], respectively. The ambient density matches those shown in Figure 3.26. A significant density enhancement is still seen in the few measurements near the wake that were fit well by Equation (3.6).

3.2.1.5 Experiment C

The 'enhanced' wake generated behind a positively charged object is discussed on pages 56-57 of reference [48]. Expanding the wake creates a larger region amenable to electrostatic actuation, so the extent to which this can be accomplished with reasonable charge levels is a subject of interest. As with the previous experiment, the power requirements to hold the conducting sphere at the desire potential could not be measured. However, experiments such as [21] have charged positive by 100s of volts in LEO, so a voltage of 50 V should be attainable. The expanded grid shown in the figures below was chosen in the hopes of capturing the entirety of the wake for this voltage regime.

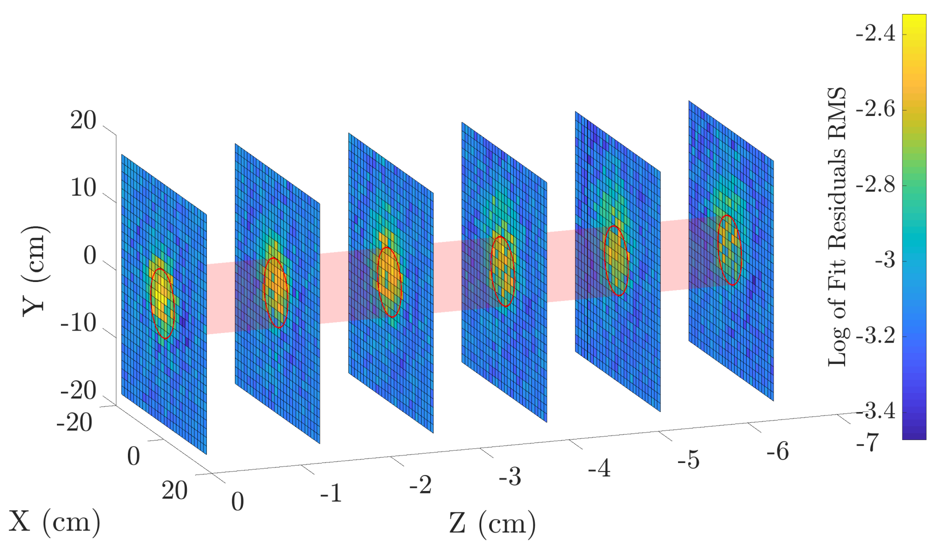

Figure 3.32: Residuals RMS for Experiment C

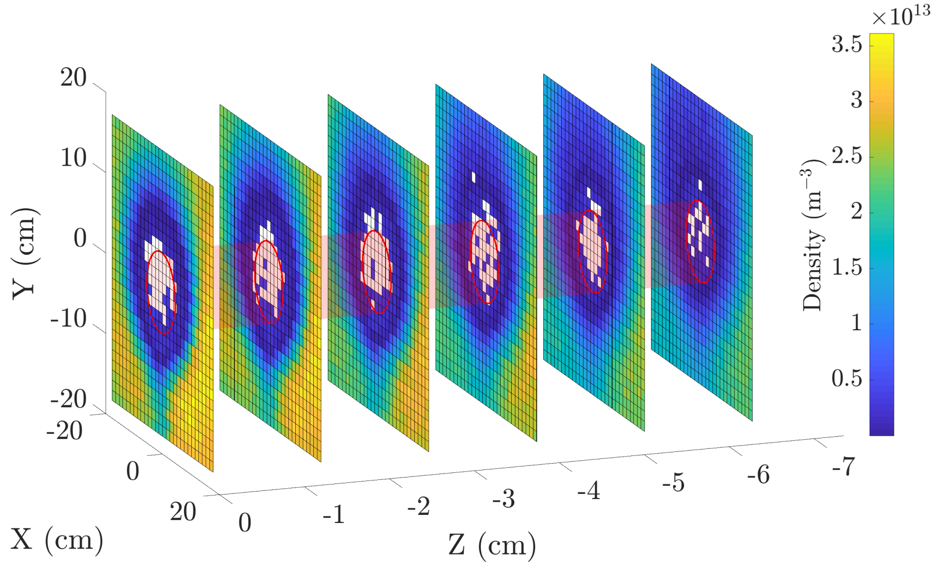

Figure 3.33: Ion Density for Experiment C

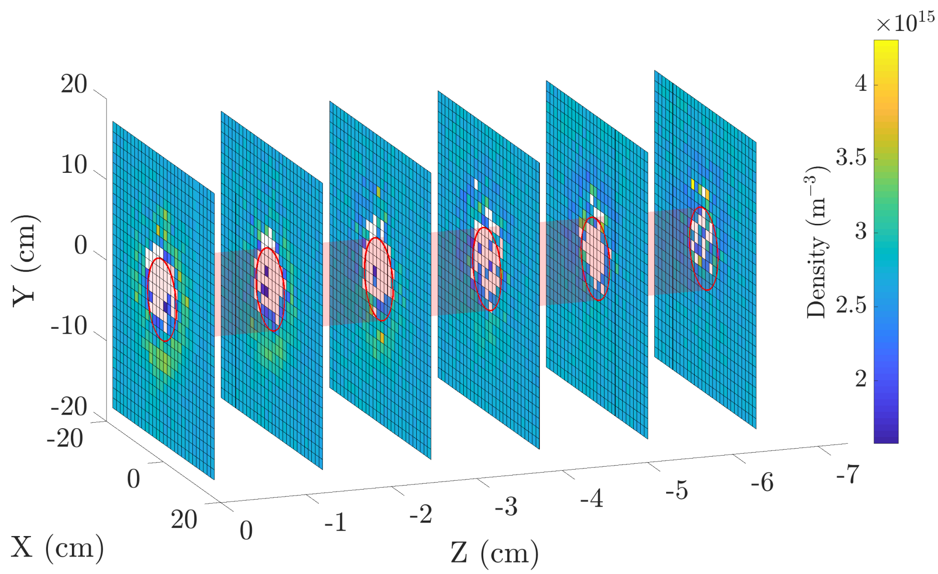

Figure 3.34: Electron Density for Experiment C

Figure 3.32 indicates that the general fit quality expressed by the RMS residual values in this experiment should be similar to that in experiment A. However, additional checks on the second derivative of Equation (3.6) given the fit parameters eliminate data sets that had good RMS values, but do not provide realistic plasma properties.

The wake region indicated by the ion density decreases in Figure 3.30 is significantly larger for this experiment than those previous. This matches intuition, as the potential on the conducting sphere is about an order of magnitude higher than the expected thermal energy of the ions leaving the source. Note, however, that the out-of-wake ion density shown in Figure 3.33 is roughly an order of magnitude smaller than those measured in the previous experiments shown in Figures 3.25 and 3.30. This indicates that the 50 V charged conducting sphere significantly alters the local plasma environment. Whether this circumstance is representative of what would happen in space or is an artifact of the experiment is unknown. Additional characterization of the source and the plasma flow into JUMBO must be undertaken before these and other questions can be answered.

Another feature to note in Figure 3.33 is the extension in the closing distance of the wake. Indeed, it doesn't appear to be closing as is seen in the previous experiments. Rather, it seems that the out-of-wake plasma is thinning and approaching the wake density. As with the X and Y grid dimensions, the Z distance for this experiment was significantly increased compared with the others described in Table 3.1. Visualization of this data is not extremely useful, as the crowding of the contour slices obscures the relevant features. However, the wake shown in Figure 3.33 does close after roughly 10 cm. This is significantly farther than Figures 3.25 and 3.30. This indicates that the wake can indeed be expanded significantly by charging the wake-forming craft positive.

The ambient electron density for this experiment is reminiscent of the experiments described above. As with Figure 3.31, the fit and data quality in the wake is low, meaning that the slight density enhancement is likely an artifact of the analysis method.

3.2.1.6 Experiment D

The final experiment is the crux of this investigation. Here, a sparse sphere pictured in Figure 3.20 is used to create the wake. It has similar dimensions to the charged sphere used previously and is also held at 50 V. This object is not a perfect sphere, which creates the interesting wake shape seen in Figure 3.36.

As discussed above, the electrostatic actuation techniques require a wake that is large compared to the object within it. Additionally, a larger wake means that the electric field of the charged sphere — whether solid or sparse — is interacting with more of the plasma and exchanging momentum. The goal of experiment C was to determine if a larger wake could be created by charging a craft positive, rather than increasing cross-sectional area and therefore its mass and cross sectional area. Experiment D goes a step farther in investigating whether the wake can be expanded by the use of thin, charged structures — which have low mass and cross sectional area. If this can be accomplished, a craft can enhance its wake without increasing area-dependent perturbations. Additionally, large wakes could be generated behind small, lightweight craft, making electrostatic actuation in LEO more applicable to a range of missions.

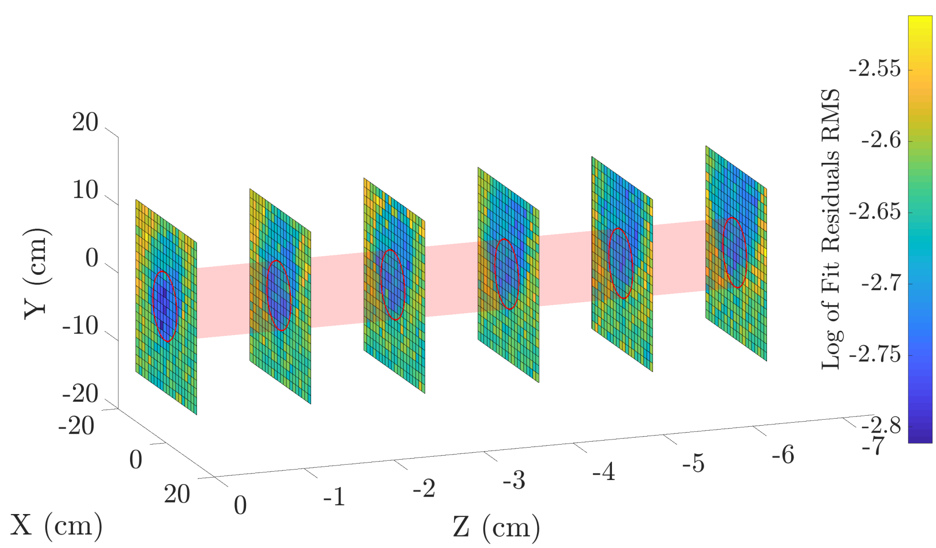

Figure 3.35: Residuals RMS for Experiment D

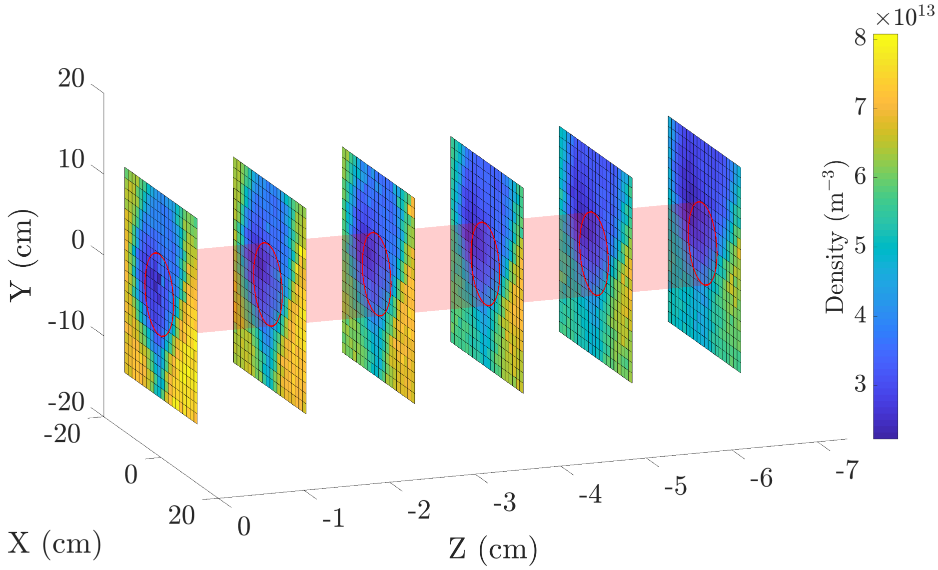

Figure 3.36: Ion Density for Experiment D

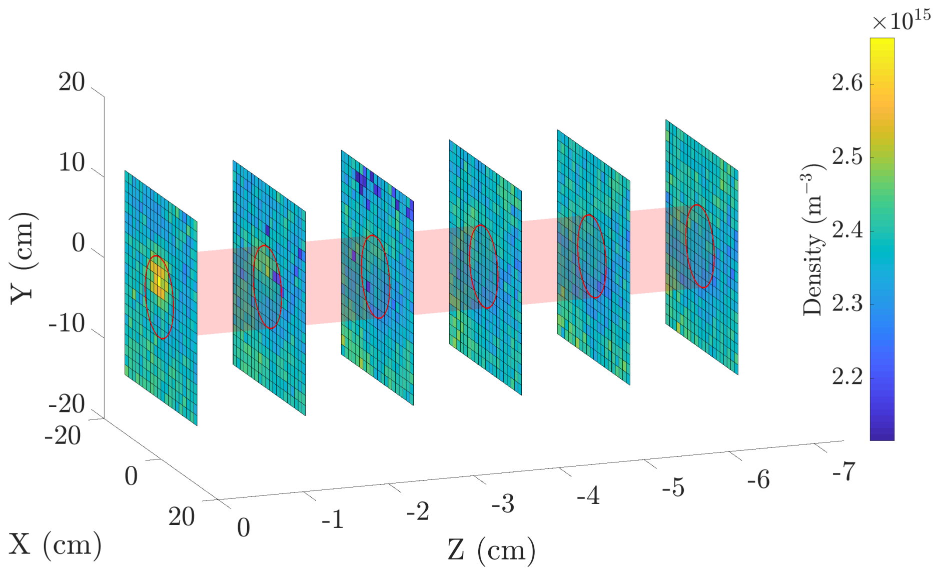

Figure 3.37: Electron Density for Experiment D

The fit quality indicated in Figure 3.35 is quite good overall. Figure 3.36 qualitatively matches experiment C, generating a wake significantly larger than the diameter of the wake-forming object and with closing distance much larger than those seen in experiments A and B. This matches the simulations results described in [60], indicating that a sparse structure can be applied to generate an enhanced wake.

A significant difference is seen in the ion density, which is increased relative to experiment C at all points on the grid. Other investigations using this same source [55] have shown that the plasma current onto an object in the streaming plasma can vary by 10s of percent over a given experiment. A vent cycle and source re-ignition took place between experiments C and D, which could have affected the source output or added contaminates to the Langmuir probe, affecting its I-V characteristics and the derived plasma parameters. Additionally, the charged sparse sphere seems to affect the local plasma environment less than the previous wake-forming object. However, this may not be true of a less-sparse structure. If the cross-sectional area of the sparse sphere were increased — such that in the limit it became a solid sphere once again — the wake would likely look similar to 3.33, given identical source output.

Finally, the same density increase is seen in Figure 3.37 as in the previous experiments. However, the enhancement is much more localized than in Figure 3.26. Indeed, the wake shape cannot be seen in Figure 3.37 as it can be in all previous experiments. This matches the conclusion made with regard to the ion density that the sparse sphere used does not have as significant an effect as a solid object charged to the same voltage.

3.2.1.7 Experiment Conclusions

The results above indicate that charging a solid or sparse object positive relative to the plasma potential will expand the wake region, matching the predictions by [48] and [60], respectively. Both the radius of the wake and its closing distance are enhanced in this circumstance. While charging the spherical conductor negative did not appear to decrease the closing distance of the wake, the deepening of the wake seen in Figure 3.30 provides interesting insight into the plasma's behavior.

The results of the experimental campaign described indicate that positively charged spares geometries can prove advantageous to electrostatic actuation simulations as plasma wakes are generated without the need for large surface areas. This will decrease the power consumption of wake expansion compared with a solid structure. The success of the wake shaping demonstration motivates a study of the power associated with electrostatic actuation with expanded wakes.

3.2.2 Power Experiments for Charging in Expanded Plasma Wakes

The experimental campaign described in this section is aimed at developing a model for the power required to charge an object in the wake of another craft applying wake shaping. The proposed technique is illustrated in Figure 3.38.

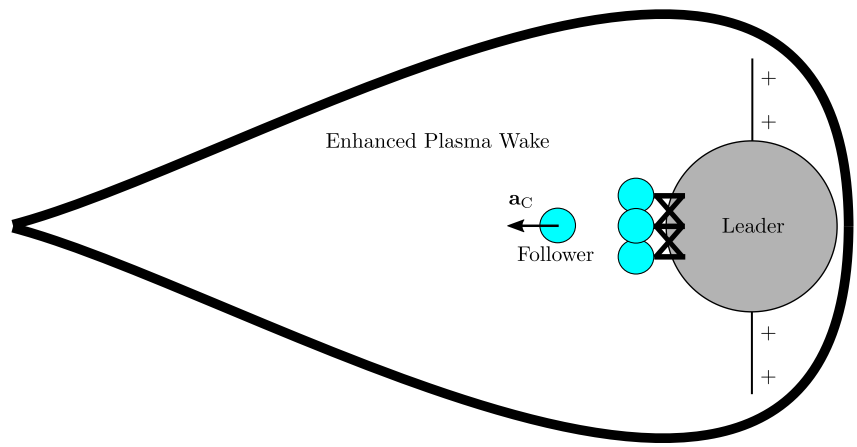

Figure 3.38: Electrostatic Actuation in an Enhanced LEO Plasma Wake

The presence of positively charged thin booms attached to the hub of the leader craft serves to expand the wake generated by the leader, providing a larger working volume for electrostatic actuation techniques. In the experiments described, three measurements were taken — the current collected by the leader as it generates an enhanced wake and the current to two probes of different sizes which are swept both spatially and in potential through the wake. The combination of these three measurements provides a basis for estimating the power required for a functioning LEO electrostatic actuation system. Additionally, the identical measurements from probes of different sizes gives scaling insight, allowing for extrapolation of results to a mission scenario.

This section provides a detailed explanation of the experiment outlined above followed by a brief discussion of the analysis methods employed to extract results from the raw data. Results are presented and the insight into the feasibility of electrostatic actuation techniques within LEO plasma wakes is discussed.

3.2.2.1 Experimental & Data Analysis Methods

Plasma wake experiments were conducted within the JUMBO chamber at the Spacecraft Charging Instrumentation and Calibration Laboratory (SCICL) at the Air Force Research Laboratory (AFRL) at Kirtland Air Force Base, NM. JUMBO is a 2 m diameter cylindrical chamber with length of roughly 3 m and is described in greater detail in [22]. The plasma source manufactured by Plasma Controls LLC used in this study and pictured in the background of Figure 3.19 uses magnetic filtering to produce a representative LEO plasma — one in which the thermal velocity of the streaming, directional ions is roughly equivalent to the velocity of a LEO spacecraft relative to ionospheric ions. Argon gas is ionized by a filament within the source to generate the ions which are then accelerated to the desired velocities by a system of charged grids. Argon is chosen because its mass is representative of the higher-concentration elements within the ionosphere and because Ar^+ is not as corrosive as elements such as O^+. This source is not differentially pumped, meaning that neutral Argon atoms are present within the flow, allowing for charge exchange between the fast-moving ions and the slow neutrals. The effect of this phenomenon is currently under investigation.

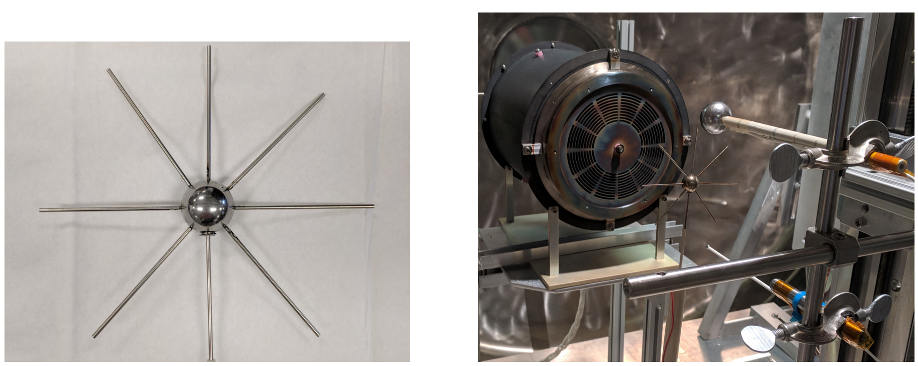

(a) Wake-Forming Representative Spacecraft

(b) Experiment Setup

Figure 3.39: Experiment Depictions

The experiments conducted apply a wake expansion methodology similar to that described in [54]. Rather than use a sparse sphere as in that work, a positively charged "spacecraft" with thin booms extending radially outward from a central hub as pictured in Figure 3.39(a) generates the enhanced wake. The presence of the thin booms is negligible when the object's positive charge is small relative to the 5 eV kinetic energy of the ions. However, as the electrostatic potential energy exceeds this value the thin booms expand the wake significantly, creating a larger region in which electrostatic actuation is feasible [54].

Two spherical probes of different sizes take current measurements at each point of a 3-dimensional grid of size 30 cm $\times$ 18 cm $\times$ 18 cm beginning $\sim$1 cm behind the spherical conductor. The probes, picture in Figure 3.39(b), are chosen to provide insight into the effects of placing differently-sized objects in the wake. Note that the large probe is significantly larger than the hub of the spacecraft. Two Keithley 2410 Source-Measure Units (SMUs) are used to collect current to the probes at each node of the 3-dimensional grid described above while sweeping through potentials ranging from -10 V to -200 V. The current on the wake-forming spacecraft held at $\Phi = 10$ V is measured constantly to provide insight into mutual effects between the probes, drift in the plasma source, and the power required to expand the wake.

Determining the local voltage surrounding a charged object in a streaming plasma is extremely difficult. Suffice to say that a power supply set to 1 V relative to chamber ground is not at 1 V relative to the local plasma. It may indeed be negative relative to the plasma. For this reason, only large voltages relative to the plasma are considered. This greatly simplifies analysis and provides all relevant information, as electrostatic actuation techniques do not provide sufficient control authority at voltages on the order of 1 V.

All data is considered in terms of power, but knowledge of the signs of voltage and current are also highly relevant to the analysis. Being that the plasma output by the source contains both positive and negative charges, changes in power sourced by a probe at a given voltage provides qualitative insight into dynamics within the plasma. For example, a negatively charged probe whose current is decreasing in time could indicate either that the number of ions coincident on the probe surface is increasing, or the number of electrons decreasing. Arriving at a solid conclusion is complicated by variations in the plasma source and other factors. However, correlation of the three measurements taken throughout the experiment provides a means to eliminate mistaken hypotheses.

It is important to recognize in interpreting results that the “ambient” wake is not being measured in this experiment. Rather, an effective wake resulting from the placement of a charged object in the wake of another is described. The presence of this charged object necessarily changes the wake’s shape and properties. The purpose of perturbing the wake in this way is not to understand its geometry as in the previous experiment, but to determine what the power requirement is to charge an object to a given potential at a given location in an expanded wake. This has clear relevance to electrostatic actuation.

It should also be noted when considering the figures below that each measurement shown is separated in time — the wake structures are not snapshots. Finally, the power values for each experiment should only be considered in a relative sense. Each individual point provides no insight into the feasibility of electrostatic actuation techniques. Only through consideration of all experiment data together can conclusions be drawn about the dependence of system power requirements on the potentials and locations of its components.

3.2.2.2 Probe Power Results

The current measurements described above provide an indication of the wake shape resulting from a charged object at a certain position. Given that the wake is ion-deficient, there is little shielding of negative potentials [27]. This means that, when the negatively charged spheres are deep in the wake, very little current is collected. However, when a sufficient negative potential approaches the edge of the wake, the streaming ions will be attracted down onto the sphere, causing a significant increase in current. This effect is seen in Figures 3.40-3.42, which show the power consumed by both probes at a given voltage and location.

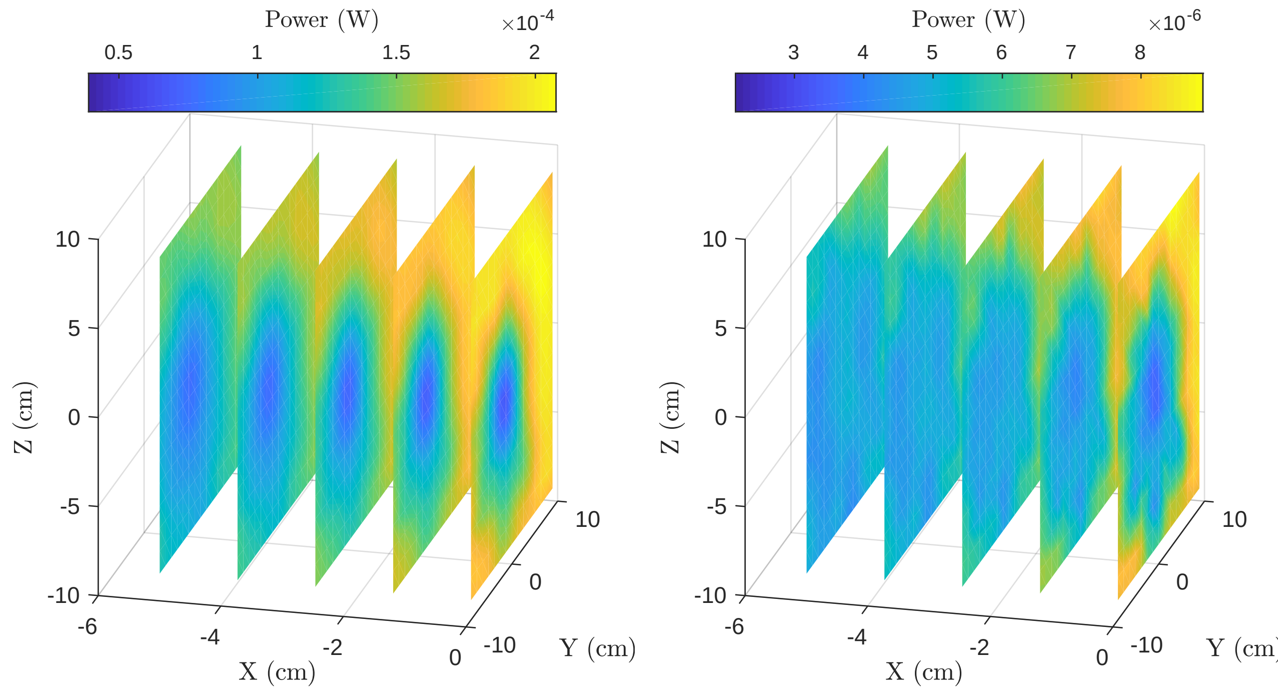

(a) Large Probe

(b) Small Probe

Figure 3.40: Power Required to Hold Probes at Φ = -10 V

An interesting difference in Figures 3.40(a) and 3.40(b) is the sharpness of the features at the X=0 cm plane. Recall that the spacecraft is held at 10 V. Ion trajectories are therefore deflected away and, in the wake, will not be collected by probes charged negatively to this same potential. This results in the structure in Figure 3.40(b), which clearly matches the shape of the spacecraft shown in Figure 3.39(a). Notably, the wake region directly behind the thin booms on the spacecraft are significantly larger than their diameters. This matches the conclusion from Reference [54] that thin, lightweight objects can be charged to significantly expand wakes. Indeed, the ambient wake behind such an object would certainly be even larger, but is compressed by the fact that the probes are charged negatively.

The structure shown so clearly in Figure 3.40(b) appears significantly washed out in Figure 3.40(a). This is due to the larger collection area of the large probe and persists in Figures 3.41(a) and 3.42(a). Importantly, the diameter of the large probe is greater than the distance steps on the 3-dimensional grid described in previous sections. This circumstance provides insight into the feasibility of manipulating large craft within the wake electrostatically. It is clear from comparison of Figures 3.40(b) and 3.40(a) that a larger object has a smaller working area for electrostatic actuation techniques.

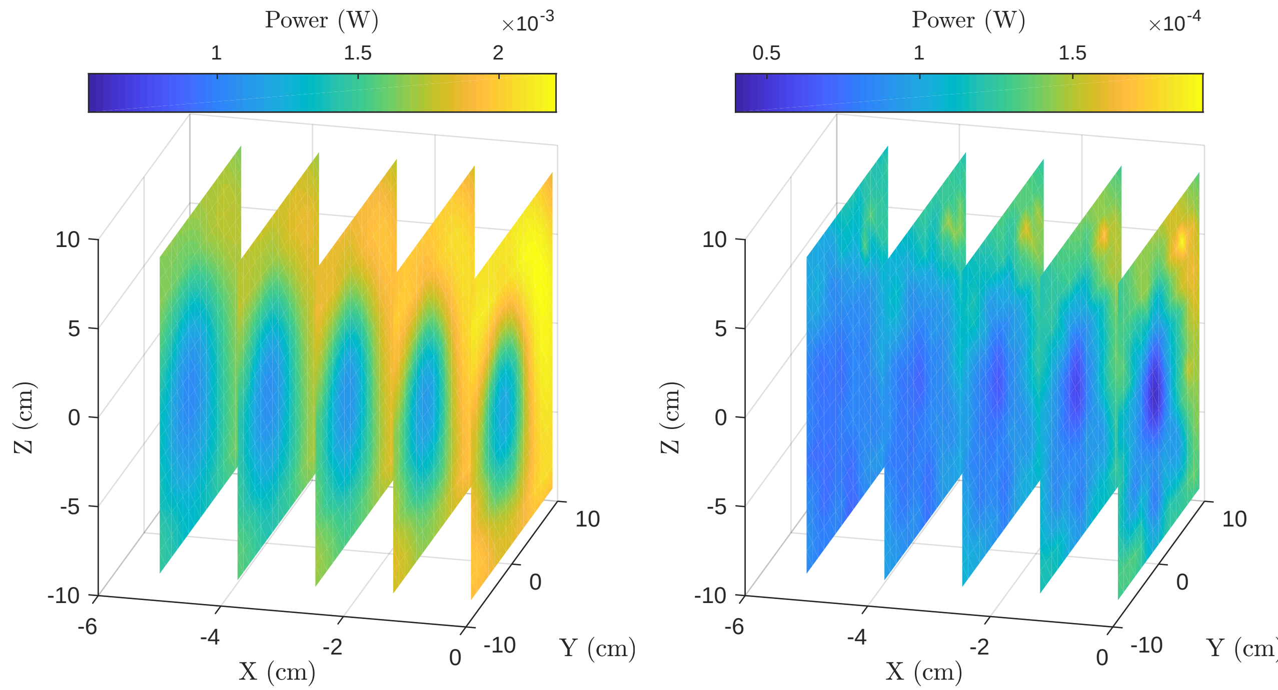

(a) Large Probe

(b) Small Probe

Figure 3.41: Power Required to Hold Probes at Φ = -50 V

The spacecraft structure shown in Figure 3.40(b) persists in Figure 3.41(b), though the difference in power sourced by the probe within the wake is far more comparable to that in ambient in this latter experiment. This results from an increase in the probe voltage while holding the spacecraft voltage fixed at 10 V. This effect is even more pronounced in Figure 3.41(a). However, this and Figure 3.40(a) have an interesting quality not as clearly shown by the small probe measurements — an increase in the wake diameter for increasing values of X. This is also seen in the results discussed in Reference [54], but was assumed the result of excessive potentials on the wake-forming craft disrupting the entirety of the limited volume of plasma output by the source. The persistence of this feature in the presence of a much smaller spacecraft potential indicates that the enhanced wake does not close in the same way as the ambient.

Consider a lone craft in LEO. If uncharged, ions are initially deflected via interactions with the sheath and surface in the very near vicinity of the craft. As discussed previously, this results in the wake behind the craft which exhibits a negative space-charge. The trajectories of ions deflected only slightly around the craft by the initial interaction are affected only by this space-charge, which pulls them toward the wake axis resulting in wake closure a short distance behind the craft. However, a craft at 10 V interacts differently. Firstly, the initial trajectory deviation is much greater, as ions enter a potential gradient significantly larger than their kinetic energy relative to the craft. After they pass the craft, the decreased shielding in the wake mentioned above allows the electric field of the craft to continue repelling them. This repulsion will continue until the combination of the reduced shielding and natural $1/r^2$ falloff of the field is less than the space-charge in the wake.

In the experiments described in Figures 3.40-3.42, the presence of a negatively charged objects affects the closing distance, but this value is highly dependent on the location of the object. Placing it on the wake axis clearly maximizes the size of the wake, but the optimal position of this object on this line will be a function of both the spacecraft and probe potentials. Applying this knowledge of position-potential coupling would allow for minimal power usage for a given electrostatic actuation technique.

Figure 3.42 bears similar hallmarks to the previous experiments, including the tendency for in- and out-of-wake power differences to decrease with probe voltage. While the effective wake — such as it is — continues to expand as the probes move away from the spacecraft, the power savings are negligible. This result combined with the preceding discussion indicates that the magnitude of the spacecraft potential must be comparable or greater than that of the probes in order to reap any benefit from charging within the wake.

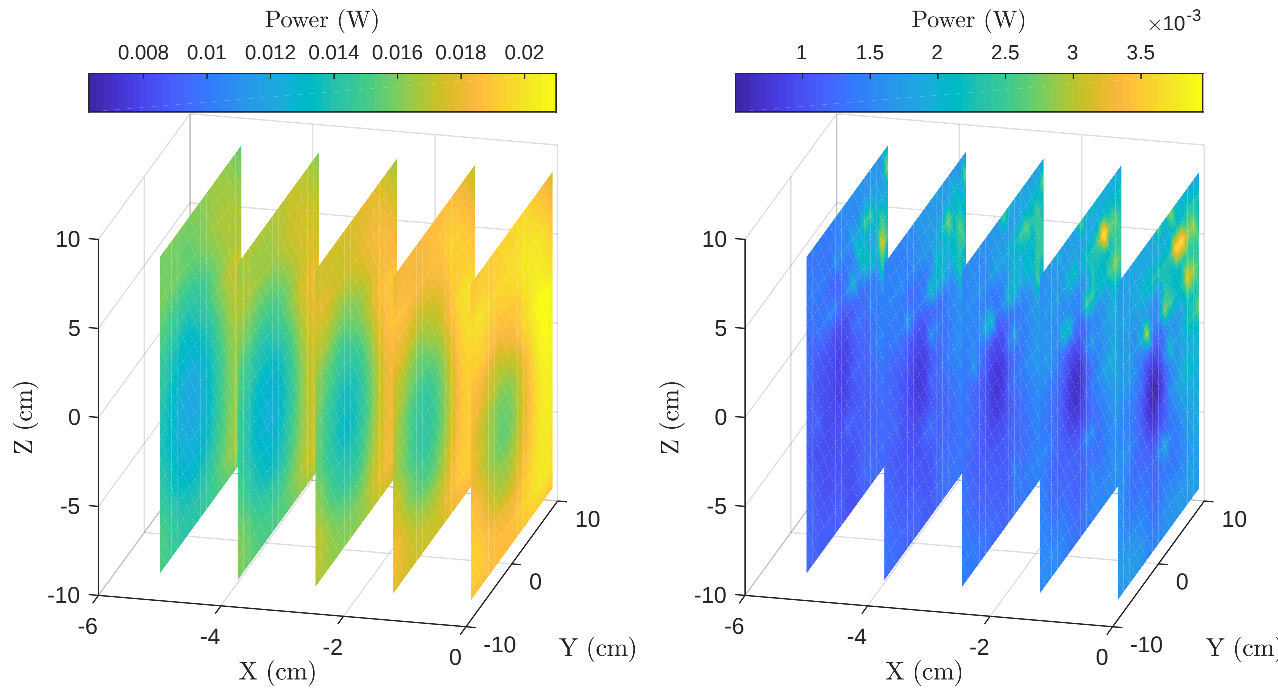

(a) Large Probe (b) Small Probe

Figure 3.42: Power Required to Hold Probes at Φ = -200 V

3.2.2.3 Spacecraft Power Results

A sample of the power sourced by the spacecraft is shown in Figure 3.43. Three separate timescales are shown, each with the same starting time. Each of Figures 3.43(a)-3.43(c) shows different behaviors. The decrease in power on the timescale of hours indicates drift in the plasma source — a common occurrence of such systems. For a positively charged probe, this indicates either a decrease in electrons collected or an increase in ions collected. It can be inferred from this information that the energy and/or density of one or both of these species is varying in time. Inspection of Figure 3.40(b) provides an additional clue. The scanning method employed to navigate the 3-dimensional grid at which measurements are made is such that measurements on the Z=10 cm plane are taken days before those on the Z=-10 cm plane. The lower power values on the -Z half of Figure 3.40(b) must be considered alongside the plasma parameters of the source.

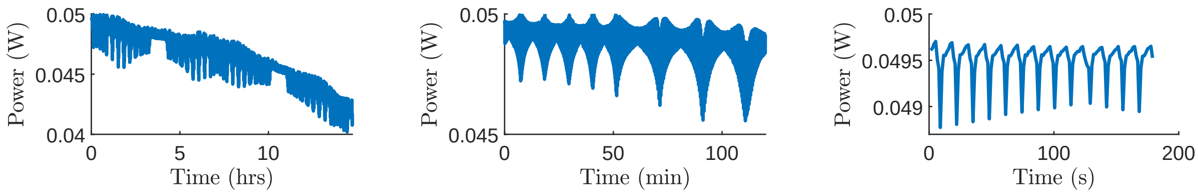

(a) Hours (b) Minutes (c) Seconds

Figure 3.43: Spacecraft Power Signal Structure at Different Timescales

In simulating LEO conditions, the ion and electron energies are necessarily different. Calibration values for the plasma source indicate that, for the parameters used in this experiment, the electron temperature distribution is centered at about 1 eV, while the ions are streaming directionally with a temperature distribution centered at roughly 5 eV. Assuming these distributions are relatively narrow, a probe at -10 V in this plasma should repel almost all electrons while collecting most of the ions. On the other hand, the spacecraft charged to +10V would collect some number of ions (from the high-energy tail of the distribution), while collecting almost all electrons. This information combined with time-correlated decreases in power to both the positively charged spacecraft and negatively charged probe indicate a general decreases in energy/density of the plasma output by the source.

Different behavior is seen in the spacecraft power curve on the order of minutes as shown in Figure 3.43(b). This can be understood by considering the current as the time derivative of charge. For this discussion, the current from the plasma is neglected, as it is not expected to vary significantly over the timescale of minutes and is therefore considered a baseline value upon which other effects are superimposed. Consider the current as the time derivative of the well-known voltage to charge relationship.

$$\boldsymbol{I} = \frac{\mathrm{d}}{\mathrm{d}t}(\boldsymbol{Q}) = \frac{\mathrm{d}}{\mathrm{d}t}(C\boldsymbol{V}) \tag{3.7}$$

Here, C is the capacitance matrix which modifies charge on an object given nearby charged objects.

Expanding Eq. (3.7) according to the experiment configuration described above yields

$$\begin{pmatrix} I_L \\ I_S \\ I_{SC} \end{pmatrix} = \frac{\mathrm{d}}{\mathrm{d}t}\begin{pmatrix} Q_L \\ Q_S \\ Q_{SC} \end{pmatrix} = \frac{\mathrm{d}}{\mathrm{d}t}\left\{\begin{bmatrix} C_L & C_{L,S} & C_{L,SC} \\ C_{S,L} & C_S & C_{S,SC} \\ C_{SC,L} & C_{SC,S} & C_{SC} \end{bmatrix}\begin{pmatrix} V_L \\ V_S \\ V_{SC} \end{pmatrix}\right\} \tag{3.8}$$

To understand the structure in Figure 3.43(b), only the bottom row is necessary.

$$I_{SC} = \frac{\mathrm{d}}{\mathrm{d}t}(C_{SC,L}V_L + C_{SC,S}V_S + C_{SC}V_SC) \tag{3.9}$$

Given that the spacecraft is held at a constant 10 V potential and its shape — which determines its self capacitance C_{SC} — does not change, the final expression for the power on the spacecraft resulting from the probes is

$$P_{SC} = I_{SC}V_{SC} = (\dot{C}_{SC,L}V_L + C_{SC,L}\dot{V}_L + \dot{C}_{SC,S}V_S + C_{SC,S}\dot{V}_S)V_{SC} \tag{3.10}$$

From the experiment setup, it is known that the mutual capacitance terms — which are a function of separation distance between the probes and the spacecraft — change on timescales of minutes, while the voltages change must faster. Therefore, the structure seen in Figure 3.43(b) results from the motion of the probes relative to the spacecraft. The voltage derivative terms in Eq. (3.10) generate the structure seen in Figure 3.43(c).

Finally, consider the magnitude of power used by the spacecraft relative to the probes. The total area of the spacecraft is comparable to that of the large probe, yet the former uses far more power even when the latter's voltage is orders of magnitude larger. This indicates that wake expansion techniques are more expensive than implementing the electrostatic tractor itself. However, the sheer difference in power consumption motivates the use of such techniques. Even when the probe is charged to extremely large negative voltages, the local plasma environment is significantly less dense than the ambient experienced by the wake-forming spacecraft. The power required by electrostatic actuation increases strongly with plasma density, as increases in both the current to the object and the shielding of electrostatic forces and torques motivate larger sourced currents and voltages, respectively. Therefore, application of wake expansion techniques could result in a decrease in power required to electrostatically actuate a follower craft that is large relative to the size of the wake in which it flies.

3.2.2.4 Probe Scaling Results

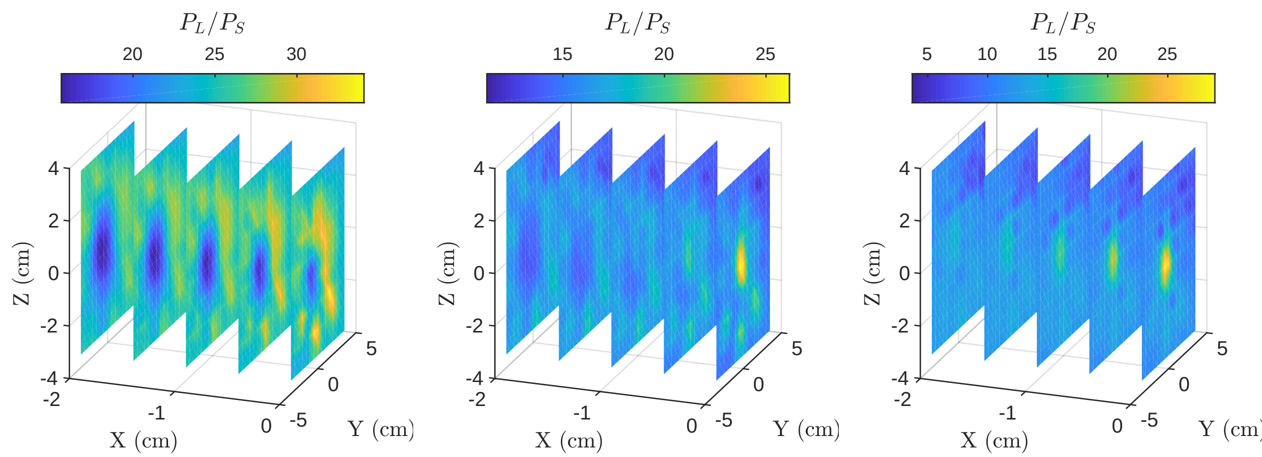

(a) Φ = -10 V

(b) Φ = -50 V

(c) Φ = -200 V

Figure 3.44: Ratio of Large Probe Power to Small Probe Power at Various Potentials

Comparison between the power on the large and small probes provides an indication of how the power scales with increasing craft size. Figure 3.44 shows the ratio of power on the large probe to that of the small probe for each voltage measurement. As expected, the large probe always requires more power than the small probe. However, the ratio between these two is a function of both voltage and position. Figure 3.44(a) has a great deal of structure. At the center, the ratio is relatively small because the the spacecraft diverts most ions away from the probes. However, near the thin booms, the ratio increases significantly. This is because the small probe is completely in the wake of the booms, while the large probe integrates over an area that is only partially within the wake.

Figures 3.44(b) supports the previous conclusion that the size, voltage, and location of a probe determines the wake closure distance. Near the point $[0,0,0]^T$ cm, the large probe collects a great deal more current than the small probe. However, as the probes are moved backward along the Y=0 cm, Z=0 cm line, the ratio decreases and, eventually, becomes lower than the ambient. A similar decrease is seen in Figure 3.44(c), though it never drops near the ambient value. Additionally, very little structure is seen in this figure besides at the very center. This supports the conclusion that a probe voltage so much larger than that of the spacecraft minimizes the power savings gained from charging in the wake.

The two-point probe measurements allow for linear extrapolation of the power required to charge a craft of given size in the wake according to Eq (3.12).

$$P_{\text{object}} = \frac{\mathrm{dP}}{\mathrm{dA}} A_{\text{object}} \tag{3.11}$$

$$\frac{\mathrm{dP}}{\mathrm{dA}} \approx \frac{\Delta \mathrm{P}}{\Delta \mathrm{A}} = \frac{\mathrm{P}_L - \mathrm{P}_S}{\mathrm{A}_L - \mathrm{A}_S} \tag{3.12}$$

The transformation $\Delta P/\Delta A$ is plotted throughout the volume of the given experiment in Figure 3.45. According to these results, charging a 10 cm diameter spherical probe in the wake to -50 V — a feasible parameter set for an application of electrostatic actuation — would require an estimated 15 mW of power. Maneuvering much larger objects would require much more power, because both the current collecting area and object inertia increase. Applying this same concept to a larger craft would require more force and therefore larger voltages. However, the experiment configuration is such that electrostatic actuation at voltages significantly larger than that of the wake-forming spacecraft are not power efficient, as discussed previously. The data collected here indicates that a 1 m diameter craft at -200 V would require 63 W of power. Based on the Nascap-2k simulations presented previously, this indicates that wake collapse has occurred. In optimizing for heavier objects, a larger spacecraft voltage would be applied to expand the wake further, potentially leading to an overall power savings relative to the 63 W requirement estimated from the data.

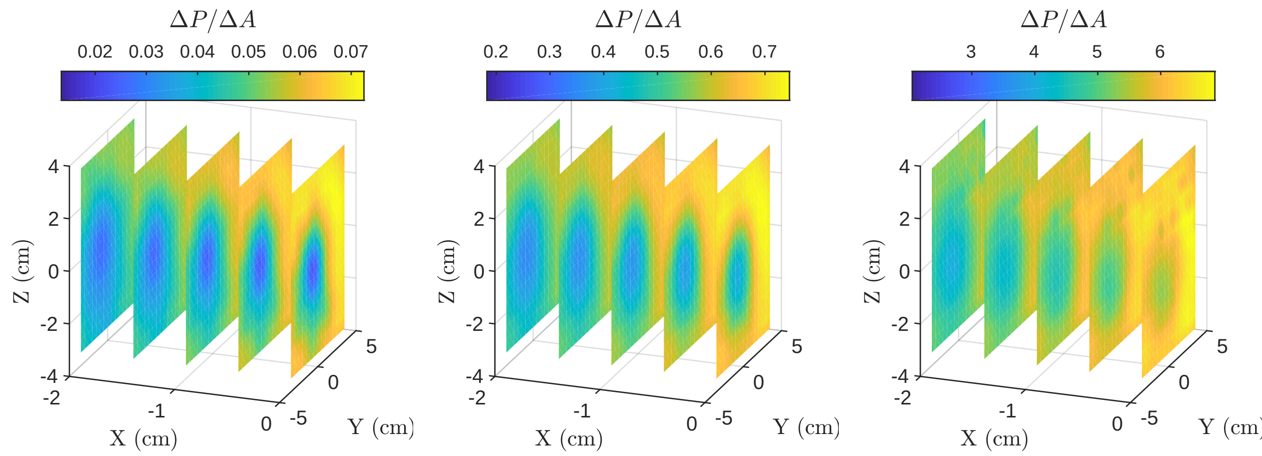

(a) Φ = -10 V (b) Φ = -50 V (c) Φ = -200 V

Figure 3.45: Area to Power Transformation

3.2.2.5 Experiment Conclusions

Experimental results indicate that, for certain configurations, significant power savings can be achieved by charging in the wake. However, as potentials increase relative to that of the wake-forming craft, the savings decrease. This effect is less true for small objects in the wake than larger ones and depends on location. Results indicate that manipulating a small daughter craft in the wake of a mother craft using electrostatic actuation — as described in Reference [53] — could be quite power-efficient. Additionally, maneuvering lighter craft requires less control authority, so lesser voltages could be used.

The dataset presented provides a great deal of insight into the application of electrostatic actuation within LEO plasma wakes, but can also be used as a physical model using scaling insight and interpolation schemes. Future work will use this and similar datasets in control simulations for technological insight. Results are qualitatively consistent with the Nascap-2k simulations presented previously in that power is reduced in the wake. Direct comparison is extremely difficult due to differences in sizes, geometries, and potentials.

3.3 Results & Summary of Goal 3

The development of a plasma wake models enables analysis of the challenges of LEO electrostatic actuation techniques. A great amount of insight was gained from the investigations described throughout this chapter. Nascap-2k simulations provided a baseline for LEO plasma wakes behind uncharged and charged spacecraft in orbit, indicating that charged wake dynamics are far more complex than ambient wake dynamics. This motivated a series of parametric studies across leader and follower bias potential signs and magnitudes, sizes, and geometries. One clear trend was that negative potentials — though more likely to lead to wake collapse — cost significantly less power than positive potentials. Another general trend identified was that for the ~ 1 kV potential needed in ideal circumstances to settle a cubesat in LEO, a leader craft diameter of at least ~ 3 m was needed to not collapse the wake. This exceeds the size of most LEO spacecraft, with the notable exception of the ISS, motivating an investigation of techniques for expanding and shaping LEO plasma wakes.

Two experimental wake shaping investigations described provide insight into the feasibility of using lightweight, thin structures to generate large wakes for relatively small craft. The first experiment considered wake formation from a solid object charged to various potentials both positive and negative. The greatest wake expansion effect was seen in the experiment with large positive object voltages, as expected. Next, the same experiment is run for a sparse object similar in size and geometry charged to the same positive voltage. Wake expansion is still seen, but the sparse nature of the shape allows plasma to flow though, leading to less significant wake expansion and higher ion content in the wake. This effect could be mitigated by increasing the density of the sparse geometry.

The final experiment discussed considers the power required to conduct electrostatic actuation while actively wake shaping. A variety of analyses were run on the data indicating the power in the expanded wake is indeed lower than in ambient, but rough comparison with Nascap-2k simulations indicated wake collapse had occurred for relatively low potentials. This indicates that a more dense geometry than that shown in Figure 3.39 must be used.

While the simulation and experiment results are difficult to compare due to the complex physics at play, all investigations conducted agree with the literature on one key fact —- if the wake is large enough, very little power is expended when charging the follower craft negatively. While this general trend does not allow for explicit calculation of the necessary formation geometry and parameters for electrostatic actuation, it certainly indicates that for certain circumstances — a cubesat following the ISS, for example — the technique is certainly feasible and likely to be extremely efficient.

Chapter 4

Space Simulation Facility Development

As indicated by the many simulations and experiments described in the previous chapter, a primary obstacle in applying electrostatic actuation in LEO is the behavior of the plasma wake. The concern is that charging an object in the wake to positive or excessively negative voltages costs large amounts of power not feasible for modern spacecraft power systems to maintain. Simulations run in Nascap-2k illustrate the relationship between the maximum voltage that can be sourced and the wake-forming craft's diameter to avoid wake collapse, indicating that electrostatic actuation is not feasible for large voltages and small leader craft. However, experiments motivated by the results shown in reference [60] and described in the previous chapter demonstrate the concept of wake shaping. The technique allows for the ambient wake to be expanded by use of positive potentials and/or sparse conductors. The benefit of using positively charged, sparse conductors is that the wake can be expanded without substantially increasing mass- or area-dependent perturbations.

The primary challenge faced when investigating wake shaping is accurately simulating spacecraft-ionosphere interactions terrestrially. Spacecraft in LEO experience an isotropic electron flux, but a directional, collimated ion flux. This latter situation arises from the supersonic nature of LEO spacecraft with respect to the ionosphere. Because of the highly-rarified nature of the LEO environment, the primary means of wake closure comes from electrostatic forces arising from the negative space charge build-up in the wake. Achieving a representative wake closure distance is crucial to experimental investigation of charged wake dynamics, as the power associated with charging is highly dependent on the distance to the wake edge whose position is determined by the wake closure. As described previously, wake experiments conducted on the ground place a stationary object in a flowing ion plasma moving at LEO orbital speeds. Assuming the plasma densities and ion flow velocity match those in LEO — or the scaling laws in reference [19] are appropriately applied — the Coulomb attraction between the ions on the wake edge and the negative space charge in the wake will result in LEO-like wake closure.

While a great deal of insight into wake shaping techniques has been gained from the experimental campaigns described previously, the zero-voltage control experiments do not conform to the NASCAP-2k simulation results or the literature. This is primarily a consequence of the plasma source, which is a flood source applying magnetic filter to achieve roughly LEO-like kinetic energies and densities. The two concerns with this source is that it is not collimated, and the electrons are not isotropic. These effects compound each other in preventing wake closure from occurring on the expected spatial scales.

This chapter seeks to develop an improved simulation facility and experimental design concept for investigation of general charged wake dynamics and wake shaping techniques. As indicated by the discussion above, this task ultimately comes down to producing a collimated ion flux such that a generated plasma wake will close on experimental spatial scales. It is clearly stated here that generation of an exactly LEO-like plasma is not the objective. More weight is put upon the ability to feasibly explore charged wake dynamics, as this provides insight into electrostatic actuation techniques.

The Electrostatic Charging Laboratory for Interactions of Plasma and Spacecraft (ECLIPS) is being designed to investigate topics critical to the development of electrostatic actuation. These include potential sensing techniques for craft on orbit[9, 99], High Area to Mass Ratio (HAMR) objects charged dynamics [57], and plasma wake dynamics. This last item is the focus of this chapter. A holistic discussion of the relevant LEO-environment simulation techniques is included here, as the environment as a whole affects the plasma's behavior. The primary contribution is the development of a novel LEO plasma simulation method that produces wake closure which leverages electrostatic lens design as well as space-charge induced spreading of the beam.

4.1 Motivation for Experimental Study of Wakes

Chapter 1 discusses a variety of experimental, numerical, and analytic studies of LEO plasma wakes. Notably lacking in the literature is a means of rapidly investigating wake behavior under changing conditions. Plasma simulation software like Nascap-2k provide a great deal of information, but takes minutes to converge on solutions and represent the wake behavior for only a single formation configuration (i.e. they provide information at discrete points in time). Electrostatic actuation simulations indicate significant deviations in object potentials and positions as the follower craft is controlled behind the leader, meaning that wake behavior is likely to change significantly in time. Numerical simulations can provide snapshots of wake behavior, but predicting the critical points — for example, when wake collapse is about to happen — is difficult as the plasma behaves in complex, non-intuitive ways. Experimental investigations serve to supplements these numerical simulations by providing a means of investigating wake behavior continuously in time.

An additional motivation for the application of experimental methods comes from the wake shaping experiments described in Chapter 3. These experiments considered positive charging of thin, sparse structures to create an enhanced wake. Nascap-2k and similar packages apply Finite Element Method (FEM) techniques to simulate plasma behaviors. A general rule for the spatial (Δx) and temporal (Δt) discretization conditions for stability of these techniques are included below as well as their values for a LEO simulation.

$$\Delta x \lesssim \lambda_{\mathrm{D}} \approx 1 \text{ cm} \quad , \quad \Delta t \lesssim {}^{1}\!/\!_{\omega_{\mathrm{pe}}} \approx 0.1\ \mu\text{s} \tag{4.1}$$

The time step indicated by this condition is several orders of magnitude lower than required for any LEO orbit simulation, providing an additional motivation for the development of empirical models over those derived from simulation. Considering the spatial constraint, most spacecraft are much larger than 1 cm, meaning that the conditions are sufficient for most applications. However, the wake shaping experiments presented make use of structures on the order of 1 mm that are charged to significant positive voltages. Therefore, much finer meshes must be applied about these structures. The resulting wake expansion will also necessitate a larger overall simulation volume, adding the need for yet more finite elements. Constructing these complex, high-point-density meshes requires significant time and effort, and must be redone for every change in geometry. Therefore, experimental techniques — to which sparse object pose no unique obstacle — are preferred when investigating wake shaping methods.

4.2 ECLIPS Chamber Overview

The primary contribution of this aspect of the overall research is the design of a LEO-like plasma simulation technique which enables rapid investigation of wakes resulting from arbitrary geometries and applied potentials. The design described in this chapter is suitable for implemented on the ECLIPS chamber, which is therefore used as a frame for this discussion. However, theoretical background is provided such that future researchers can apply the design considerations to other facilities.

Figure 4.1: ECLIPS Space Simulation Chamber

The ECLIPS facility pictured in Figure 4.1 is specifically designed to conduct experiments relevant to electrostatic actuation. The simulation test-bed is loosely based on the Jumbo chamber [22] at the Spacecraft Charging Instrumentation and Calibration Laboratory (SCICL) at the Air Force Research Laboratory (AFRL), though applies different methods for simulating the LEO environment. The development of ECLIPS is being assisted by plasma experiment experts at SCICL and the Laboratory for Atmospheric and Space Physics (LASP) also operated out of CU Boulder.

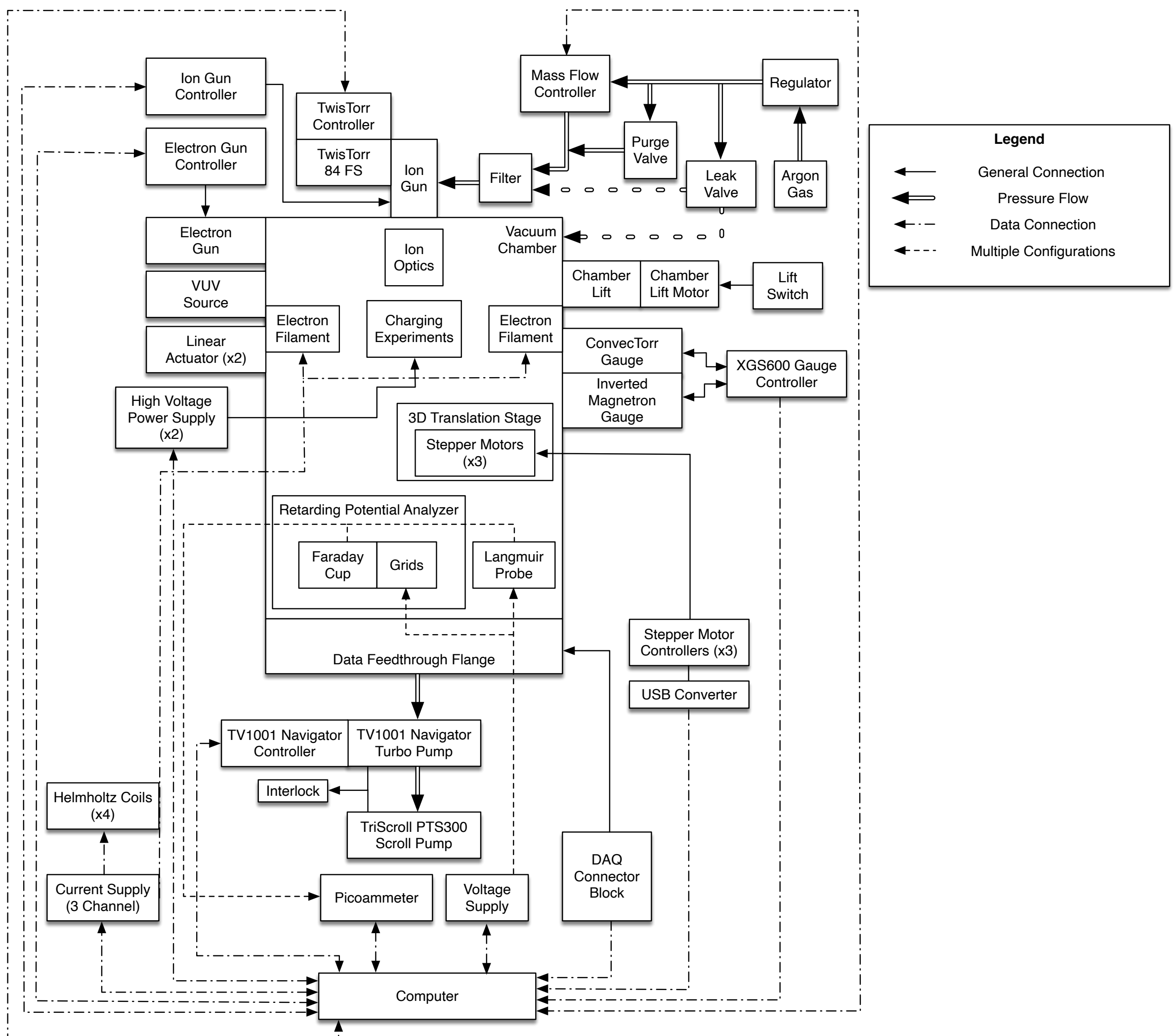

Figure 4.2: ECLIPS Block Diagram

The ECLIPS chamber block diagram is shown in Figure 4.2. A turbomolecular pump backed by a scroll pump enables a minimum pressure of roughly 10^{-6} Torr (10^{-9} atm). The two elements of the plasma are sourced using different techniques. A design of the system is shown in Figure 4.3.

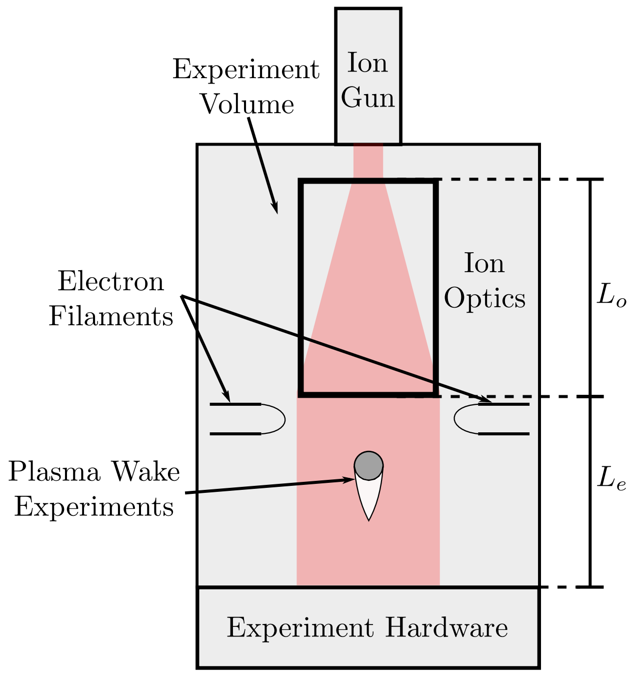

Figure 4.3: Block diagram of proposed LEO plasma simulation technique suitable for implementation in the ECLIPS facility

A low-energy, high-density collimated ion beam is fired down the axis of a cylindrically symmetric plasma chamber. Before spacecharge spreading effects can compromise the collimation, the beam enters ion optics designed to output a collimated ion flux. Electron filaments are placed at the exit of the optics to create a representative LEO environment. The length of the optics L_o and the desired experiment L_e must be considered in comparison to the available experimental volume. For the ECLIPS chamber, the available experimental volume — to remain far from nearby hardware — is a cylinder of height $L_o + L_e$ =∼60 cm and diameter ∼30 cm. These dimensions apply constraints onto the ion optics design and feasible wake-forming object radius, as wakes in LEO typically close roughly 1 craft radius down their axis.

A source-measure unit will be used as the detector on a variety of different plasma measurement devices. The experiments in Chapter 3 applied spherical probes, though a variety of different measurement apparatuses including Retarding Potential Analyzers (RPA) and emissive probes will be applied to analyze the energy and density of the expanded beam and probe wake behavior. The general design of these probes and devices is not discussed here, as a great amount of literature informing their design and construction exists.

4.3 Vacuum Environment Design

A key feature of plasma wakes — and one especially relevant to the development of electrostatic actuation techniques — is their ion-void nature. This phenomenon results from the supersonic nature of spacecraft relative to the ionosphere and is simulated in terrestrial chambers like ECLIPS by the reference frame switch in which a stationary wake-forming craft is enveloped in a flow of collimated ions of the proper LEO orbital velocity. A common challenge in such experiments is preventing the generation of a low-energy ion population via charge exchange between beam ions and neutrals present in the chamber.[92] The baseline reaction assumed is $\mathrm{Ar} + \mathrm{Ar}^+ \rightarrow \mathrm{Ar}^+ + \mathrm{Ar}$, as reference [95] provides the charge exchange cross section ($\sigma_{cc} = 3.19{\times}10^{-19}$ m^2). While other reactions — $\mathrm{N}_2 + \mathrm{Ar}^+ \rightarrow \mathrm{N}_2^+ + \mathrm{Ar}$, for example — are likely more common, charge exchange studies at such low energies are rare and data for interactions between Ar^+ and atmospheric constituents could not be found. Given the above-cited cross section for the Ar-Ar^+ reaction, the mean free path for charge exchange (λ_{cc}) is calculated

$$\lambda_{cc} = (\sigma_{cc} n)^{-1} \tag{4.2}$$

where n is the particle number density. To mitigate the effect of charge exchange, the mean free path must be much larger than the experiment dimensions. Baseline analyses indicate ECLIPS plasma experiment sizes on the order of 10 cm, so a conservative assumption on the charge exchange mean free path of 100 m is made (i.e. no particle will travel more than 0.1% of λ_{cc}). Inverting Eq. (4.2), the associated density is roughly 10^{16} m^{-3}.

The neutrals in the chamber are at room temperature (0.025 eV), as they are remnants of the atmosphere mostly pumped out by an imperfect pumping system. The volume of ECLIPS is 0.287 m^3. Given this information, the pressure required to achieve a 100 m charge exchange mean free path is calculated assuming an ideal gas. Below, T is the temperature of the neutrals, V is the chamber volume, and p is the chamber pressure.

$$p = \frac{nk_{\mathrm{B}}T}{V} \approx 10^{-5} \text{ Torr} \tag{4.3}$$

The ECLIPS vacuum system is fully implemented and achieves a base pressure of roughly 10^{-6} Torr. Given the conservative bound of a 100 m mean free path, it is assumed that charge exchange interactions will rarely occur, meaning that the ions in the chamber will have a uni-modal energy distribution as in LEO. The equations and discussion presented above provide a concrete means of calculating a recommended base pressure for other facilities.

4.4 Plasma Environment Design

The spacecraft-plasma interactions in LEO are difficult to simulate because of the vastly different behavior of ions and electrons described in Chapter 1. Translating an object at the LEO orbital velocity of $\sim$ 7 km/s is clearly impractical for terrestrial experiments. Instead, the spacecraft reference frame is simulated so that the ions stream directionally past an object at this speed, while the electron flux is isotropic. The ECLIPS facility will use a high-current, low-energy ion gun (model 1402 from Non Sequitur Technologies) to simulate the streaming ions. The narrow beam put out by this device will be widened with an electrostatic telescope designed specifically such that an ion front simulating LEO envelops the wake-forming craft.

4.4.1 Electron Plasma Generation

The generation of the electron plasma is simpler in implementation. Filaments placed around the interior of the vacuum chamber will, by thermionic emission, release electrons. The resulting current density is calculated according to reference [46] given a material-dependent constant A_G, the material temperature T, the work function W, and the change in the work function ΔW resulting from an applied bias on the filament which generates an electric field E at the material surface.

$$J = A_G T^2 e^{-\frac{(W-\Delta W)}{k_B T_e}} \ , \ \Delta W = \sqrt{\frac{e^3 E}{4\pi\epsilon_0}} \tag{4.4}$$

The temperature, bias, and number of filaments will be chosen such that a LEO-like electron density ($\sim 10^{12}$ m^{-3}) is sourced, resulting in a neutral plasma as in LEO given the discussion above. These electrons will be accelerated to the proper, LEO energy (∼0.1 eV) by applying the appropriate potentials around the sources. The scaling laws presented by reference [19] should be applied to attempt to correct for deviation from the electron density and energy that can practically be sourced with the technique described.

4.4.2 Ion Plasma Generation

4.4.2.1 Experiment Spatial Constraints

With the electron plasma source mechanism described, the design of a multi-element ion source remains. Given a collimated ion beam with constant current I and energy E, the effective number density n of the ion front can be calculated.

$$n = \frac{I}{eAv} = \frac{I}{e\pi r^2}\sqrt{\frac{m_i}{2E}} \tag{4.5}$$

Above, e is the electron charge, A is the area of the beam and r its radius after passing through the optics, v is the ion front velocity, and m_i is the ion mass. By varying the radius of the beam, the effective density can be modulated. This is one novel aspect of this project. A search of the existing literature indicates this is a new method for modulating effective density which can be used to simulate density variations as the simulated craft changes altitude or transitions between the day and night sides of the ionosphere.

One constraint on terrestrial experiments is the size of the simulation facility. The ECLIPS chamber is a cylinder of radius ~ 0.3 m and height ~ 1 m, meaning that only small mock spacecraft can be used. Rather than rely on generating an exactly LEO-like environment, the plasma scaling laws introduced in reference [19] are applied such that spacecraft-plasma interactions of much larger craft can be investigated. In this work, five non-dimensional scaling parameters are derived via Buckingham Pi analysis which indicate that larger-scale plasma phenomena can be investigated by applying larger plasma densities, leader voltages, and/or plasma temperatures.

Given the above discussion of ion beam expansion, large-scale phenomena can be investigated by widening the beam such that the experiment plasma density (n) is much larger than ambient LEO (n_{LEO}). Reference [19] indicates the following scaling law in this case.

$$R_{\mathrm{sim}} = \sqrt{\frac{n}{n_{\mathrm{LEO}}}} R_0 \tag{4.6}$$

Here, R_0 is the true radius of the object in the plasma while R_{sim} is the scaled radius. The use of such scaling laws to investigate a wide range of LEO conditions given a much different parameter space is another novel aspect of this project. Reference [19] was only published within the last two years, and applies specifically to LEO plasma wakes.

A minimum constraint on the radius r of the ion beam simulating the ionosphere is that it must be larger than the true object radius R_0 such that the object is completely enveloped in the ion beam. However an additional requirement on this radius exists: in order to accurately simulate the LEO environment, any potential within the plasma must fall off before the edge of the beam else the ion front will diverge and result in a stream of particles whose dynamics are dominated by the craft potential rather than its supersonic velocity. If large potentials (compared to the relative kinetic energy) exist near the beam edge, the particle trajectories at this point will be affected, compromising the energy and density of the plasma as a whole. Therefore the following requirement is placed on the beam radius.

$$r > R_0 + N\lambda_{\mathrm{D}} \tag{4.7}$$

Above, N is some positive number and λ_{D} is the Debye length in the plasma, which indicates the spatial scale over which potentials in the plasma decay. Generally speaking, large N is desired for wake experiments as it means even large potentials will fall off before the beam edge. Note from the equation below that the Debye length is inversely proportional to $\sqrt{n}$ such that potentials die off faster in a more-dense plasma. Below, ϵ_0 is the electrical permittivity of vacuum, k_{B} is the Boltzmann constant, and T_e is the electron temperature.

$$\lambda_{\mathrm{D}} = \sqrt{\frac{\epsilon_0 k_{\mathrm{B}} T_e}{e^2 n}} \tag{4.8}$$

If the condition in Eq. (4.7) is met for N, it can be expected that the beam will remain coherent. Therefore, wake behaviors and properties can be investigated provided the experiment parameters applied results in a set of dimensionless parameters which also match the LEO environment according to reference [19].

4.4.2.2 Ideal Thin Lens Telescope Comparison to Ion Optics Simulations

Given the limits and conditions defined on the expanded beam, notional ion optics designs can be generated and simulated to achieve the desired expansion. References that provide analytic and numerical insight into lens design are applied alongside ion optics simulation software SIMION.[23] The general design for the ion source system outlined above indicates that the beam should be collimated before and after the ion optics, motivating the design of an electrostatic telescope to expand the beam.

Consider the electrostatic accel-decel ion telescope pictured in Figure 4.4 described by reference [49].

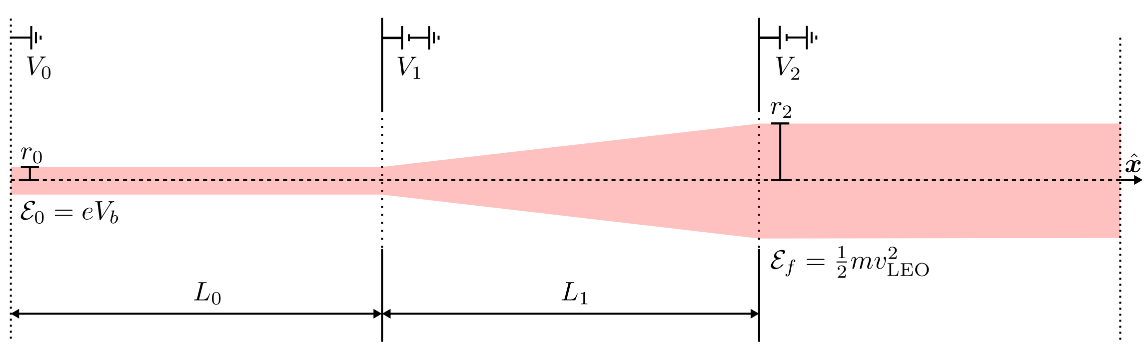

Figure 4.4: Thin conductor lens design

Figure 4.4 shows a collimated ion beam traveling in direction $\hat{\boldsymbol{x}}$ with initial beam voltage V_b

and radius r_0 entering the telescope. This design is hereafter referred to as the "thin-conductor" telescope to differentiate from designs discussed later. It is so named because the telescope is characterized by thin conductors placed along $\hat{\boldsymbol{x}}$ at distances L_0 and $L_0 + L_1$. One representative geometry of the conductors used commonly in ion optics as viewed down $\hat{\boldsymbol{x}}$ is shown in Figure 4.5. It is clearly stated here that the conductor geometry — provided the thickness of the material walls are sufficient to eliminate external fields — is inconsequential to ion dynamics. The geometry of the negative space through which the ions travel dictates their trajectories. The means by which this geometry changes the beam focus is described in detail by the references provided and is therefore not detailed here.

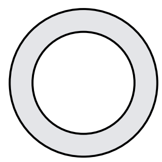

Figure 4.5: Down-$\hat{\boldsymbol{x}}$-axis conductor geometry for general electrostatic lens design

As the beam leaves the ion gun — the end of which is indicated by the dashed line on the far left of Figure 4.4 — with radius r_0 and energy $\mathcal{E}_0$ it passes through a diverging lens defined by the first conductor charged to V_1 and then a converging lens charged to V_2. It is important to note that V_1 and V_2 are defined relative to the initial beam voltage V_b. The expanded beam leaves the second lens with radius r_2 and the desired LEO energy $\mathcal{E}_f$. These design parameters indicate that the value of V_2 must correspond to a particle velocity of roughly 7 km/s to match LEO orbital velocity. As with the Jumbo chamber at AFRL, ECLIPS is design to use Ar^+ to simulate the cations of the ionosphere. The relative kinetic energy that accurately simulates LEO orbital velocity for this element is $\sim$ 11 eV, though this can be tuned for different atmospheric elements. In practice, Argon is a good choice for the plasma as it is an extremely non-reactive element even in its ionized state, which will result in fewer arcing events and in turn longer lifetime for the ion source filament.

A primary motivation of the ion optics design is to increase the area of the final beam so that experiments on relatively large objects can be conducted. The obvious motivation here is that investigating the wake behind an object of diameter 1 mm is more challenging than the wake behind an object of, say, 10 cm. On the other hand, the effective simulated density described in Eq. (4.5) decreases as the square of the beam magnification $M = r_2/r_0$. The effective density after expansion n_f is written below.

$$n_f = \frac{I}{eA_f v_f} = \frac{I}{e\pi M^2 r_0^2 v_f} \tag{4.9}$$

The inverse square dependence on the magnification means that, while larger experimental volumes are desirable, the simulated density after the beam may fall below that in LEO. Additional motivation to keep M reasonably small is the density scaling law shown in Eq. (4.6) which enables self-similarity between scaled experiments. As an example, the ion gun on the ECLIPS chamber — which was purchased specifically for its low-energy, high-current output — widened and accelerated to the proper energy will theoretically create a 6 cm diameter beam with roughly LEO densities. Given the condition in Eq. (4.7) (replace the left-hand-side with r_2 from Figure 4.4) the experiment object radius R_0 should be kept less than ~ 1 cm. For wake shaping experiments, the potentials will also need to remain small so that they die off before the beam edge as discussed previously. At the time of purchase, no ion gun with a better balance of low energy and high current could be sourced commercially for the ECLIPS chamber. Future facilities applying improved ion guns would enable larger experiment volumes.

Once a desired magnification is determined given the considerations above, the beam energy, spacings, and voltages in an ion telescope like that pictured in Figure 4.4 must be tuned to achieve it. Reference [49] provides a set of equations which indicate that the telescopic properties come down the voltage and length ratios, V_1/V_2 and L_1/L_2. This initial simulation is run to ensure that the simulation parameters applied result in theoretically-predictable results.

A SIMION simulation is run replicating a lens design presented in [49] which gives a magnification $M = 1.51$. This results in a final beam radius far too small for practical investigation of plasma wake behavior, but the design allows for validation of the SIMION simulation parameters.

This design is identified as "ideal" because it matches the theory.

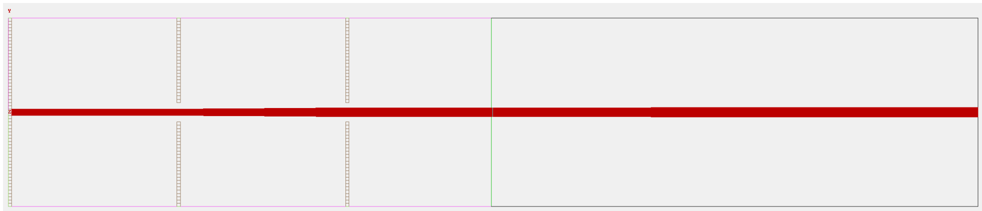

Figure 4.6: Transverse view of ideal thin-conductor ion telescope

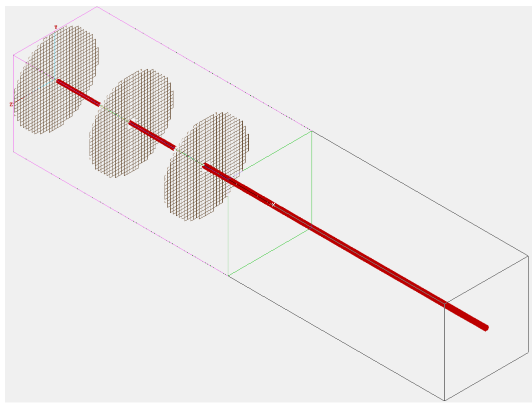

Figure 4.7: Isometric view of ideal thin-conductor ion telescope

Transverse and isometric views of the SIMION simulation results are shown in Figures 4.6 and 4.7 for the telescope design with lengths $L_1 = L_2 = 10$ cm and voltages $V_1 = -14V$ and $V_2 = -5V$. For the initial lens design here and following, spacecharge effects within the beam are neglected. In this way, the lens design problem comes down to tracing rays of charged particles through the voltage gradients in the telescope. In the simulation, 1000 ions are generated as a beam at the left (in Figure 4.6) with energy $\mathcal{E}_0 = 0.1$ eV and diameter $r_0 = 1$ mm.

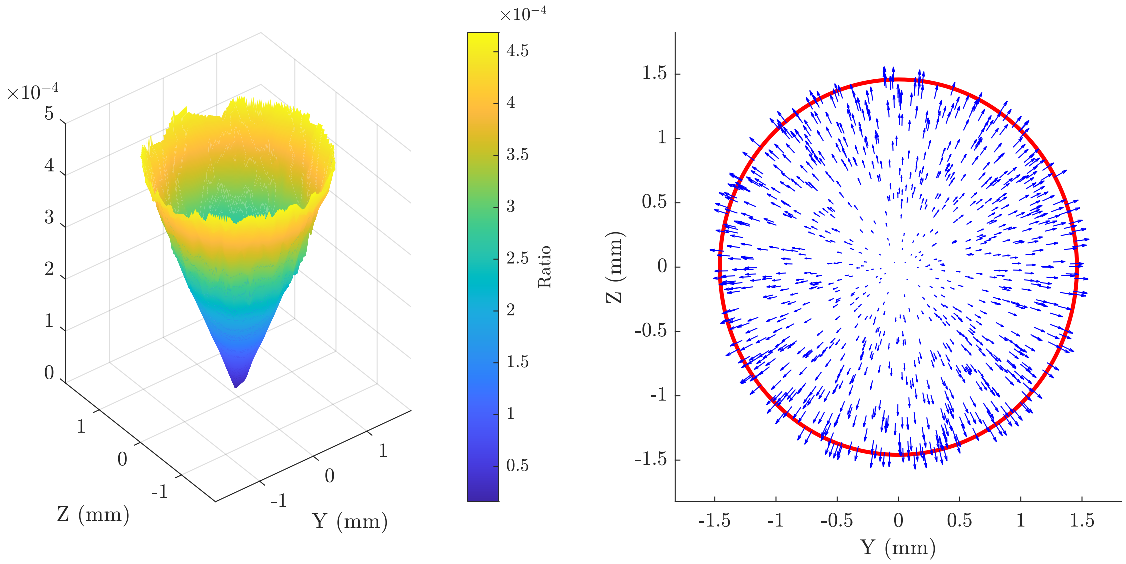

(a) Ratio of transverse to axial velocity magnitude (b) Down-axis ($-\hat{\boldsymbol{x}}$) view of particle trajectories

Figure 4.8: Quantification of collimation of ideal telescope simulation

The collimation of the beam is quantified in Figure 4.8, which shows the ratio of the transverse to axial velocity $\sqrt{\frac{v_y^2+v_z^2}{v_x^2}}$ and the particle trajectories both evaluated at the far right of the simulation volume. The velocity ratio in Figure 4.8(a) indicates that the beam is quite collimated, as its maximal value is well below 1%. As expected the exterior of the beam is less collimated than the interior. This is confirmed by the off-axis trajectories in Figure 4.8(b). The circle drawn on the figure indicates the final beam radius. Given the initial beam radius $r_0 = 1$ mm and the expanded beam radius $r_2 = 1.49$ mm, the magnification indicated in reference [49] is replicated to high accuracy.

The primary motivation of this design is to validate the simulation parameter set in SIMION again analytic solutions. With the success of the ideal thin-lens design, SIMION is applied to design lenses with much larger magnifications so as to increase LEO plasma wake experiment volume.

4.4.2.3 Large Magnification Thin Lens Telescope Design

In practice, magnifications much larger than this are desired, as a 1.5 mm beam will not generate a wake feasible to probe in experiments. Consider the alternative thin-conductor telescope

Figure 4.9: Transverse view of non-ideal thin-conductor ion telescope

design pictured in Figures 4.9 and 4.10.

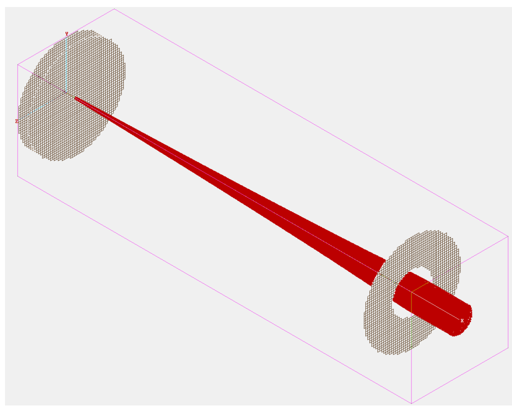

Figure 4.10: Isometric view of non-ideal thin-conductor ion telescope

This design spaces thin conductors at $L_0 = 1$ cm and $L_1 = 35$ cm charged to $V_1 = -500$ V and $V_2 = 5$ V with initial energy $\mathcal{E}_0 = 100$ eV to achieve a magnification of 12.70. It is identified as "non-ideal" henceforth because the lens design framework in reference [49] does not predict this parameter set will create a telescope. The reason for the discrepancy is that the theory used is applicable only weak (low magnification) lenses. The final beam energy achieved is 20 eV, which is higher than the desired 5 eV. A deceleration grid could be applied to further reduce the energy to achieve the desired supersonics.

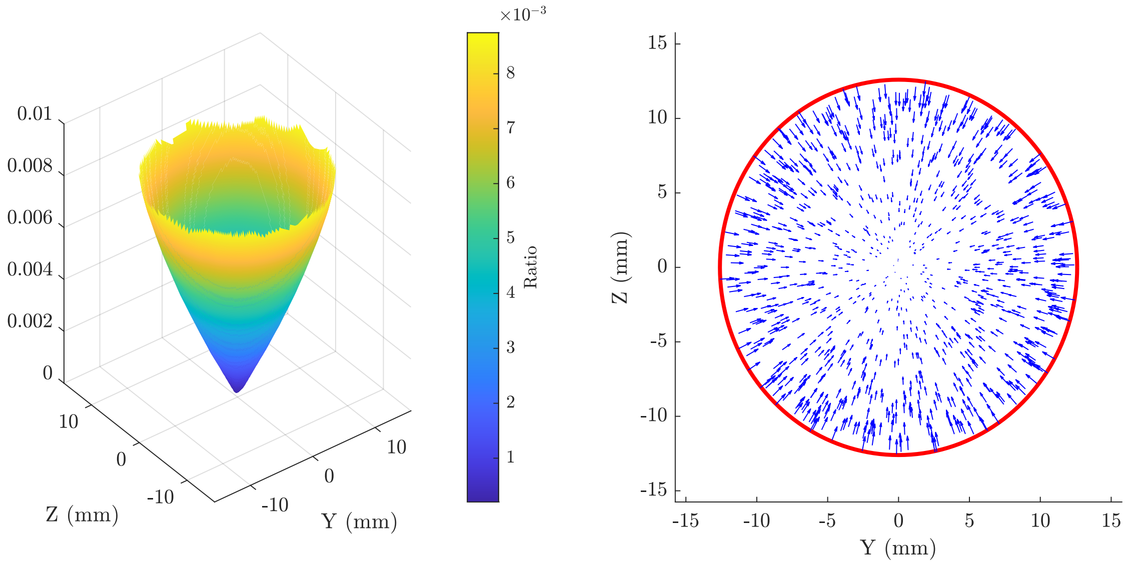

(a) Ratio of transverse to axial velocity magnitude (b) Down-axis ($-\hat{\boldsymbol{x}}$) view of particle trajectories

Figure 4.11: Quantification of collimation of non-ideal telescope simulation

The collimation of the non-ideal thin-lens telescope is quantified in Figure 4.11. This design was developed through trial and error, using only the general trends predicted by the theory to inform spacings and voltages. Despite this, a high degree of collimation is indicated in Figure 4.11(a). Note that Figure 4.11(b) shows that the final beam converges slightly, whereas Figure 4.8(b) was slightly divergent.

The reason the theory in reference [49] does not apply to thick lenses is because it assumes a kink in a particle's trajectory occurs at the plane defined by the center of the thin conductor. For stronger lenses, this is not the case. Instead, the larger fields at the conductors result in continuous deflection near the lens. Additionally, the deflection can begin in planes other than that at the center of the thin conductors. These circumstance are analogous to a thick optical lens.[61] A more practical — though less analytically insightful — lens design guide is provided in reference [69], as it includes approximations of the physics of thick lenses. The results of the non-ideal thin-conductor telescope simulation qualitatively matched those described in this source. Precise comparison was not attempted, as errors as large as 10% relative to experimental data were reported. Additionally, even if the design were perfected such that SIMION results indicated a truly ideal telescope as predicted by this more-precise source, the lens parameters will need to be tuned again after the telescope is constructed to account for imperfections. Therefore, the design of the telescopes discussed throughout this chapter will be tuned only to the point at which design considerations are sufficiently illustrated.

4.4.2.4 Thick Lens Telescope Design

Now that two thin-lens configurations have been designed and simulated, an alternative lens geometry is considered. Consider the thick-conductor telescope pictured in Figure 4.12. The physical layout of this telescope is in some senses the inverse of the thin-lens telescope: three thick conductors held at fixed potentials with two thin gaps separating them. In this latter design, the lenses are the gaps, whereas the thin conductors served to modify particle trajectories in the earlier design considered.

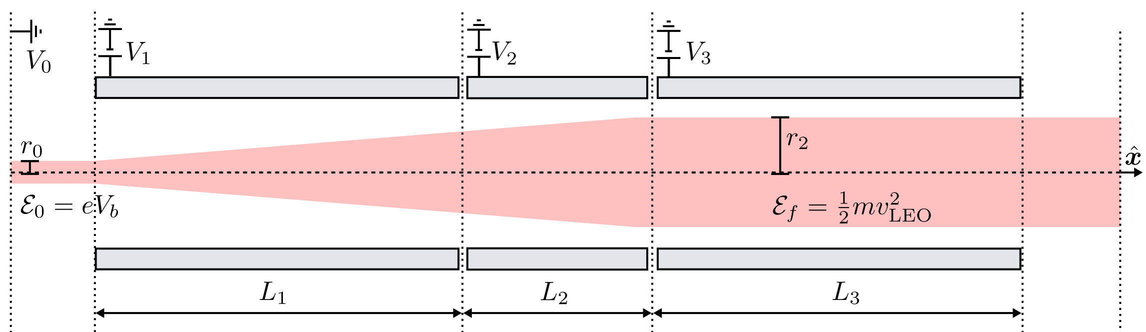

Figure 4.12: Thick conductor telescope design

The design of this telescopic system is informed by reference [1], though as with the theories considered for the thin-lens system, the lens parameters need to be tuned to achieve telescoping both when applied in SIMION and again when constructed. In theory, the thick-lens design has two telescopic modes which correspond to $V_1 = V_3$ and $V_2 = V_3$. The former of these is a so-called Einzel or symmetric lens. The symmetry in both voltage and geometry results in a telescope that changes the focus but not the energy of the beam. This constrains what the output from the ECLIPS (or other facility) ion gun is. Practically speaking, this is undesirable as the ion gun will have certain energies at which it can put out higher density or a more collimated beam. Therefore, a telescope that allows tuning of both the magnification and energy is desired. Constraining $V_2 = V_3$ achieves this, according to reference [1], for all values of V_1.

Figure 4.13: Transverse view of thick-conductor ion telescope

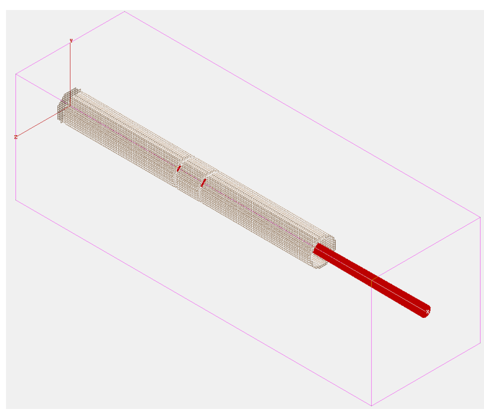

Figure 4.14: Isometric view of thick-conductor ion telescope

SIMION simulations are run on a thick-lens telescope design. The lens geometry is shown in Figures 4.13 and 4.14. In practice, the theoretical prediction that telescoping is achieved for arbitrary V_1 given that $V_2 = V_3$ does not hold. Instead, the three voltages must be tuned to achieve the desired collimation as shown in Figure 4.15. The parameter set applied in simulation this is $\mathcal{E}_0 = 10$ eV, $V_1 = -73$ V, $V_2 = V_3 = -30$ V, $L_1 = L_3 = 10$ cm, $L_2 = 4$ cm and the resulting magnification is 8.75.

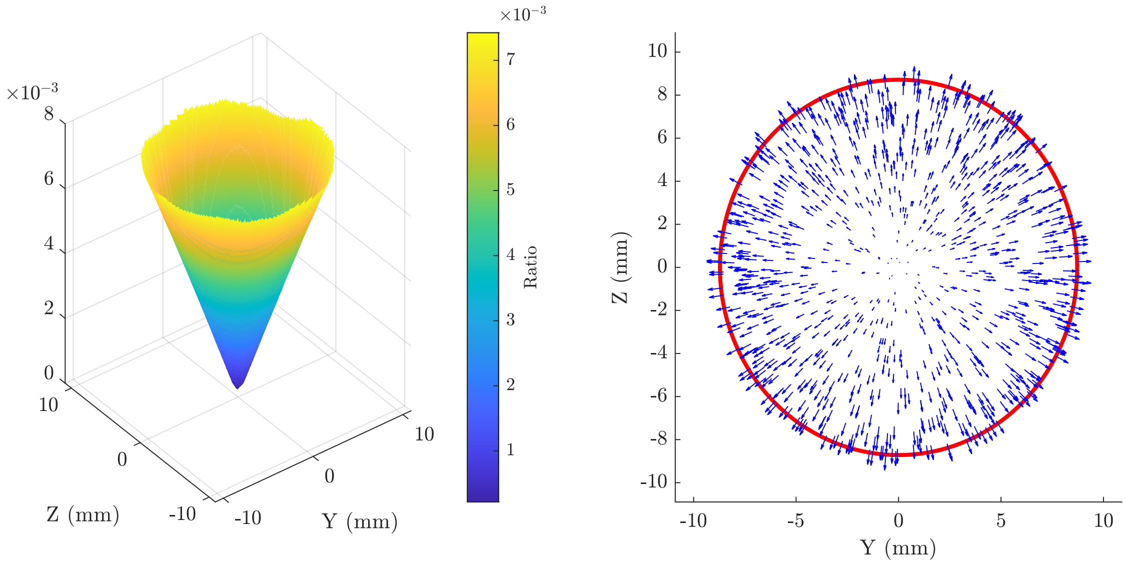

(a) Ratio of transverse to axial velocity magnitude (b) Down-axis ($-\hat{\boldsymbol{x}}$) view of particle trajectories

Figure 4.15: Quantification of collimation of non-ideal telescope simulation

4.4.2.5 Thick Lens Spacecharge Telescope Design

With notional lens designs based on ray tracing techniques complete, an approximate spacecharge spreading effect is included in the SIMION simulations and the beam's behavior is analyzed. The voltages and spacings are then tuned to create a telescope that incorporates the effects of the spacecharge spreading. The lens parameters for this telescope design are included in Table 4.1.

$\mathcal{E}_0$ (eV)	V_1 (V)	V_2 (V)	V_3 (V)	L_1 (cm)	L_2 (cm)	L_3 (cm)	r_0 (cm)	M
40	-300	-10	-10	14	5	14	0.1	33

Table 4.1: Final Ion Telescope Design Parameters

The thick-lens spacecharge telescope geometry is shown in Figure 4.16 for beam current 2 μA — approximately what the ECLIPS ion gun sources at the described beam energy. It is immediately clear that the spacecharge spreading effect is substantial. Indeed the telescope parameters in Table 4.1 were actually tuned to reduce the effect. This is accomplished by accelerating the beam more in the first conductor, as higher energy beams remain coherent over larger spatial scales.

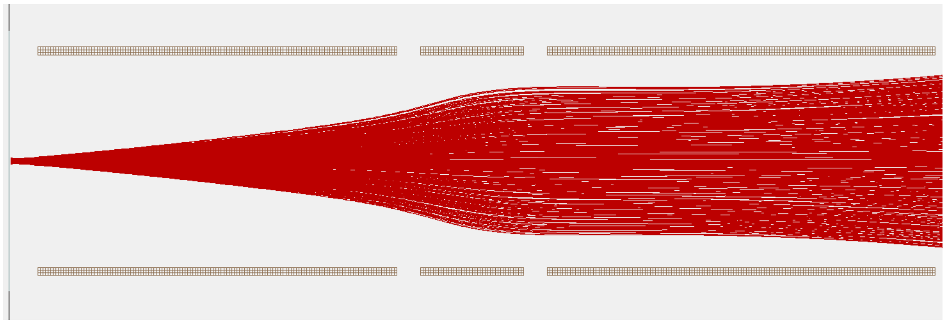

Figure 4.16: Transverse view of thick-conductor spacecharge ion telescope

The collimation results shown in Figure 4.17 are significantly worse than those in the previous simulations. This is because the spacecharge spreading cannot be fully mitigated given the geometry of the thick-lens spacecharge telescope. Though results of the thin-lens spacecharge telescope are not presented here, simulations indicated that the collimation was much worse, so the thick-lens design was selected. In contrast to the collimation challenges, the spacecharge spreading effect results in much larger magnifications with relatively low conductor potentials relative to designs in which spacecharge is ignored or mitigated by beam acceleration or other techniques. By modulating the beam output energy and V_1, the spacecharge spreading can be tuned, though this is clearly not an independent tuning parameter based on the discussion previously.

According to SIMION simulations and the published specifications of the ECLIPS ion gun, the thick-lens spacecharge telescope design should create a collimated beam of ~ 6 cm with approximately the correct LEO densities ($\sim 10^{12}$ m^{-3}) and relative velocities ($\sim 10^4$ m/s). While this beam radius is tight — though feasible — for measurement of the wake, the parameters from this design reasonably replicate LEO. Further tuning of this design to attempt to achieve precise LEO simulation is not advised by the creators of SIMION, as their documentation indicates that the spacecharge model is not applicable for low-energy, high-current beams like the ECLIPS ion gun simulated. Therefore, as discussed previously, the optics will be constructed as designed and tuned to achieve the desired parameters.

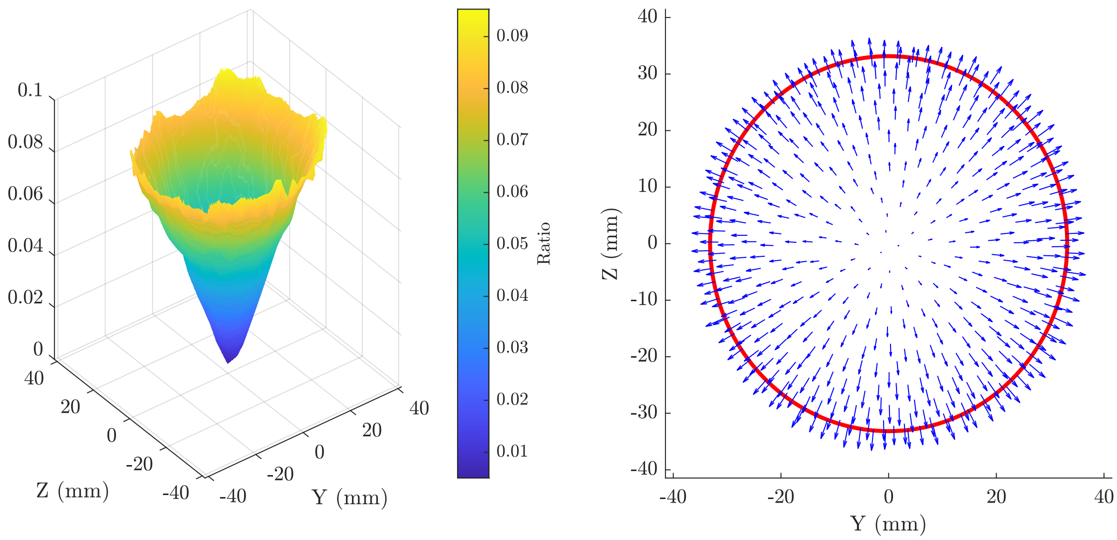

(a) Ratio of transverse to axial velocity magnitude (b) Down-axis ($-\hat{\boldsymbol{x}}$) view of particle trajectories

Figure 4.17: Quantification of collimation of thick-lens spacecharge telescope simulation

The lens design presented in 4.1 is 33 cm long. Given the configuration in 4.3 and the 1 m height of ECLIPS, this leaves roughly 30 cm for experiments to be conducted. Given that LEO craft generate wakes that close after 1 body radius, the constraint to use a small object imposed by the beam radius serves to ensure the wake will not extend beyond the allotted experiment volume.

While the design described above seeks to accurately simulate LEO densities, the primary focus of this chapter is to generate closed wakes that can feasibly be studied to provide insight into electrostatic actuation techniques. Therefore the parameters for an alternative design with much larger experimental volume are given in Table 4.2. The SIMION result is shown in Figure 4.18

$\mathcal{E}_0$ (eV)	V_1 (V)	V_2 (V)	V_3 (V)	L_1 (cm)	L_2 (cm)	L_3 (cm)	r_0 (cm)	M
40	-210	39	40	14	5	14	0.1	80

Table 4.2: Final Ion Telescope Design Parameters

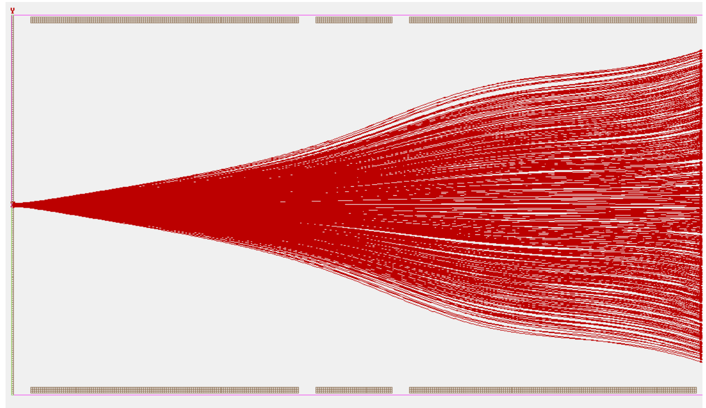

Figure 4.18: Transverse view of large-magnification spacecharge thick-lens telescope

This final telescope achieves a beam diameter of roughly 16 cm simulating density of $\sim 5 \times 10^{10}$ m^{-3}. The telescope as before is 33 cm long. This would fit inside the stated ECLIPS experimental volume without resulting in densities too low for wake closure to occur according to Nascap-2k simulations.

As before, the velocity and collimation are not tuned carefully in SIMION as this process would necessarily need to be repeated once the optics were constructed. Interestingly, this optic design was highly sensitive to differences in V_2 and V_3 as predicted by the theory. The 1 V different serves to minimize the spreading of the beam when it departs the optics. The lower-magnification spacecharge telescope described previously — while it did hold these potentials equal — was far less sensitive to these differences.

4.4.2.6 Wake Closure Analysis

This chapter is aimed at simulating plasma wakes terrestrially. Two telescopes leveraging spacecharge spreading have been described which seek to achieve different experimental parameters. The first of these is designed to replicates LEO densities. A Nascap-2k simulation is shown in Figure 4.19 considering an Argon plasma of the relevant densities (10^{12} m^{-3}) and energies (5.5 eV) flowing past a 10 cm craft. This craft radius — which is larger than the beam in the optics design shown in Figure 4.16 — is applied because Nascap-2k simulations of smaller craft did not converge for the environmental parameters. These simulation results are considered to apply to more realistic ∼1 cm objects given that these are still significantly larger than the Debye length in the plasma (∼2 mm).

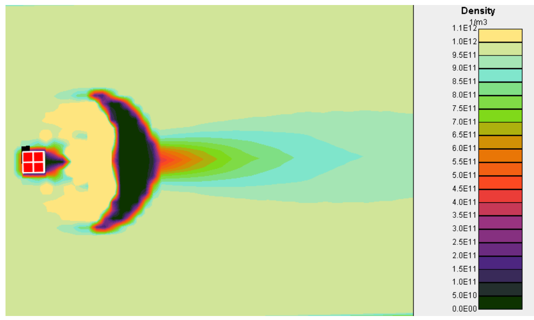

Figure 4.19: Nascap-2k simulation of telescope simulating LEO-like densities

Figure 4.19 shows a plasma wake similar in size and dimension to those in Chapter 3. Given that the appropriate energy and density are applied here, this is unsurprising. The key point here is that the wake of this 10 cm object closes well before the expected experimental spatial limits (33 cm along the wake axis).

Interestingly, the Argon plasma simulated seems to enhance ion focusing behaviors immediately behind the wake. This results in simulated large low-ion-density region behind the spacecraft. While this sort of structure has been predicted behind negative spacecraft previously [58] this extreme enhancement is unexpected. This effect is not relevant to electrostatic actuation, and will be considered in future experiments.

The results shown in Figure 4.19 simulate a density of 5×10^{10} m^{-3} with the same energy described previously. In general, the results are similar to the LEO-like simulation, but are extended in the direction of ion flow. The lower density serves to magnify supersonic effects, resulting in larger wake geometries.

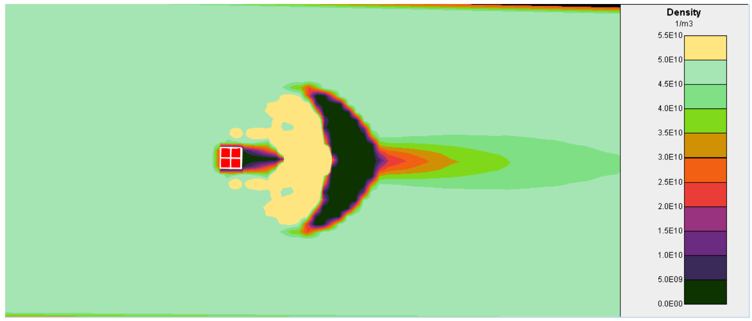

Figure 4.20: Nascap-2k simulation of telescope maximizing experiment area

The extended wake in this final simulation allows for larger experimental area in the ECLIPS or other chambers at the cost of lower simulated densities. Given that the focus of this chapter is the development of closed LEO plasma wake simulation capabilities, the deviation from LEO densities is accepted as insight into wake geometry and dynamics can still be obtained. In this case, care should be taken to ensure that the plasma wake does not extend out of the desired experiment volume.

4.5 Results & Summary of Goal 3

The objective of this aspect of the project was to design an improved simulation facility for studying charged wake behavior and wake shaping techniques. The ECLIPS chamber is presented as the frame for this discussion, though the design considerations discussed throughout this chapter apply generally to chambers seeking to simulate LEO spacecraft-plasma interactions. First, a conservative condition for sufficient vacuum for LEO experiments is derived based on charge exchange between the low-energy neutrals not removed by the pumping system and the high-energy (relative to the neutrals) Ar^+ ions in the beam. It is shown that for these extremely low energy experiments (relative to $\geq\sim$ 1 keV energies common in plasma experiments) charge exchange is minimal. This means that the ion plasma in the chamber remains mono-energetic as in LEO.

Two distinct techniques are presented to generate electron and ion plasmas to simulate LEO spacecraft-plasma interactions. Electrons are sourced with a filament selected and biased to achieve the desired energies and densities. Simulation of the flowing ion plasma experiments by LEO spacecraft is more complicated, as significant deviations in collimation, density, and energy result in wake behavior unrepresentative of LEO. A novel simulation system is proposed for the ion front and a variety of different designs are presented, simulated, and discussed with assumptions on the system parameters relaxed as designs are iterated. Two final designs with different motivations are simulated in Nascap-2k with results showing that experimental parameters in ECLIPS will enable simulation of closed plasma wakes. With this result, it is expected that wake geometries and behaviors can be investigated experimentally. This is a major contribution to the study of electrostatic actuation in LEO plasma wakes.

Chapter 5

Electrostatic Actuation Control Techniques

The final goal is the crux of this research. The development of robust control techniques is complex regardless of the actuation method, as each mission has different physical characteristics, objectives, and constraints. Electrostatic actuation in LEO has several unique challenges described throughout this dissertation. The insight gained from projects discussed previously provides a foundation to investigate the feasibility of electrostatic actuation in LEO plasma wakes.

A technique for modeling electrostatic interactions between spacecraft in motion is prerequisite to the development of electrostatic actuation controllers. In Chapter 2, MSM was shown to accurately model system capacitances and electric fields over significant system reconfiguration, indicating that the method is well suited for modeling charged spacecraft dynamics. Significant insight for control applications was gained while deriving the system capacitance and electric field equations. The $1/r^2$ dependence of the Coulomb force means that the control authority for the technique decreases with relative distances. This couples the problems of gain selection and reference trajectory design. The position-dependence of the capacitance adds further complexity, as it is harder to force charge onto two nearby objects with same-signed potentials. Put in practical terms: more voltage is required to generate repulsive forces between objects in close proximity. These two insights gained from investigating the application of MSM to time-varying structures taken together imply that there is a "sweet spot" for electrostatic actuation in terms of relative distances. This has significant implications for the development of control techniques and reference trajectories.

The simulations and experimental campaigns described in Chapter 3 evidence the importance of keeping system voltages low. The massive power expense associated with wake collapse decreases the feasibility of the technique, as large trade-offs would be required in other mission areas. Additionally, the increase in plasma density will attenuate electric fields, resulting in an additional decrease to control authority to those identified in Chapter 2. Another major conclusion drawn was that negative voltages — though they can lead to wake collapse — cost minimal power to source in the wake. On the other hand, the low electron temperature in LEO and decreased plasma shielding in the wake result in even very small positive voltages requiring power. These two physical phenomena motivate the use of negative control voltages small enough to not cause wake collapse during electrostatic actuation. A parametric study was run on a prototypical formation concluding that the wake-forming craft must be roughly 3 m in diameter in order to charge a small spacecraft in its wake to -1 kV without collapsing the wake. The lack of spacecraft of this diameter and larger motivated experimental studies of wake shaping which provided significant insight into physical systems difficult to model using conventional simulation techniques. Finally, Chapter 4 outlines improved experimental facility design and techniques for future study of wake shaping and electrostatic actuation generally.

Dependence on relative position, the concern of wake collapse, and power requirements asymmetric in the sign of the control variable are not common challenges in control design. Unfortunately, these and other complications strongly affect the performance of the control and can lead to system instability. The degree to which a controller can account for the effects is highly implementation specific, depending on the choice of control variable, the accuracy of linearized models, computational limitations, and system configuration. The goal of this piece of the project — and of this research generally — is to develop electrostatic actuation controllers that could feasibly be used for formation control in LEO given modern spacecraft power systems. The insights gained from previous sections are imperative to this effort, as they provide bounds on acceptable relative distances and control usage.

This chapter begins with an outline of the problem to be solved, defining the electrostatic actuation system under consideration. Dynamics models are derived and various controllers are applied to settle the system over a variety of different initial conditions. A discussion of reference trajectory precedes final simulation results and conclusion.

5.1 Problem Statement

The general system configuration for each control simulation is shown in Figure 5.1. An uncharged leader craft equipped with with a set of isolated, conducting spheres — identified in the figure and hereafter as the charge structure — creates a plasma wake in which a charged follower resides. The wake is considered static for all simulations to follow.

Various controllers are applied to modulate voltage or charge on the follower and charge structure such that some desired relative motion is achieved. For simulations to date, the wake is assumed to be static regardless of sourced potentials and to consist of perfect vacuum, as no model exists that can be integrated at reasonable speeds. It is assumed that the wake is large enough as discussed in Chapter 3 such that wake collapse will not occur. This implies that leader diameter is considered the independent variable when considering wake collapse as in Chapter 3.

The two frames used throughout the problem described above are the Earth Centered Inertial (ECI) frame and the Hill-Clohessy-Wiltshire (HCW) frame, denoted $\mathcal{N}$ and $\mathcal{H}$, respectively. The formal definitions of the frames are provided below where $\hat{\boldsymbol{n}}_i$ signifies an inertial unit vector, $\hat{\boldsymbol{r}}_\mathrm{L}$ is the leader's normalized position relative to the center of the earth, and $\hat{\boldsymbol{h}}_\mathrm{L}$ is the direction of the

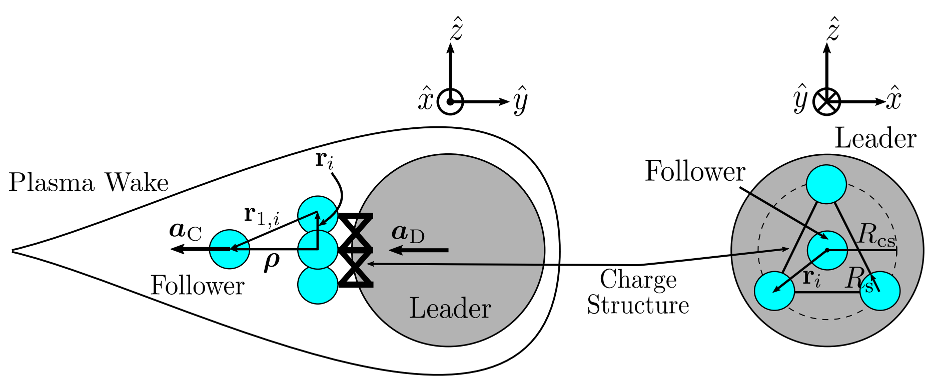

Figure 5.1: Illustration of electrostatic actuation technique in LEO

leader's angular momentum vector.

$$\mathcal{N} : \{\hat{\boldsymbol{n}}_1, \hat{\boldsymbol{n}}_2, \hat{\boldsymbol{n}}_3\}\ ,\ \mathcal{H} : \{\hat{\boldsymbol{r}}_\mathrm{L}, \hat{\boldsymbol{h}}_\mathrm{L} \times \hat{\boldsymbol{r}}_\mathrm{L}, \hat{\boldsymbol{h}}_\mathrm{L}\} \tag{5.1}$$

As before, bolded quantities indicate vectors. A left superscript indicates the frame in which a given vector is defined, while the hat notation indicates a unit vector (i.e. ${}^{\mathcal{N}}\hat{\boldsymbol{x}}$ indicates the unit vector of $\boldsymbol{x}$ expressed in the inertial frame). In general, matrices are signified via square brackets, though Direction Cosine Matrices (DCMs) are identified, for example, by the form $[\mathcal{HN}]$ indicating the mapping of a right multiplied vector from the inertial to the Hill frame.

$${}^{\mathcal{H}}\boldsymbol{x} = [\mathcal{HN}]{}^{\mathcal{N}}\boldsymbol{x}\ ,\ [\mathcal{HN}] = [{}^{\mathcal{H}}\hat{\boldsymbol{n}}_1, {}^{\mathcal{H}}\hat{\boldsymbol{n}}_2, {}^{\mathcal{H}}\hat{\boldsymbol{n}}_3] \tag{5.2}$$

Finally, a notation for time derivatives as seen by different frames is introduced.

$$\dot{\boldsymbol{x}} = \frac{{}^{\mathcal{N}}\partial \boldsymbol{x}}{\partial t}\ ,\ \boldsymbol{x}' = \frac{{}^{\mathcal{H}}\partial \boldsymbol{x}}{\partial t} \tag{5.3}$$

Additional notations will be introduced throughout the text, but the definitions above provide a baseline for beginning the analysis.

The simulated environment includes two-body and J_2 gravity, drag, and solar radiation pressure (SRP) in addition to the Coulomb acceleration. Gravitational accelerations dominate in this orbit, with drag and SRP resulting in accelerations of roughly 10^{-7} m/s. The controller includes linearized models of a subset of these — two-body gravity, drag, and Coulomb accelerations. J2 gravity, SRP, and variations in atmospheric density are included as unmodeled perturbations, providing insight into the robustness of the controllers.

5.2 Nonlinear Equations of Motion

Four perturbations are included in the simplified model used to simulate the environment: Coulomb forces, two-body and J_2 gravity, orbital drag, and SRP. For the following discussion, it is useful to define $\boldsymbol{\rho}$ as the difference of the positions of the leader and follower.

$$\boldsymbol{\rho} = \boldsymbol{r}_\mathrm{f} - \boldsymbol{r}_\mathrm{L} \tag{5.4}$$

5.2.1 Coulomb Acceleration

The Coulomb acceleration of the follower relative to the leader is calculated from the charge and mass of the follower — Q_f and m_f, respectively — and the electric field of the leader $\boldsymbol{E}_\mathrm{L}$ generated by the charge structure pictured in Figure 5.1.

$$\boldsymbol{a}_\mathrm{C}(\boldsymbol{X},\boldsymbol{V}) = \frac{1}{m_\mathrm{f}} Q_\mathrm{f} \boldsymbol{E}_\mathrm{L}(\boldsymbol{X},\boldsymbol{V}) \tag{5.5}$$

The proximity of the follower to the charge structure on the leader means that a mutual capacitance exists between the two objects. This effect is described by the relation between the voltage and the charge on a given object. The voltage V_i on a given sphere subject to its own charge Q_i and the charge Q_j on nearby spheres is calculated.

$$V_i = k_\mathrm{C}\frac{Q_i}{R_i} + k_\mathrm{C}\sum_{j=1,j\neq i}^{n}\frac{Q_j}{r_{i,j}} \tag{5.6}$$

Here, $k_\mathrm{C} = 8.99 \times 10^9$ Nm^2/C^2 is Coulomb's constant, R_i is the radius of the i^th sphere, and $r_{i,j}$ is the center-to-center distance between the i^th and j^th spheres. Throughout this discussion, the subscript 1 refers to the follower and subscripts 2 through n refer to the spheres on the charge structure. The relation above can be rewritten into a single matrix equation.

$$\begin{pmatrix} V_1 \\ V_2 \\ \vdots \\ V_n \end{pmatrix} = k_\mathrm{C} \begin{bmatrix} 1/R_1 & 1/r_{1,2} & \dots & 1/r_{1,n} \\ 1/r_{2,1} & 1/R_2 & \dots & 2/r_{2,n} \\ \vdots & \vdots & \ddots & \vdots \\ 1/r_{n,1} & 1/r_{n,2} & \dots & 1/R_n \end{bmatrix} \begin{pmatrix} Q_1 \\ Q_2 \\ \vdots \\ Q_n \end{pmatrix} \tag{5.7}$$

Written in a more compact fashion

$$\boldsymbol{V} = [S]\boldsymbol{Q} \tag{5.8}$$

where $[S]$ is the elastance matrix.[84] Another well-known expression relating charge to voltage, $\mathbf{Q} = [C]\mathbf{V}$ indicates that the capacitance is the inverse of the elastance matrix.

$$\mathbf{Q} = [S]^{-1}\mathbf{V} \tag{5.9}$$

This form is preferable, as the voltage is the control variable and the charge dictates the dynamics. The charge on the follower can be written as an inner product between the first row of the capacitance and the voltage vector. As displayed in Figure 5.1 above, the follower craft is simulated as a single sphere, though in general Q_{f} in Eq. (5.5) represents the total charge on a follower simulated with n MSM spheres.

$$Q_{\mathrm{F}} = Q_1 = \boldsymbol{C}_1^T \boldsymbol{V} \tag{5.10}$$

The vector $\boldsymbol{C}_i$ indicates the i^{th} row of the capacitance matrix. The electric field from the charge structure $\boldsymbol{E}_{\mathrm{L}}$ at the position of the follower can be calculated by summing the individual fields from each of the spheres on the charge structure.

$$\boldsymbol{E}_{\mathrm{L}}(\boldsymbol{X}, \boldsymbol{V}) = k_{\mathrm{C}} \sum_{i=2}^{n} \frac{\boldsymbol{C}_i^T \boldsymbol{V}}{||\boldsymbol{\rho} - \boldsymbol{r}_i||^3} (\boldsymbol{\rho} - \boldsymbol{r}_i) = k_{\mathrm{C}} \sum_{i=2}^{n} \frac{\boldsymbol{C}_i^T \boldsymbol{V}}{r_{1,i}^3} \boldsymbol{r}_{1,i} \tag{5.11}$$

Note that the vector pointing from the i$^{\text{th}}$ sphere to the follower can be written in terms of the state variable ($\boldsymbol{r}_{1,i} = \boldsymbol{\rho} - \boldsymbol{r}_i$). Substituting Eqs. (5.10) and (5.11) into (5.5) yields the non-linear acceleration of the follower subject to the leader.

$$\boldsymbol{a}_{\mathrm{C}}(\boldsymbol{X}, \boldsymbol{V}) = \frac{k_{\mathrm{C}}}{m_{\mathrm{r}}} \boldsymbol{C}_1^T \boldsymbol{V} \sum_{i=2}^{n} \frac{\boldsymbol{C}_i^T \boldsymbol{V}}{r_{1,i}^3} \boldsymbol{r}_{1,i} \tag{5.12}$$

An additional complication presents itself in Eq. (5.12). The coupling through the mutual capacitance described by Eq. (5.7) means that the proximity of two nearby objects affects their charge. To demonstrate this effect, Eq. (5.10) is expanded. The dual subscripts $C_{i,j}$ indicate the position of a scalar element within the capacitance matrix.

$$Q_1 = \boldsymbol{C}_1^T \boldsymbol{V} = C_{1,1} V_1 + \sum_{i=2}^{n} C_{1,i} V_i \tag{5.13}$$

By convention, the self capacitance of an object ($C_{1,1}$) is always positive, while the mutual capacitance terms ($C_{1,i}$) are always negative, though both are position-dependent quantities.[84] Physically, this results in nearby objects of the same voltage causing a decrease in charge on — in this case — the follower craft. This means that there are sets of voltages and relative positions for which a large enough Coulomb acceleration cannot be generated to counter differential drag as indicated by the condition in Eq. (5.18).

To demonstrate this, consider the mission scenario discussed above and recall that the Coulomb accelerations between the leader and follower are proportional to the charge products. The norm of Eq. (5.12) is expanded below. For the purpose of clearly explaining the limits on attainable voltages, all charge structure spheres are assumed to have the same potential V_2. As discussed previously, the desired Coulomb acceleration is that which perfectly opposes the drag acceleration in the along-track direction (a_{Drag_y}).

$$|\boldsymbol{a}_{\mathrm{C}}(\boldsymbol{X},\boldsymbol{V})| = -a_{\mathrm{Drag}_y} = \frac{k_{\mathrm{C}}}{m_{\mathrm{r}}}\left\{\left(C_1V_1 + V_2\sum_{i=2}^{n} C_{1,i}\right)\left(V_1\sum_{i=2}^{n}\frac{C_{1,i}}{r_{1,i}^2} + V_2\sum_{i=2,j=2}^{n}\frac{C_{i,j}}{r_{i,j}^2}\right)\right\} \tag{5.14}$$

This equation can be re-expressed as a quadratic in V_2, assuming a charge structure voltage is desired to be found for a given follower voltage V_1. The following substitutions are made to simplify the equation. The conditions in this equation recall the discussion of the signs of self and mutual capacitance previous.

$$\begin{aligned} \alpha &= C_1 > 0 \\ \beta &= \sum_{i=2}^{n} C_{1,i} < 0 \\ \gamma &= \sum_{i=2}^{n}\frac{C_{1,i}}{r_{1,i}^2} < 0 \\ \delta &= \sum_{i=2,j=2}^{n}\frac{C_{i,j}}{r_{i,j}^2} < 0 \end{aligned} \tag{5.15}$$

Eq. (5.14) is written as a quadratic in V_2.

$$0 = \beta\delta V_2^2 + (\alpha\delta + \beta\gamma)V_1V_2 + (\alpha\gamma V_1^2 + \frac{m_{\mathrm{r}}a_{\mathrm{Drag}_y}}{k_{\mathrm{C}}}) \tag{5.16}$$

The condition on real voltages satisfying this expression come from the square root term in the quadratic equation. This condition is written

$$(\alpha\delta + \beta\gamma)^2V_1^2 - 4\beta\delta(\alpha\gamma V_1^2 + \frac{m_{\mathrm{r}}a_{\mathrm{Drag}_y}}{k_{\mathrm{C}}}) > 0 \tag{5.17}$$

Solving for V_1 yields the final condition for the minimum follower voltage.

$$V_1^2 > \frac{4m_\mathrm{r}a_{\mathrm{Drag}_y}\beta\delta}{k_\mathrm{C}(\alpha\delta - \beta\gamma)^2} \tag{5.18}$$

Note here that, given the sign of the substituted variables indicated in Eq. (5.15), there is a minimum follower voltage for all possible configurations. Note that both V_1 and V_2 are solutions to quadratic equations, yielding 4 possible voltages to achieve the desired acceleration — two sets of equal magnitude and opposite sign. The fact that there are two sets of negative voltages that can generate the desired acceleration arises from the position-dependent nature of the system capacitance discussed previously. The larger (in magnitude) of the two same-signed potentials is a result of nearby objects pushing charge around such that the charge products — though not the charge vector itself, as degeneracy is not allowed for the non-singular charge-to-voltage mapping — are identical to those for the lower potential. The four sets are then: large positive V_1 and V_2, small positive V_1 and V_2, small negative V_1 and V_2, and large negative V_1 and V_2. The clear choice given the discussion in Chapter 3 is the use of small negative voltages, though the follower must adhere to Eq. (5.18). If this minimum voltage is likely to collapse the wake, wake shaping techniques must be applied so that larger voltages can be sourced.

5.2.2 Orbital Perturbations

While the control formulation incorporates linearized two-body gravity, drag, and Coulomb accelerations, the true simulated environment consists of nonlinear two-body and J_2 gravity, drag, and Solar Radiation Pressure (SRP) accelerations. For each spacecraft, the two-body gravitational acceleration is calculated given the gravitational constant of Earth μ and the position relative to the center of Earth $\boldsymbol{r}$. To incorporate the oblateness, the higher-order spherical harmonic term with coefficient J_2 is included which depends on the radius of the Earth r_Earth and the angle of the spacecraft position with respect to the $\hat{\boldsymbol{n}}_1 - \hat{\boldsymbol{n}}_2$ plane ϕ.

$$\boldsymbol{a}_\mathrm{G} = -\frac{\mu}{r^3}\boldsymbol{r} - \frac{3\mu r_\mathrm{Earth}^2}{2r^5}J_2\left[(1-5\sin^2\phi)\boldsymbol{r} + 2r\sin\phi\hat{\boldsymbol{n}}_3\right] \tag{5.19}$$

Cannonball drag and SRP models are used, as spherical craft are assumed in the scenario. The drag model used is shown below where A is the cross-sectional area, m the mass, C_{D} the drag coefficient, ρ_{atm} the local atmospheric density, and $\boldsymbol{v}_{\mathrm{rel}} = \dot{\boldsymbol{r}} - \boldsymbol{\omega} \times \boldsymbol{r}$ the atmosphere-relative velocity of a given craft assuming an atmosphere rotating at angular velocity $\boldsymbol{\omega}$. For this simulation, a corotating atmosphere is assumed rotating at earth's angular acceleration ($\boldsymbol{\omega}_{\mathrm{E}}$) such that $\boldsymbol{\omega} = \omega_{\mathrm{E}} \hat{\boldsymbol{h}}_{\mathrm{L}}$.

$$\boldsymbol{a}_{\mathrm{D}} = -\frac{1}{2} \frac{A C_{\mathrm{D}} \rho_{\mathrm{atm}}}{m} v_{\mathrm{rel}}^2 \hat{\boldsymbol{v}}_{\mathrm{rel}} \tag{5.20}$$

The model used for SRP is calculated

$$\boldsymbol{a}_{\mathrm{SRP}} = \frac{\Phi_{\mathrm{S}} C_{\mathrm{R}} A}{m} \frac{AU^2}{u^3} \boldsymbol{u} \tag{5.21}$$

where Φ_{S} is the solar flux at Earth, C_{R} is the reflectivity coefficient, AU is the astronomical unit, and $\boldsymbol{u}$ is the vector from the sun to a given spacecraft.

Finally, the total acceleration for each spacecraft is calculated for the environment model.

$$\boldsymbol{a} = \boldsymbol{a}_{\mathrm{C}} + \boldsymbol{a}_{\mathrm{G}} + \boldsymbol{a}_{\mathrm{D}} + \boldsymbol{a}_{\mathrm{SRP}} \tag{5.22}$$

5.3 Linear Quadratic Regulator (LQR) Voltage Controller

To investigate the robustness of the electrostatic actuation technique, a linearized subset of the environmental perturbations described above are included in the controller: namely two-body gravity, drag, and Coulomb accelerations. SRP and J_2 gravity are later included as an unmodeled perturbation. The control variable is chosen as the voltage vector calculated in Eq. (5.7).

For control development, it is convenient to put the system in state-space form so that the state is defined $\boldsymbol{X} = [\boldsymbol{\rho}, \boldsymbol{\rho}']^T$ and evolves according to the equation

$$\boldsymbol{X}' = \begin{bmatrix} \boldsymbol{\rho}' \\ \boldsymbol{\rho}''(\boldsymbol{X}, \boldsymbol{V}) \end{bmatrix} \tag{5.23}$$

where $\boldsymbol{\rho}''$ is the relative acceleration between the bodies observed in the HCW frame as discussed in Section 5.1. The control is derived in the HCW frame because leader-fixed points are constant in this frame, enabling the use of regulation control schemes. This has no effect on the control vector output as it is frame invariant. The description in terms of relative state necessitates that relative accelerations be used in the derivation. These are calculated

$$\delta \boldsymbol{a}_i = \boldsymbol{a}_{i_\mathrm{F}} - \boldsymbol{a}_{i_\mathrm{L}} \tag{5.24}$$

where i is an index over the relevant perturbations. The relative Coulomb acceleration is derived given that Newton's 3$^{\mathrm{rd}}$ law states that the these forces between the leader and follower are equal and opposite (i.e. $\boldsymbol{F}_{\mathrm{C_L}} = -\boldsymbol{F}_{\mathrm{C_F}}$).

$$\delta \boldsymbol{a}_\mathrm{C} = \frac{1}{m_\mathrm{F}} \boldsymbol{F}_{\mathrm{C_F}} - \frac{1}{m_\mathrm{L}} \boldsymbol{F}_{\mathrm{C_L}} = \frac{m_\mathrm{F} + m_\mathrm{L}}{m_\mathrm{F} m_\mathrm{L}} \boldsymbol{F}_{\mathrm{C_F}} = \frac{1}{m_\mathrm{r}} \boldsymbol{F}_{\mathrm{C_F}} \tag{5.25}$$

Here, the canonical reduced mass formula is recognized and denoted m_r.

5.3.1 Linearization of Equations of Motion

To apply linear control techniques, Eq. (5.23) must be linearized about some reference state and potential vector.

$$\boldsymbol{X}' \approx \boldsymbol{X}'(\boldsymbol{X}_0, \boldsymbol{V}_0) + \left.\frac{\partial \boldsymbol{X}'}{\partial \boldsymbol{X}}\right|_{\boldsymbol{X}_0} (\boldsymbol{X} - \boldsymbol{X}_0) + \left.\frac{\partial \boldsymbol{X}'}{\partial \boldsymbol{V}}\right|_{\boldsymbol{V}_0} (\boldsymbol{V} - \boldsymbol{V}_0) \tag{5.26}$$

The value $\boldsymbol{X}'(\boldsymbol{X}_0, \boldsymbol{V}_0)$ is the derivative of the state at the reference. Moving this term to the left side and using the Δ notation to indicate the difference between the variables and their reference values gives the familiar state-space form of the equations.

$$\Delta \boldsymbol{X}' = \left.\frac{\partial \boldsymbol{X}'}{\partial \boldsymbol{X}}\right|_{\boldsymbol{X}_0} \Delta \boldsymbol{X} + \left.\frac{\partial \boldsymbol{X}'}{\partial \boldsymbol{V}}\right|_{\boldsymbol{V}_0} \Delta \boldsymbol{V} \tag{5.27}$$

The general form of the expressions $\left.\frac{\partial \boldsymbol{X}'}{\partial \boldsymbol{X}}\right|_{\boldsymbol{X}_0}$ and $\left.\frac{\partial \boldsymbol{X}'}{\partial \boldsymbol{V}}\right|_{\boldsymbol{V}_0}$ are provided below in terms of the Jacobians of the state derivative with respect to the state and voltages, respectively.

$$\left.\frac{\partial \boldsymbol{X}'}{\partial \boldsymbol{X}}\right|_{\boldsymbol{X}_0} = [A] = \left.\begin{bmatrix} [0] & [I] \\ \frac{\partial \delta \boldsymbol{a}}{\partial \boldsymbol{\rho}} & \frac{\partial \delta \boldsymbol{a}}{\partial \boldsymbol{\rho}'} \end{bmatrix}\right|_{\boldsymbol{X}_0} \tag{5.28}$$

$$\left.\frac{\partial \boldsymbol{X}'}{\partial \boldsymbol{V}}\right|_{\boldsymbol{V}_0} = [B] = \left.\begin{bmatrix} [0] \\ \frac{\partial \delta \boldsymbol{a}}{\partial \boldsymbol{V}} \end{bmatrix}\right|_{\boldsymbol{V}_0} \tag{5.29}$$

The Jacobian of the Coulomb acceleration with respect to the state variable is complicated, as both the relative positions $\boldsymbol{r}_{1,i}$ and the capacitance matrix $[C]$ depend on the states as seen in Eqs. (5.5) and (5.7). The rotating-frame acceleration derivatives are incorporated later.

$$\frac{\partial \delta \boldsymbol{a}_{\mathrm{C}}}{\partial \boldsymbol{X}} = \frac{k_{\mathrm{C}}}{m_{\mathrm{r}}} \left\{ \left(\sum_{i=2}^{n} \frac{\boldsymbol{C}_i^T \boldsymbol{V}}{r_{1,i}^3} \boldsymbol{r}_{1,i} \right) \left(\boldsymbol{V}^T \frac{\partial \boldsymbol{C}_1}{\partial \boldsymbol{X}} \right) + \boldsymbol{C}_1^T \boldsymbol{V} \sum_{i=2}^{n} \left[\frac{\boldsymbol{r}_{1,i}}{r_{1,i}^3} \boldsymbol{V}^T \frac{\partial \boldsymbol{C}_i}{\partial \boldsymbol{X}} + \boldsymbol{r}_{1,i} \boldsymbol{C}_i^T \boldsymbol{V} \frac{\partial r_{1,i}^{-3}}{\partial \boldsymbol{X}} + \frac{\boldsymbol{C}_i^T \boldsymbol{V}}{r_{1,i}^3} \frac{\partial \boldsymbol{r}_{1,i}}{\partial \boldsymbol{X}} \right] \right\} \tag{5.30}$$

The derivative of the capacitance is necessarily a $n \times n \times 3$ tensor. Tensors of this shape are henceforth indicated with a double bar over the matrix, as shown in Eq (5.31). Additionally, the prime notation here is used to denote the derivative with respect to the state. The derivative of the capacitance can be calculated by relation to the elastance, for which a simple analytic expression (Eq. (5.7)) exists.

$$\overline{\overline{[C']}} = \frac{\partial [C]}{\partial \boldsymbol{X}} = -[C]\overline{\overline{[S']}}[C] \tag{5.31}$$

Consider the elastance derivative as a set of $1 \times 1 \times 3$ vectors stacked in to the rows and columns of the elastance derivative. The derivative of the diagonal elements elastance with respect to the state $\boldsymbol{S}'_{ii}$ are the zero vector, as these depend only on the MSM sphere radii which state-independent. The same is true of the sub-matrix $\frac{\mathrm{d}[S]}{\mathrm{d}\boldsymbol{\rho}'}$, as the relative distances are independent of the follower's HCW velocity. The off-diagonal HCW position derivative elements $\boldsymbol{S}'_{ij}$ all have the same form.

$$\boldsymbol{S}'_{ij} = \frac{\mathrm{d}S_{ij}}{\mathrm{d}\boldsymbol{\rho}} = \frac{\mathrm{d}(\boldsymbol{r}_{ij}^T \boldsymbol{r}_{ij})^{-1/2}}{\mathrm{d}\boldsymbol{r}_{\mathrm{F}} - \boldsymbol{r}_{\mathrm{L}}} = \frac{\mathrm{d}(\boldsymbol{r}_{ij}^T \boldsymbol{r}_{ij})^{-1/2}}{\mathrm{d}\boldsymbol{r}_1} - \frac{\mathrm{d}(\boldsymbol{r}_{ij}^T \boldsymbol{r}_{ij})^{-1/2}}{\mathrm{d}\boldsymbol{r}_{\mathrm{L}}} = \frac{\mathrm{d}(\boldsymbol{r}_{ij}^T \boldsymbol{r}_{ij})^{-1/2}}{\mathrm{d}\boldsymbol{r}_1} \tag{5.32}$$

Note that the charge structure sphere positions are fixed with respect to the leader craft, hence the vanishing of the second term in the derivative. Additionally, only the first row and column of the elastance matrix depend on the follower voltage, so the equation can be further simplified.

$$\boldsymbol{S}'_{1j} = -\boldsymbol{r}'^{T}_{1j}\frac{\boldsymbol{r}_{1j}}{r^3_{1j}} = \frac{\mathrm{d}(\boldsymbol{r}_1 - \boldsymbol{r}_j)^T}{\mathrm{d}\boldsymbol{r}_1}\frac{\boldsymbol{r}_{1j}}{r^3_{1j}} = \frac{\boldsymbol{r}_{1j}}{r^3_{1j}} \tag{5.33}$$

The capacitance derivative with respect to the state can now be calculated using equations Eqs (5.31) - (5.33). Similar to the usage of capacitance vectors previously, the sub-matrices of the capacitance derivative are denoted $[C'_i]$ henceforth. The derivative of the relative Coulomb acceleration with respect to the state is simplified relative to Eq. (5.30) using this notation.

$$\frac{\partial \delta \boldsymbol{a}_{\mathrm{C}}}{\partial \boldsymbol{X}} = \frac{k_{\mathrm{C}}}{m_{\mathrm{r}}}\left\{\left(\sum_{i=2}^{n}\frac{\boldsymbol{C}_i^T\boldsymbol{V}}{r^3_{1,i}}\boldsymbol{r}_{1,i}\right)\boldsymbol{V}^T[C'_1] + \left(\boldsymbol{C}_1^T\boldsymbol{V}\right)\sum_{i=2}^{n}\frac{\boldsymbol{r}_{1,i}\boldsymbol{V}^T[C'_i] + \boldsymbol{C}_i^T\boldsymbol{V}([I] - 3\boldsymbol{r}_{1,i}\boldsymbol{r}^T_{1,i})}{r^3_{1,i}}\right\} \tag{5.34}$$

The Jacobian of the Coulomb acceleration with respect to the control variable — the voltages on the follower and charge structure — is more straightforward, as the capacitance does not depend on this variable.

$$\frac{\partial \delta \boldsymbol{a}_{\mathrm{C}}}{\partial \boldsymbol{V}} = \frac{k_{\mathrm{C}}}{m_{\mathrm{r}}}\left\{\left(\sum_{i=2}^{n}\frac{\boldsymbol{C}_i^T\boldsymbol{V}}{r^3_{1,i}}\boldsymbol{r}_{1,i}\right)\boldsymbol{C}_1^T + \left(\boldsymbol{C}_1^T\boldsymbol{V}\right)\sum_{i=2}^{n}\frac{\boldsymbol{r}_{1,i}\boldsymbol{C}_i^T}{r^3_{1,i}}\right\} \tag{5.35}$$

The matrices in Eqs. (5.34) and (5.35) are evaluated at the nominal follower position and potential vector, respectively, to obtain the linearized Coulomb dynamics and control in state space form as shown in Eq. (5.27). For the on-orbit scenario described previously, additional dynamics are present from relative orbital motion with drag. Under the assumptions of a circular leader orbit and nearby follower orbit, the formulation of the HCW equations with linearized drag forces presented first by Silva [83] and modified by Harris [33] is applied. These equations of motion typically include a secular differential drag acceleration which in this case is assumed to be canceled by the Coulomb repulsion between the leader and follower. The along-track differential drag acceleration magnitude a_{Drag_y} required to calculate the nominal system potentials discussed in and around Eq. (5.14) calculated by reference [33] is repeated here. An important assumption is made at this step — the atmospheric density in the wake is considered null ($\rho_{\text{atm}_\text{F}} = 0$). At this altitude, the rarefied atmosphere is likely to be perturbed more than the ions, so this assumption is reasonable.

$$a_{\text{Drag}_y} = \frac{1}{2} n_\text{L}^2 r_\text{L}^2 (\beta_\text{L} \rho_{\text{atm}_\text{L}} - \beta_\text{F} \rho_{\text{atm}_\text{F}}) = \frac{1}{2} n_\text{L}^2 r_\text{L}^2 \beta_\text{L} \rho_{\text{atm}_\text{L}} \tag{5.36}$$

Here, n_L is the leader craft mean motion and $\beta = {}^{AC_D}/_{m}$ is the ballistic coefficient of a spacecraft.

Using these assumptions, the full system dynamics are produced by summing the state dynamics matrices of the HCW-plus-drag and Coulomb perturbed systems. The state dynamics and control sensitivity matrices are defined.

$$[A] = [A_{\text{HCW+Drag}}] + \begin{bmatrix} [0] & [I] \\ \frac{\partial \delta \boldsymbol{a}_\text{C}}{\partial \boldsymbol{\rho}} & [0] \end{bmatrix} \Bigg|_{\boldsymbol{X}_0} \tag{5.37}$$

$$[B] = \begin{bmatrix} [0] \\ \frac{\partial \delta \boldsymbol{a}_\text{C}}{\partial \boldsymbol{V}} \end{bmatrix} \Bigg|_{\boldsymbol{V}_0} \tag{5.38}$$

Note that the rotating-frame accelerations are accounted for in $[A_{\text{HCW+Drag}}]$. Recall in the equations above that the controller does not include SRP accelerations.

5.3.2 Control Law

A Linear Quadratic Regulator (LQR) controller is implemented on the system described. Control voltages $\boldsymbol{u}$ are sourced proportional to the deviation from the nominal state $\Delta \boldsymbol{X}$. The control law is presented without derivation, as it is commonly known.

$$\boldsymbol{u} = [\mathcal{R}]^{-1} [B]^T [\mathcal{P}] \Delta \boldsymbol{X} = -[K] \Delta \boldsymbol{X} \tag{5.39}$$

Above, $[\mathcal{R}]$ is the control gain matrix and $[\mathcal{P}]$ is a solution to the algebraic Ricatti equation which incorporates the state feedback gain $[\mathcal{Q}]$ as well as $[A]$ and $[B]$. The gains $[\mathcal{R}]$ and $[\mathcal{Q}]$ are tuned by trial and error to achieve a desired balance of state deviation and control usage.

5.3.3 Linear Controllability

Prior to examining linear controllability, the passive dynamics of the system are examined through eigenvalue analysis. The uncontrolled system is not stable — despite the potential well structure of the leader craft's electric field — as some of its poles exhibit positive real components. The control development described previously is specifically designed to yield stable linear closed-loop dynamics and indeed, all eigenvalues of $([A]-[B][K])$ have explicitly negative real components. It should be noted that this stability only holds as long as the linearization is valid, so large departures from the nominal state and control variables could result in instability.

Linear controllability can be readily established using the linearized equations of motion by analyzing the column and null space of the controllability matrix M.

$$M = \begin{bmatrix} B & AB & A^2B & ... & A^nB \end{bmatrix} \tag{5.40}$$

Prior work on Coulomb-tethered spacecraft [64] and Coulomb-controlled formation flight [45] has suggested several results for this system's controllability.

In a minimal sense, only the in-plane (HCW X-Y) states are found to be controllable with a single sphere on the leader spacecraft. While a single sphere could in theory produce only positive or negative accelerations in the HCW Y direction, controllability is achieved due to in-plane coupling in the HCW equations. Fundamentally, this result grounds the following results by replicating the controllability results found by Natarajan [63, 65] with respect to a two-sphere formation actuated only by Coulomb attraction. Notably, due to the assumption of two-body motion, the out-of-plane mode is marginally stable and will remain bounded.

Out-of-plane controllability is achieved with the addition of a second sphere. Consider a charge structure similar to that in Figure 5.1, but with only two spheres. Because the system has been linearized about an in-plane equilibrium, full controllability could not be achieved if the charge structure is arranged in-plane, i.e. along the HCW X axis. However, a line of charged spheres along the out-of-plane axis (HCW Z) yields full controllability in the position and velocity states, as the r_i states gain a component along the out-of-plane axis. These results are summarized in Table 5.1. Controllability is not affected by the addition of more spheres — assuming the circular charge structure geometry in Figure 5.1 — so only the 1 and 2 sphere cases are considered.

Table 5.1: Minimal controllability summary

Arrangement	Controllable Eigenvectors
Single sphere	In-Plane directions
Two Spheres, In-Plane	In-Plane directions
Two Spheres, Out-of-Plane	All directions

An additional limit on controllability is established by Eq.(5.18). If this condition is not met, the along-track drag acceleration cannot be balanced and the control cannot stabilize the system.

5.3.4 Control Sensitivity

With the linear controllability of the system established, it is necessary to further examine the sensitivity of prospective controllers to the selection of multiple system parameters. A major concern with this approach is the validity of the linearization under large control voltages. As such, the selection of system parameters should minimize the control voltage requested by the controller. In an equivalent sense, it is desirable for changes from the reference voltage to have a large impact on the system's states. For a linear system, the impact of these parameters is governed by the control effect matrix B. For systems that satisfy the necessary conditions for controllability derived in Section 5.3.3, the Frobenius norm of B is used as an index of control sensitivity with respect to parameter variation. This norm is chosen because it provides an indication of the size of accelerations generated by a set of control voltages.

$$\text{norm}([B]) = \sqrt{\sum_{i=1}^{m}\sum_{j=1}^{n}|B_{ij}|^2} \tag{5.41}$$

The sensitivity of B with respect to the follower voltage V_f and the number of spheres constituting the charge structure n_{cs} was evaluated for a range of plausible values of n_{cs} and V_f, resulting in Figure 5.2. The norm of B scales log-logarithmically as V_f increases, as each sphere carries a larger voltage under nominal conditions. At the same time, the norm of B drops as the number of spheres increases, reflecting the fact that attractive and repulsive forces between spheres — which requires forcing same-signed charge onto conducting spheres — requires a large voltage. These results show that the norm of B is largest when the charge structure consists of only a handful of spheres and the follower maintains a relatively large voltage.

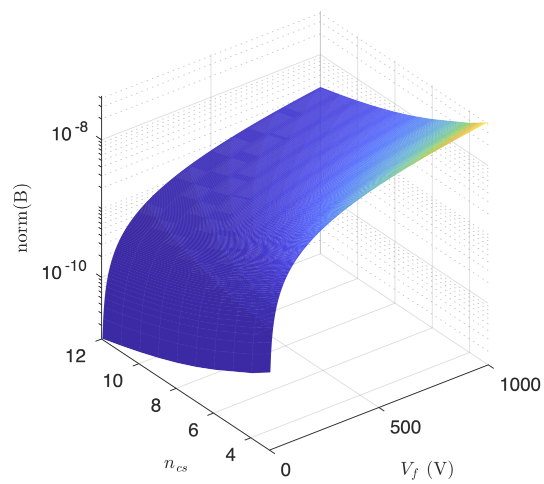

Figure 5.2: norm($[B]$) variation with respect to n and V_{f}.

Using $n_{\mathrm{cs}} = 2$ and $V_{\mathrm{f}} = 1000V$, the sensitivity of norm($[B]$) was investigated with respect to the charge structure radius (R_{cs}), and the radii scale $R_{\mathrm{s}}/R_{\mathrm{cs}}$, which is constrained to be less that 1 such that no spheres have overlapping volumes as mentioned previously. These results are shown in Figure 5.3. Here, it is apparent that the norm of $[B]$ increases with both the charge structure radius and the radii of the spheres constituting the charge structure. As the charge structure radius increases, additional control authority is achieved by the larger components of the forces resulting from each sphere along axes other than the HCW Y direction. Similarly, as the sphere radii increase, the electric field generated by each sphere for a given voltage increases in magnitude, resulting in larger forces on the follower.

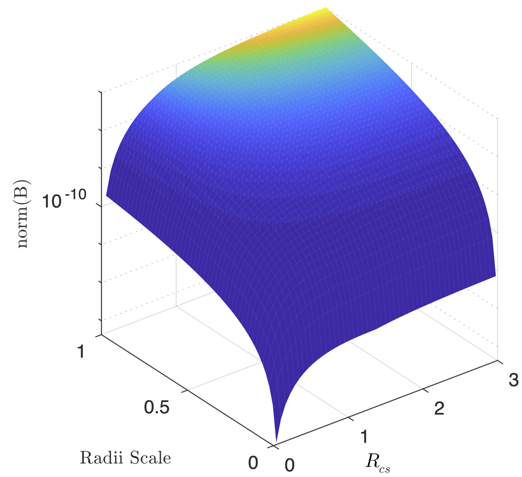

Figure 5.3: norm($[B]$) variation with respect to the charge structure radius R_{cs} and radii scale $R_{\text{s}}/R_{\text{cs}}$

From these sweeps, it is apparent that a system designed for maximized control effectiveness will use the largest feasible charge structure radius (R_{cs}), sphere radii (R_{s}), and follower voltage while minimizing the number of spheres used. As discussed previously, instances of in-wake charging of up to -6 kV have been observed in LEO. [31] However, large voltages may require extremely large power if the wake collapses. The case of the Space Shuttle charging used many Watts of power (the wake likely collapsed) which is not feasible for the electrostatic actuation system. On the other hand, the pusher-only control technique motivated by the asymmetric shielding in the wake [27] demands that only negative voltages are sourced. The nominal follower voltage of -1000 V fit both criterion for the simulations to follow.

Another concern discussed previously is that arcing and other charging effects occur if $R_{\text{s}} \approx R_{\text{cs}}$, so R_{s} is chosen such that the two charged spheres will be separated by 1 meter — a sufficient distance to mitigate the likelihood of arcing at LEO densities, though calculation of this distance requires detailed knowledge of the plasma in the wake.

Table 5.2: Maximum Control Norm Design Parameters

Parameter	Value
V_{f}	-1000V
n_{cs}	2
R_{cs}	3m
R_{s}	2.5m

5.3.5 LQR Simulation Results

Simulations are performed applying the linear control law derived above to the nonlinear dynamics in two different cases. The controller is run at 0.2 Hz and control gains are chosen such that the system settles within ∼45 minutes (0.5 orbits). The orbit elements — given in order, semi-major axis, eccentricity, inclination, right ascension, argument of periapsis, and true anomaly — of the leader are $[7000\text{km}, 0, 0°, 0°, 20°, 0°]^T$. The relative drag and SRP perturbations are similar in magnitude at this altitude. Therefore, this orbit provides a good test of robustness for the controller, which does not include SRP dynamics. A nominal separation distance of 1 m in the along-track direction is chosen to fit the requirements of a DCPA mission.

For direct comparison with the discussion immediately above, an initial simulation is performed applying the parameters outlined in Table 5.2. Additionally, perfect knowledge of the follower craft's HCW position is assumed as is the ability to perfectly source voltage on each sphere. These parameters and assumptions will be changed in later simulations. The mass of the leader is large compared with the follower such that the equal and opposite Coulomb force generated by the voltages on the follower and charge structure results in a small leader acceleration. The performance of the control is considered for a case in which the follower is offset from the nominal position — about which the linearization is performed — by 1 cm in the along-track direction.

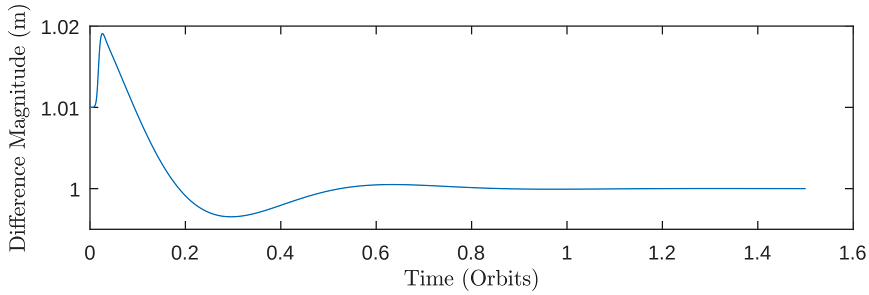

Figure 5.4: HCW-frame follower position magnitude for perfect feedback system

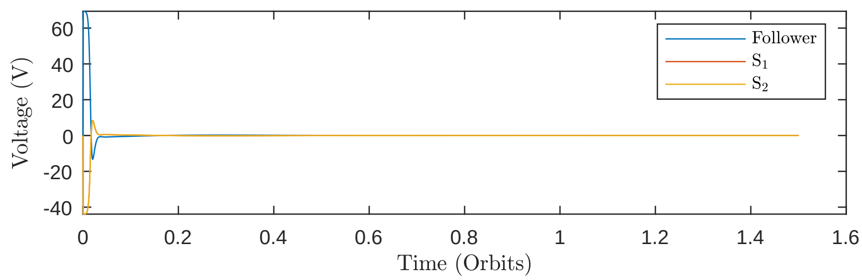

Figure 5.5: Deviation of system voltages from nominal. The curve for S_2 is superimposed on the identical curve for S_1.

Note that the signature of the plot in Figure 5.4 resembles the step response of a forced, damped harmonic oscillator. The linearized equations of motions within the controller shown in Eqs. (5.29), (5.37), and (5.38) bear out this behavior as a step function in follower position is applied. The initial increase in separation distance before the control settles to the nominal value results because only two spheres are used in the charge structure. Table 5.1 indicates that two spheres placed symmetrically out of plane results in a fully controllable system, but this is due to the coupling in the HCW X and Y directions. This is illustrated in Figure 5.6, which shows the offset from nominal for each of the HCW directions.

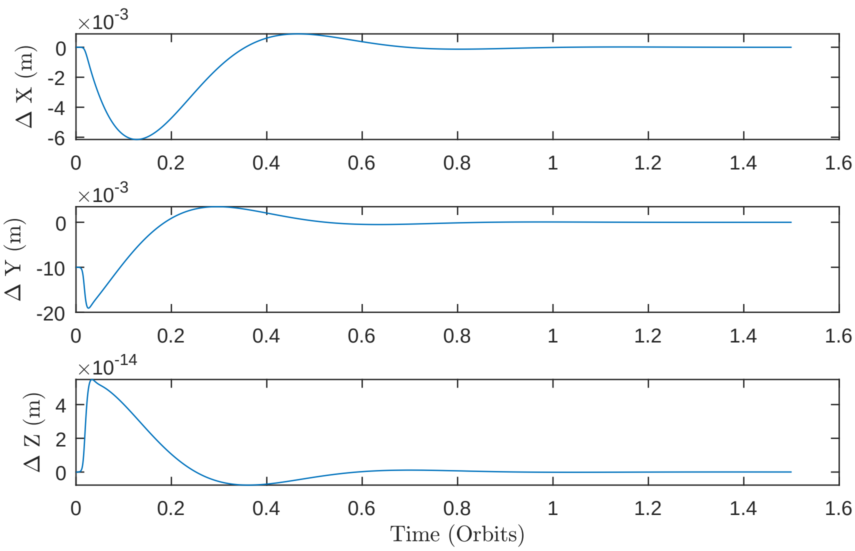

Figure 5.6: HCW vector component differences

If the controller simply pulled the sphere in the along-track direction, some radial change would occur. Two spheres out of plane cannot generate an electric field to fully control in this direction — only with the HCW dynamics is the system fully controllable. By leveraging the system dynamics, and specifically the known in-plane coupling exhibited by the HCW equations, the system is able to stabilize with the help of the controller. The control voltages in Figure 5.5 shows the deviation from the nominal voltages for the follower and for spheres 1 and 2 on the charge structure denoted as S_1 and S_2, respectively. Note that the line for S_1 cannot be seen because identical voltages are commanded on the two leader-craft spheres. The maximum deviation from the nominal voltage for this case (∼60 V) is small, resulting in a linearization error of roughly 5% in the Coulomb force acceleration magnitude. This error in the controller is not corrected in simulations.

While the simulation above demonstrates the effectiveness of the control given parameters that enhance controllability, the values in Table 5.2 and the assumptions state above do not fit a realistic mission scenario. The parameters in Table 5.3 are used in the simulation to follow which as before attempts to regulate the follower at a 1 m separation in the anti-alongtrack direction.

They are chosen to be commensurate with the dimensions of the leader shown in Table 5.4. After running simulations, the number of spheres in the charge structure on the leader was increased to improve the system settling behavior as noise and unmodeled perturbations are included in this latter case. The additional sphere enables full controllability with only the Coulomb force, enabling direct control to counter any off-axis perturbations.

Table 5.3: Mission Scenario Design Parameters

Parameter	Value
V_{f}	-1000V
n_{cs}	3
R_{cs}	0.3m
R_{s}	0.25m

The size and mass of the leader craft were based roughly on the Iridium spacecraft to provide a reasonable baseline for a LEO mission. The follower is assumed to be a spherical craft small enough to fit within the wake of the leader. To simulate the effects of the wake on atmospheric drag, the drag coefficient of the follower is nulled.

Table 5.4: System Physical Parameters

Parameter	Leader	Follower
Area (m^2)	0.5	0.008
Mass (kg)	1000	1
Coefficient of Reflectivity	1	1
Coefficient of Drag	2.2	0

The previous assumption that the follower position is known perfectly is relaxed. White Gaussian noise of $\sigma_r = 10^{-3}$ m , $\sigma_v = 10^{-5}$ m/s is added to the range value input to the controller. These noise values were chosen such that all of the controllers discussed henceforth are able to converge. Scaling these noise values by even a factor of 2 or 3 can result in system instability due to nonlinearities in the system or consequences of control design as discussed later. To account for noise in the system, a simple averaging filter is applied, running at a lower frequency than the measurements are coming in. Ten range measurements are averaged while the control voltages are held constant. Important to note here is the consideration only of random noise in the state.

Other noise sources would exist on orbit such as thermal drift in sensors. The effect of these errors would be mitigated — but not eliminated — through application of a Kalman filter or other orbit estimation technique. Such navigation methods are considered out of scope for this dissertation, so only the random noise indicated is considered.

Error is not included on voltages sourced by the system. As discussed in Chapter 4, charging of spacecraft in orbit requires that current balance be influenced to achieve a desired potential. One method for achieving this is plasma beam emission. Specification for ion and electron guns flown on past LEO missions are not available, however modern plasma guns for terrestrial use can hold the energy of a charged particle beam to within 1 eV or better. (P. Loeffler, personal communication, July 17, 2020) This small voltage difference results in a 0.1% error in the Coulomb acceleration for the electrostatic actuation system described in Figure 5.1 and Table 5.3 — this minor error will result in a very small state bias and would therefore not compromise the controllers described. It is assumed that plasma sources for use in space could achieve a similar accuracy and so noise on the control variable is neglected.

Solar Radiation Pressure (SRP) is included as an unmodeled perturbation. Both drag and SRP vary as they pass in and out of sunlight. Drag is varied sinusoidally by ±30% to roughly reflect density changes between sun and eclipse [18], while SRP is cut completely in shade. These simplified models are described in greater detail in Table 5.5 where ν is the true anomaly. A clear distinction is made between the controller dynamics and simulated environment.

Table 5.5: SRP and Drag Models in Simulation

	Drag	SRP
Controller	$\rho_{\text{atm}} = \rho_{\text{atm},0}$	$C_{\text{R}} = 0$
Environment	$\rho_{\text{atm}} = \rho_{\text{atm},0}(1 + 0.3\sin(\nu))$	$C_{\text{R}} = \begin{cases} C_{\text{R}} & 0 \leq \nu < \pi \\ 0 & \pi \leq \nu < 2\pi \end{cases}$

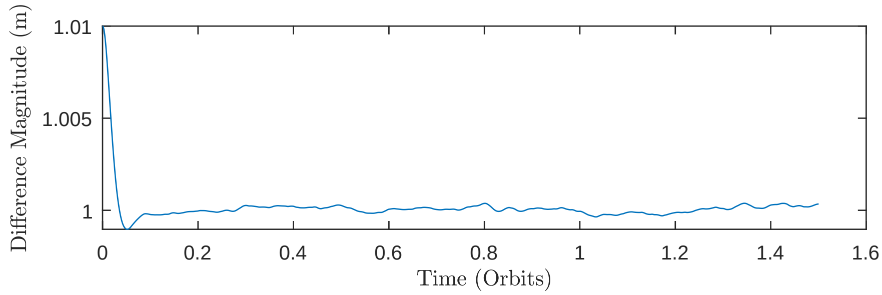

Figure 5.7: HCW-frame follower position magnitude

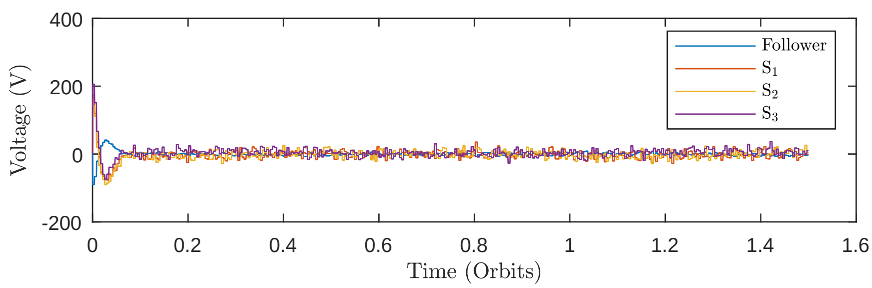

Figure 5.8: Deviation of system voltages from nominal

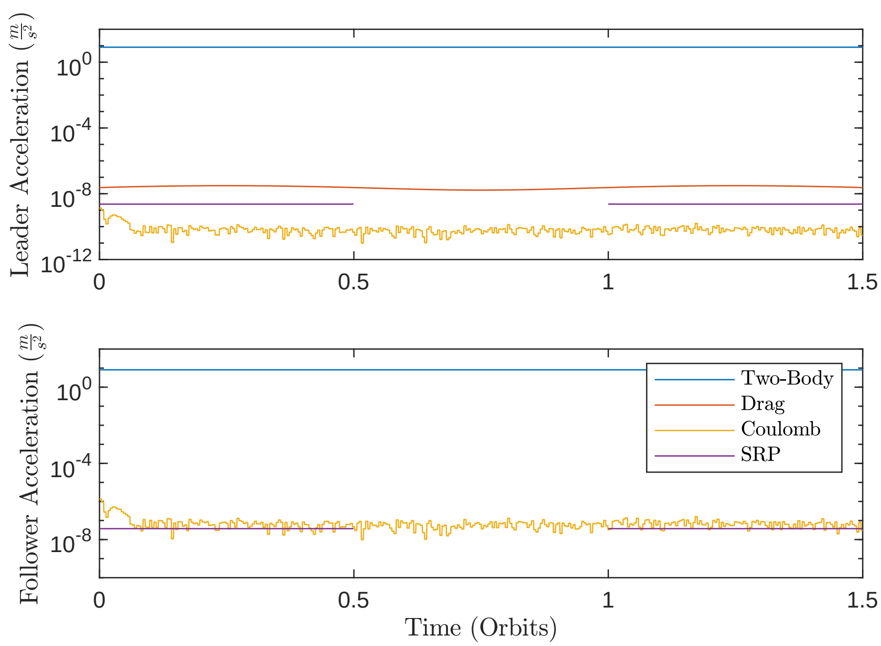

Figure 5.9: Drag, Coulomb, and SRP accelerations on the leader and follower crafts

Finally, the simulation is initialized with a 1 cm offset in the HCW Y direction as before. Figure 5.7 shows the control performance of the system. With unmodeled accelerations and noisy range measurements, the system remains within ~ 1 mm of the nominal position after the initial 1 cm offset is corrected. The ability of the control to remain exactly at this location is compromised, however it does stay extremely close — well within the sub-centimeter accuracy required by DPCA.

Figure 5.8 shows the deviation of system voltage from the nominal sourced at a given time step. The nominal follower voltage of -1 kV is indicated in Table 5.3, meaning that the maximum system voltage is roughly -1.1 kV. The results presented in Chapter 3 indicate this would require a leader craft diameter of at least ~ 3 m. The charge structure radius of 0.3 m would fit in the wake, though the obvious lack of craft of this size in LEO is a challenge. Wake shaping techniques could potentially solve this problem as discussed in Chapter 3.

The pusher-only control described in previous sections is sufficient, as no positive voltages are sourced. Nascap-2k simulations described in Chapter 3 indicate that this control would require very little power, as no positive voltages were sourced and the wake is unlikely to collapse for the simulation parameters.

Note that the voltages sourced by the controller in this latter simulation are much large than those in the previous simulation. This results primarily from the addition of noise on the follower position. As indicated previously, a very large voltage must be sourced to generate a very small relative acceleration. Therefore, even the relatively small position and velocity errors incurred from incorporating noise in the system generate a very large control response. The previous case's controller was not met with any unmodeled perturbations and therefore experiences more consistent, smaller state errors.

Note that the drag acceleration dominates the Coulomb acceleration for the leader craft. This is because the equal and opposite Coulomb force produces a much smaller acceleration due to the large mass of the leader.

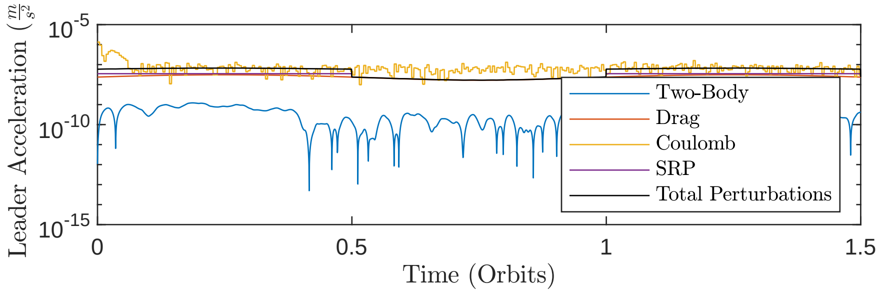

Figure 5.10: Relative accelerations between the leader and follower crafts. The sum of the gravity, drag, and SRP relative accelerations is shown in black for reference

The relative accelerations between the leader and follower are displayed in Figure 5.10. Note here that, once the system has settled, the relative Coulomb acceleration remains similar to the total perturbation magnitude — the sum of the gravitational, drag, and SRP relative accelerations — when in the sun, but does not decrease with the total perturbation magnitude as the spacecraft pass into shade. This is because the controller is still correcting on the noise added to the system. Additionally, the SRP direction changes during sunlit portions of the orbit, meaning that errors in the state are less apparent.

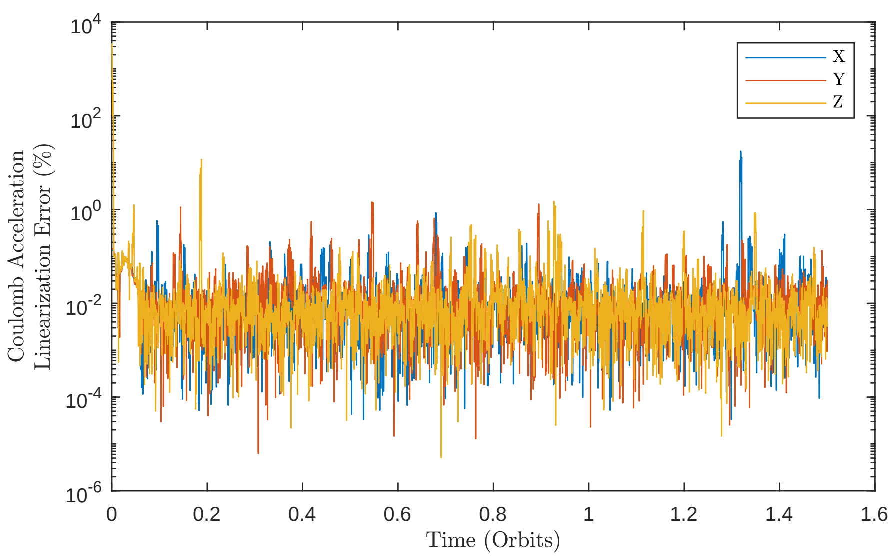

Figure 5.11: Coulomb acceleration linearization error

Figure 5.11 shows the linearization error in the Coulomb acceleration over the simulation duration. The linearized acceleration was calculated using Eqs. (5.34) and (5.35) and the state and voltage offsets at a given timestep, while the nonlinear acceleration is calculated directly with Eq. (5.12). These errors are bounded within about $\pm 20\%$, though at most times it is much smaller than this. However, for larger initial condition offsets, these errors grew large enough that the controller could not stabilize the system. This results from the fact identified in Chapter 2 that, unlike with most actuators, the control authority of the electrostatic actuation technique drops off as the inverse square of the relative distance. The linear controller cannot account for this nonlinear behavior, unpredictably resulting in instability for different sets of system gains, initial conditions, reference trajectories, orbits, and many other parameters. To provide context, an initial offset of 6 cm results in system instability given the parameters in the second simulation.

5.3.6 LQR Voltage Control Simulation Conclusions

The LQR voltage controller is able to settle the system described in Section 5.1 using a maximum voltage of 1.2 kV. Given the system definition, Nascap-2k simulations outlined in Chapter 3 indicate wake collapse is unlikely to occur. Coupled with the fact that only negative voltages are sourced, the regulating control described above is predicted to be extremely power efficient. The linearization of the Coulomb acceleration holds well throughout the simulations, but is not robust to large initial offsets and noise. The system is particularly nonlinear in the control variable which — given discussion of large voltages generating small control — is the main reason for the extremely tight bounds on position offsets. This motivates the development of alternate control methods that better handle the system's nonlinearities and that allow larger state offsets.

To develop the LQR controller, the system had to be linearized both in the state and control variables, yielding the canonical state dynamics and control effects matrices. No choice of state will result in a naturally linear Coulomb acceleration (i.e. the Jacobian of the Coulomb acceleration is state-independent), but this is not true of the control, which can be chosen freely. The Coulomb acceleration is naturally linear in the charge products, indicating large control deviations will not cause linearization errors.

5.4 Charge-Product Control Formulation

Due to the complications cited above, a charge-product control variable was considered. First introduced by [64], it uses a control vector $\boldsymbol{U}$ of charge products $U_i = Q_1 Q_i$. The key benefits of this formulation is that the Coulomb acceleration is linear in this variable and the voltage-to-charge relationship can be computed directly via Eq. (5.8), thus requiring no inverse. Recall that the follower craft is modeled with a single MSM sphere, while the charge structure is modeled with n_{cs}. The charge on an individual sphere given the voltage vector is

$$Q_i = \boldsymbol{C}_i^T \boldsymbol{V} \tag{5.42}$$

This fact is applied to Eq. (5.11) to yield an expression for the electric field in terms of the charges on the charge structure spheres.

$$\boldsymbol{E}_{\mathrm{L}} = \sum_{i=2}^{n} \frac{Q_i}{r_{1,i}^3} \boldsymbol{r}_{1,i} \tag{5.43}$$

Substituting the follower charge and leader electric field equations, the Coulomb acceleration on the follower craft is calculated.

$$\boldsymbol{a}_{\mathrm{C}}(\boldsymbol{X}, \boldsymbol{Q}) = \frac{k_{\mathrm{C}} Q_1}{m_{\mathrm{F}}} \sum_{i=2}^{n} \frac{Q_i}{r_{1,i}^3} \boldsymbol{r}_{1,i} = \frac{k_{\mathrm{C}}}{m_{\mathrm{F}}} \sum_{i=2}^{n} \frac{U_i}{r_{1,i}^3} \boldsymbol{r}_{1,i} \tag{5.44}$$

The summation notation in replaced with matrix-vector notation given the definition $[r] = [\boldsymbol{r}_{1,2}/r_{1,2}^3, \boldsymbol{r}_{1,3}/r_{1,3}^3, ..., \boldsymbol{r}_{1,n}/r_{1,n}^3]$.

$$\boldsymbol{a}_{\mathrm{C}}(\boldsymbol{X}, \boldsymbol{Q}) = \frac{k_{\mathrm{C}}}{m_{\mathrm{F}}} [r] \boldsymbol{U} \tag{5.45}$$

Finally, the relative Coulomb acceleration is written in terms of charge by substituting the reduced mass for the follower mass.

$$\delta \boldsymbol{a}_{\mathrm{C}}(\boldsymbol{X}, \boldsymbol{U}) = \frac{k_{\mathrm{C}}}{m_{\mathrm{r}}} [r] \boldsymbol{U} = [\mathcal{B}_Q] \boldsymbol{U} \tag{5.46}$$

This is the classic linear form and the control effects matrix — or at least the bottom block matrix relating the control vector to the acceleration — naturally appears.

5.4.1 Jacobians

The primary contribution of this work is the application of the electrostatic actuation system, so the Jacobian of the relative Coulomb acceleration with respect to the follower position is detailed. The quantity $\boldsymbol{r}_{1,i} = \boldsymbol{\rho} - \boldsymbol{r}_i$, so its derivative with respect to the follower position is the identity matrix. Consider the derivative of Eq. (5.46) with respect to the follower position. The summation notation is applied, as taking the derivative of the matrix vector equation would generate rank 3 tensors difficult to work with.

$$\left[\frac{\partial \delta \boldsymbol{a}_{\mathrm{C}}}{\partial \boldsymbol{\rho}}\right] = \frac{k_{\mathrm{C}}}{m_{\mathrm{r}}} \sum_i U_i \left(\boldsymbol{r} \frac{\mathrm{d}}{\mathrm{d}\boldsymbol{\rho}} \left(r_{1,i}^{-3}\right) + r_{1,i}^{-3} \frac{\mathrm{d}}{\mathrm{d}\boldsymbol{\rho}} (\boldsymbol{r}_{1,i})\right) \tag{5.47}$$

The derivative of $r_{1,i}^{-3}$ can be simplified by considering it in terms of a vector inner product.

$$\frac{\mathrm{d}}{\mathrm{d}\boldsymbol{\rho}} \left(r_{1,i}^{-3}\right) = \frac{\mathrm{d}}{\mathrm{d}\boldsymbol{\rho}} \left(\boldsymbol{r}_{1,i}^T \boldsymbol{r}_{1,i}\right)^{-3/2} = -\frac{3}{2} r_{1,i}^{-5} \left(\boldsymbol{r}_{1,i}^T [I] + \boldsymbol{r}_{1,i}^T [I]\right) = -\frac{3}{r_{1,i}^5} \boldsymbol{r}_{1,i}^T \tag{5.48}$$

Plugging into Eq. (5.47) yields the linearized Coulomb acceleration for charge products.

$$\left[\frac{\partial \delta \boldsymbol{a}_{\mathrm{C}}}{\partial \boldsymbol{\rho}}\right] = \frac{k_{\mathrm{C}}}{m_{\mathrm{r}}} \sum_{i=2}^{n} \frac{U_i}{r_{1,i}^3} ([I] - 3 \hat{\boldsymbol{r}}_{1,i} \hat{\boldsymbol{r}}_{1,i}^T) \tag{5.49}$$

The Jacobian of the relative Coulomb acceleration with respect to the control is trivial given the linearity demonstrated in Eq. (5.46).

$$\left[\frac{\partial \delta \boldsymbol{a}_{\mathrm{C}}}{\partial \boldsymbol{U}}\right] = [\mathcal{B}_Q] \tag{5.50}$$

The full form of $[A(\boldsymbol{Q})]$ is the same as $[A(\boldsymbol{V})]$ though substitutes the alternate expression for $[\partial \delta \boldsymbol{a}_{\mathrm{C}} / \partial \boldsymbol{\rho}]$. While the two expressions for the Jacobian of the Coulomb acceleration with respect to position — Eqs. (5.34) and (5.49) — are equivalent, a major benefit of the charge-product control is that no derivatives of the capacitance need be taken. Additionally, the control effect matrix $[B_Q]$ is linear in the control, so the linearization concerns of the voltage control approach are irrelevant.

The control vector $\boldsymbol{U}$ in this formulation gives a set of $Q_1 Q_i$ for which there are infinitely many combination of Q_1 and Q_i. Therefore, the charge Q_1 is chosen based on mission specific concerns and the resulting Q_i are calculated so as to fully populate $\boldsymbol{Q}$. The voltage-to-charge relationship yields the voltages necessary to source the calculated charges — again, without the need for a matrix inverse.

5.4.2 Relative Environmental Perturbations

The environmental accelerations defined in Section 5.2 pertain to each craft individually. However, the controllers derived in later sections are defined based on the inertial relative dynamics between the leader and follower craft. The follower gravity and drag accelerations relative to the leader are written. Recall that the controller includes only two-body gravity, while the simulation perturbations include the J_2 term.

$$\delta \boldsymbol{a}_{\mathrm{D}} = -\frac{1}{2}\left(\beta_{\mathrm{F}}\rho_{\mathrm{atm}_{\mathrm{F}}} - \beta_{\mathrm{L}}\rho_{\mathrm{atm}_{\mathrm{L}}}\right) v_r \boldsymbol{v}_r \tag{5.51}$$

$$\delta \boldsymbol{a}_{\mathrm{G}} = -\mu\left(\frac{\boldsymbol{r}_{\mathrm{F}}}{r_{\mathrm{F}}^3} - \frac{\boldsymbol{r}_{\mathrm{L}}}{r_{\mathrm{L}}^3}\right) \tag{5.52}$$

Note above that it is assumed that the atmosphere-relative velocities are identical between the two craft. Given that the differences in ballistic coefficient and local density dominate the differential drag term for such close-proximity craft, this is a reasonable assumption. A similar assumption that $\boldsymbol{r}_{\mathrm{F}} = \boldsymbol{r}_{\mathrm{L}}$ cannot be made in the gravity case, as differential two-body gravitational accelerations arise only from the difference in these positions.

Finally, the total inertial acceleration of the follower craft relative to the leader is the sum of the Coulomb, gravitational, and drag acceleration differences between the two craft.

$$\ddot{\boldsymbol{\rho}} = \delta \boldsymbol{a}_{\mathrm{C}} + \delta \boldsymbol{a}_{\mathrm{D}} + \delta \boldsymbol{a}_{\mathrm{G}} \tag{5.53}$$

With the equations of motion modified for charge product control, two different controllers are derived to stabilize formation dynamics.

5.5 Linear Quadratic Tracking (LQT) Charge Product Controller

The first charge product controller applied to the electrostatic actuation problem employs optimal control techniques for a deployment scenario. The limited size of the plasma wake in which electrostatic actuation is possible motivates the implementation of a tracking formulation in which the follower is controlled along a predetermined trajectory from the leader craft to its nominal location. This control methodology was chosen because, in addition to the reference trajectory, the state feedback and control can be directly tuned with gains. Other control formulations — such as that discussed next — exhibit tuning parameters that affect control usage indirectly.

The chosen cost function is that of the classic Linear Quadratic Tracking (LQT) problem, where $\boldsymbol{X}_r$ is the reference trajectory, $[\mathcal{Q}]$ is the state feedback gain, $[\mathcal{R}]$ the control gain, and τ is the simulation duration.

$$J = \frac{1}{2}\int_{\tau} (\boldsymbol{X} - \boldsymbol{X}_r)^T [Q] (\boldsymbol{X} - \boldsymbol{X}_r) + \boldsymbol{U}^T [R] \boldsymbol{U} \mathrm{d}t \tag{5.54}$$

The Hamiltonian of the system is

$$\mathscr{H} = \frac{1}{2}\left[(\boldsymbol{X} - \boldsymbol{X}_r)^T [Q] (\boldsymbol{X} - \boldsymbol{X}_r) + \boldsymbol{U}^T [R] \boldsymbol{U}\right] + \boldsymbol{\lambda}^T \boldsymbol{X}' \tag{5.55}$$

Applying the necessary conditions yields

$$\boldsymbol{X}' = \left(\frac{\partial \mathscr{H}}{\partial \boldsymbol{\lambda}}\right)^T = \boldsymbol{X}' \tag{5.56}$$

$$\boldsymbol{0} = \left(\frac{\partial \mathscr{H}}{\partial \boldsymbol{U}}\right)^T = [\mathcal{R}]\boldsymbol{U} + \left[\frac{\partial \boldsymbol{X}'}{\partial \boldsymbol{U}}\right]\boldsymbol{\lambda} \Rightarrow \boldsymbol{U}^* = -[\mathcal{R}]^{-1}[B]\boldsymbol{\lambda} \tag{5.57}$$

$$\boldsymbol{\lambda}' = -\left(\frac{\partial \mathscr{H}}{\partial \boldsymbol{X}}\right)^T = -[\mathcal{Q}](\boldsymbol{X} - \boldsymbol{X}_r) - \left[\frac{\partial \boldsymbol{X}'}{\partial \boldsymbol{X}}\right]\boldsymbol{\lambda} = -[\mathcal{Q}]\Delta\boldsymbol{X} - [A]\boldsymbol{\lambda} \tag{5.58}$$

The Jacobians $[A]$ and $[B]$ are recognized above and are calculated using Eqs. (5.49) and (5.50). Recall that only linearized two-body gravity, drag, and Coulomb accelerations are used in these derivations. It is important to note a key distinction between the LQR and LQT controllers — the Jacobians are recomputed at each control time step for the latter. This has practical concerns for computing gains.

The equations above are combined to yield the well-known optimal control law for the LQT problem. The remaining derivations are passed over, as the relevant, novel pieces have already been explicated through the discussion above.

$$\boldsymbol{U}^*_{\mathrm{LQT}} = -[\mathcal{R}]^{-1}[B]^T([\mathcal{P}]\boldsymbol{X} - \boldsymbol{s}) = -[K]\boldsymbol{X} - [\mathcal{R}]^{-1}[B]^T\boldsymbol{s} \tag{5.59}$$

Here, $[\mathcal{P}]$ is the solution to the dynamic Ricatti equation, $[K]$ is the LQT gain analogous to the LQR gain above, and $\boldsymbol{s}$ describes the behavior of the reference trajectory. Because the system is assumed Linear Time Varying (LTV), $[\mathcal{P}]$ and $\boldsymbol{s}$ are integrated backward in time from null final conditions to their initial value. These precomputed values are applied along-side the integrated dynamics $\boldsymbol{X}$ at control time steps to calculate $\boldsymbol{U}^*_{\mathrm{LQT}}$.

5.6 Speed-Constrained Kinematic Steering (SCKS)

A control approach similar to that described in [78] is taken in deriving the second controller. Lyapunov's Direct Method is applied to yield a nonlinear control law to actuate the follower craft along a desired trajectory to rendezvous with the leader craft. Recall that the control authority for the electrostatic actuation system shown in Figure 5.1 drops off as the relative distance squared. Therefore, a saturating controller is desired so that reasonable voltages are sourced when the craft are far apart. The extreme hazard of collisions on orbit additionally motivates the use of a speed-constrained control law.

A candidate Lyapunov function is proposed.

$$\mathcal{V}_1 = \frac{1}{2}\delta\boldsymbol{\rho}^T\delta\boldsymbol{\rho} \tag{5.60}$$

Here, $\delta\boldsymbol{\rho} = \boldsymbol{\rho} - \boldsymbol{\rho}_r$ is the difference between the current leader-relative position of the follower and the reference trajectory. The derivative of this candidate function is shown in Eq. (5.61). It is important to recognize that $\delta\dot{\boldsymbol{\rho}}$ represents the inertial time derivative. This is a consequential difference from the previous controllers resulting from the use of a nonlinear tracking control framework. Since $\dot{\mathcal{V}}_1$ must be negative definite for the system to be asymptotically stable, the leader-relative velocity is set equal to an odd function $-\boldsymbol{f}(\delta\boldsymbol{\rho})$.

$$\dot{\mathcal{V}}_1 = \delta\boldsymbol{\rho}^T\delta\dot{\boldsymbol{\rho}} = -\delta\boldsymbol{\rho}^T\boldsymbol{f}(\delta\boldsymbol{\rho}) \tag{5.61}$$

Due to the possibility of collapsing the wake if overly large voltages are sourced, a control that saturates under large position differences is desired. A candidate function with this property is presented. Below, K is a scalar gain and $\delta\dot{\rho}_{\mathrm{max}}$ is the maximum allowed relative follower speed. Note that, as discussed previously, these gain values determine the shape and size of the saturating function $f_i(\delta\boldsymbol{\rho})$, whereas prior gains discussed balance state feedback and control usage directly.

$$f_i(\delta\boldsymbol{\rho}) = \tan^{-1}\left(\delta\rho_i \frac{K\pi}{2\delta\dot{\rho}_{\mathrm{max}}}\right)\frac{2\delta\dot{\rho}_{\mathrm{max}}}{\pi} \tag{5.62}$$

In order to constrain the leader-relative velocity to adhere to the equation above, an inner control loop must be derived which controls the accelerations. Consider the candidate Lyapunov function below as well as its derivative.

$$\mathcal{V}_2 = \frac{1}{2}\Delta\dot{\boldsymbol{\rho}}^T\Delta\dot{\boldsymbol{\rho}} \tag{5.63}$$

$$\dot{\mathcal{V}}_2 = \Delta\dot{\boldsymbol{\rho}}^T\Delta\ddot{\boldsymbol{\rho}} \tag{5.64}$$

The quantity $\Delta\dot{\boldsymbol{\rho}} = \delta\dot{\boldsymbol{\rho}} - \delta\dot{\boldsymbol{\rho}}^*$ represents the difference between the actual velocity deviation from the reference trajectory and that desired. The combination of the position and velocity control loops is realized by setting $\delta\dot{\boldsymbol{\rho}}^* = \boldsymbol{f}(\delta\boldsymbol{\rho})$. Given this definition, the derivative of $\Delta\dot{\boldsymbol{\rho}}$ is calculated.

$$\Delta\ddot{\boldsymbol{\rho}} = \delta\boldsymbol{a}_{\mathrm{C}} + \delta\boldsymbol{a}_{\mathrm{D}} + \delta\boldsymbol{a}_{\mathrm{G}} - \ddot{\boldsymbol{\rho}}_{\mathrm{r}} + \dot{\boldsymbol{f}}(\delta\boldsymbol{\rho}, \delta\dot{\boldsymbol{\rho}}) \tag{5.65}$$

The reference trajectory is later defined in the HCW frame for simplicity, so its inertial derivative is computed in terms of its HCW-frame derivatives (denoted by primes rather than dots) and the rotating-frame accelerations.

$$\ddot{\boldsymbol{\rho}}_{\mathrm{r}} = \boldsymbol{\rho}_{\mathrm{r}}'' + \dot{\boldsymbol{\omega}}_{\mathcal{H}/\mathcal{N}} \times \boldsymbol{\rho}_{\mathrm{r}} + 2\boldsymbol{\omega}_{\mathcal{H}/\mathcal{N}} \times \boldsymbol{\rho}_{\mathrm{r}}' + \boldsymbol{\omega}_{\mathcal{H}/\mathcal{N}} \times \boldsymbol{\omega}_{\mathcal{H}/\mathcal{N}} \times \boldsymbol{\rho}_{\mathrm{r}} \tag{5.66}$$

Finally, the derivative of the outer-loop saturating control function is presented.

$$\dot{f}_i(\delta\boldsymbol{\rho}, \delta\dot{\boldsymbol{\rho}}) = \frac{K\delta\dot{\rho}_i}{1 + \left(\delta\rho_i \frac{K\pi}{2\delta\dot{\rho}_{\mathrm{max}}}\right)^2} \tag{5.67}$$

In order to obtain a globally asymptotically stabilizing control, the Lyapunov rate in Eq. (5.64) is set equal to $-[P]\Delta\dot{\boldsymbol{\rho}}$, where $[P]$ is a matrix gain which determines how strictly the controller holds the spacecraft velocity to that defined in Eq. (5.62). The resulting control is obtained by using the least-squares inverse of the control effects matrix. This inverse is chosen because it guarantees a solution to the system and minimizes the norm of the control vector — providing a voltage set for the desired acceleration that is least likely to cause wake collapse.

$$\boldsymbol{U}^*_{\mathrm{SCKS}} = -[B]^T([B][B]^T)^{-1}\left([P](\Delta\dot{\boldsymbol{\rho}}) + \boldsymbol{f}(\delta\boldsymbol{\rho}) + \delta\boldsymbol{a}_{\mathrm{C}} + \delta\boldsymbol{a}_{\mathrm{D}} - \ddot{\boldsymbol{\rho}}_{\mathrm{r}} + \dot{\boldsymbol{f}}(\boldsymbol{\delta\rho}, \delta\dot{\boldsymbol{\rho}})\right) \tag{5.68}$$

5.7 Deployment and Rendezvous Simulations

The LQT and SCKS controllers are applied to deployment and rendezvous simulations, respectively. For both simulations, the leader craft's initial orbit elements are given by $\boldsymbol{r}_{\mathrm{L}} = [7000\ \mathrm{km}, 0, 0°, 0°, 20°, 10°]^T$. While these two operations are near inverses of one another dynamically, the electrostatic actuation control strategies applied differ dramatically as a result of the electrostatic interactions between the leader and follower. Dominating these effects is the $1/r^2$ Coulomb acceleration dependence which leads to much higher control authority when approaching the leader than when departing. Both control strategies make use of pre-defined reference trajectories. See the spacecraft parameters for both simulations displayed in Table 5.6. Note that in both simulations, Solar Radiation Pressure (SRP), J_2, and variations in drag are included as unmodeled perturbations.

Parameter	**Leader**	**Follower**
Number of Charged Spheres	10	1
Charged Sphere Radius (m)	0.25	0.25
Charge Structure Radius (m)	1	N/A
Mass (kg)	1000	1
Drag Coefficient	2.2	2.2
Reflectivity Coefficient	2	2
Cross-Sectional Area (m^2)	3.1415	0.0314

Table 5.6: Spacecraft Parameters for Deployment and Rendezvous Simulations

For both simulations, the controller's knowledge of the follower position and velocity is imperfect. Noise is added to the follower state in the form of a multivariate normal distribution centered on the truth with $\sigma_r = 5$ mm and $\sigma_v = 0.05$ mm as the variances of the positions and velocities, respectively. As mentioned previously, doubling or tripling this noise figure results in some controller diverging as discussed in later simulations. It is assumed that a variety of sensor information is combined to provide estimates with these noise characteristics.

5.7.1 Reference Trajectory Design Using Passive Dynamics

Trajectories making use of the natural dynamics between the two craft were chosen to reduce the control effort, resulting in the follower traveling to the nominal HCW position ($[0,-1,0]^T$ m). It is assumed that the initial conditions can be prescribed in both simulations, meaning that some deployment and/or actuation mechanism is available to bring the follower near its nominal position. The HCW formulation specifies a condition on a closed relative orbit. Without developing the formulation required to justify, this condition is that the offset in the HCW-x direction must be null. This is equivalent to saying that the follower and leader craft inertial orbits must have identical semi-major axes.[75] This means that an initial HCW-x velocity on the follower will generate a drift between the two craft which can be taken advantage of.

The HCW State Transition Matrix (STM) is used to map a given position back to the initial state of the follower. While the STM applies linearized gravity to the nonlinear simulation, the extremely close proximity between the leader and follower craft minimizes the resulting error.

$$\boldsymbol{X}_0 = \begin{pmatrix} \boldsymbol{\rho}_0 \\ \boldsymbol{\rho}'_0 \end{pmatrix} = [\Phi(t_0,t)]\boldsymbol{X}(t) = \begin{bmatrix} [\Phi_{\rho\rho}] & [\Phi_{\rho\rho'}] \\ [\Phi_{\rho'\rho}] & [\Phi_{\rho'\rho'}] \end{bmatrix} \begin{pmatrix} \boldsymbol{\rho}(t) \\ \boldsymbol{\rho}'(t) \end{pmatrix} \tag{5.69}$$

Equation (5.69) can be rearranged to solve for the initial velocity given an initial and final position. Expanding Eq. (5.69) yields two equations.

$$\boldsymbol{\rho}_0 = [\Phi_{\rho\rho}]\boldsymbol{\rho}(t) + [\Phi_{\rho\rho'}]\boldsymbol{\rho}'(t) \tag{5.70}$$

$$\boldsymbol{\rho}'_0 = [\Phi_{\rho'\rho}]\boldsymbol{\rho}(t) + [\Phi_{\rho'\rho'}]\boldsymbol{\rho}'(t) \tag{5.71}$$

Solving the first equation for $\boldsymbol{\rho}'(t)$ and rearranging gives an expression to calculation $\boldsymbol{\rho}'_0$ given the initial and final positions. Importantly, the final velocity must remain free, as the other three parameters are fixed.

$$\boldsymbol{\rho}_0' = [\Phi_{\rho'\rho}]\boldsymbol{\rho}(t) + [\Phi_{\rho'\rho'}][\Phi_{\rho\rho'}]^{-1}(\boldsymbol{\rho}_0 - [\Phi_{\rho\rho}]\boldsymbol{\rho}(t)) \tag{5.72}$$

This method is applied to generate a baseline reference trajectories for the next two simulations.

5.7.2 Simulation Environment Definitions

SRP is included as an unmodeled perturbation. Additionally, the controller development assumes a constant drag acceleration for a given orbit radius. In the simulated environment, both drag and SRP vary as they pass in and out of sunlight. Drag is varied sinusoidally by ±30% to roughly reflect density changes between sun and eclipse [18], while SRP is cut completely in shade. These simplified models are described in greater detail in Table 5.5 as in the LQR simulation.

5.7.3 Deployment Scenario Applying LQT Controller

The first simulation applies the control law in Eq. (5.59) to the deployment scenario so that the initial follower positions is $\boldsymbol{\rho}_0 = [0, 0, 0]^T$ m. The initial velocity calculated using Eq. (5.72) and used to generate the reference trajectory is $\boldsymbol{\rho}_0' = [0.270, 0, 0]^T$ m/s. The velocity was chosen such that the nominal position is achieved in half an orbit period. As mentioned previously, the final velocity must remain free to solve Eq. (5.69) for $\boldsymbol{\rho}_0'$, resulting in a non-zero velocity when the follower reaches the nominal position. Rather than immediately demand that the control cease all motion in the HCW-x direction — which would demand a great amount of control — the trajectory is altered to exponentially decrease the HCW-x velocity throughout another 0.25 orbits.

The matrix gains in Eq. (5.59) are replaced with scalars for this simulation and displayed in Table 5.7. Note that R is large because the charge product control vector magnitude is extremely small. Generally speaking, there is a range of values for R for which the controller functions properly. While poor choices for Q can result in system instability, the precise value does not significantly affect control performance for gain sets that achieve the nominal state.

Figure 5.12 shows the deviation between the follower's HCW position and velocity and the

Parameter	Value
R	2.5×10^{26}
Q	10

Table 5.7: Gains used in LQT deployment control simulation

nominal throughout the simulation. Note that the follower tends to oscillate about the nominal state rather than settling to it. This is due in part to the unmodeled drag and SRP variations, but also because the gains in Table 5.7 were not selected to critically damp the system, but rather to balance control usage with an acceptable deviation from the nominal state. Note that, with the selected gains, the nominal positions is held within roughly ±10 cm.

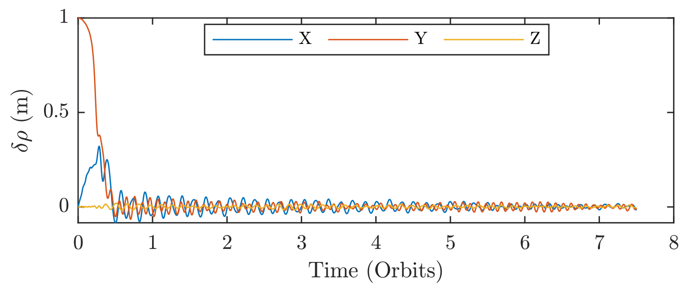

(a) Deviation of HCW position

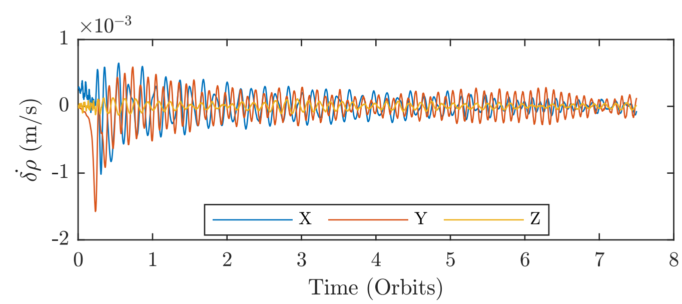

(b) Deviation of HCW velocity

Figure 5.12: Deviation of HCW position and velocity relative to nominal for LQT deployment control simulation

The effects of the added noise is clearly seen in Figure 5.13. Interestingly, while the voltage signals certainly exhibit some noisy characteristics, the overall magnitude of the voltages are not increased compared to simulations (not shown) in which perfect knowledge of the follower state is assumed. The voltages sourced by the controller are initially bounded within ±3000 V, though decay slightly in time. While the voltage limit for wake collapse is highly specific to a given system, generally speaking this voltage is large for LEO applications in which the relative kinetic energy between a craft the ionospheric ions is roughly 10 eV — several orders of magnitude lower than the electrostatic energy between an ion and the craft in this simulation.

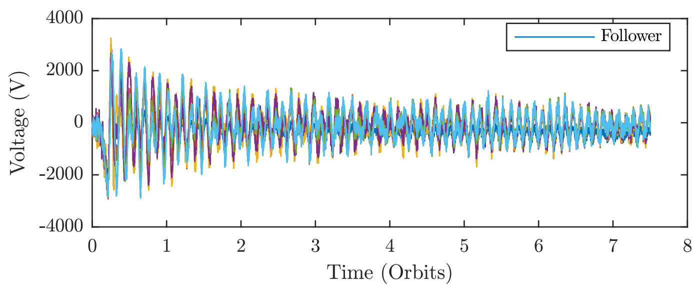

Figure 5.13: Control voltage for LQT deployment control simulation. Only the Follower's line is called out in the legend because the individual behavior of each of the charge structure's spheres is of no interest.

The structure of Figure 5.13 consists of a period in which the controller sources low potentials followed by a significant step increase as the nominal position is realized. The magnitude of negative voltages after this point is likely to collapse the wake of a leader with diameter 1 m based on the results presented in Chapter 3. Additionally, significant positive voltages are sourced. Therefore, large power would likely be required even if the wake does not collapse.

The structure of this control signal results from the fact that the reference follower velocity does not go to zero as the reference follower position does. Therefore, a more carefully designed reference trajectory — in which natural dynamics are leveraged, but the relative position and velocity go to zero together — may reduce the overall control usage for the LQT controller.

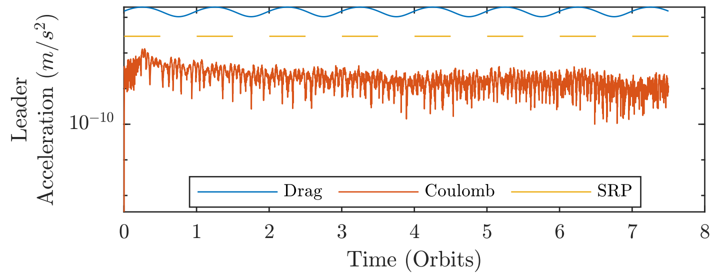

(a) Leader accelerations

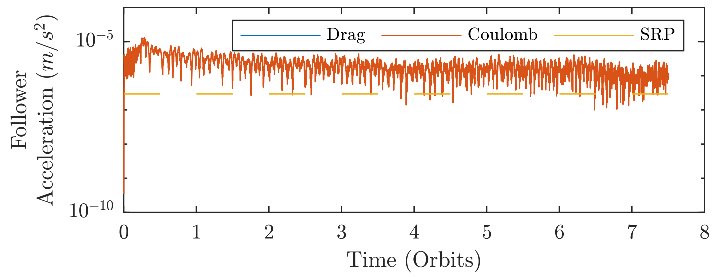

(b) Follower accelerations

Figure 5.14: Accelerations for LQT deployment control simulation

Finally, the acceleration magnitudes for the LQT deployment control simulation are shown in Figure 5.14. Note that these are the true, nonlinear accelerations applied in the simulation, not the linearized and abbreviated dynamics included in the controller derivation. The magnitude of the follower Coulomb acceleration is significantly higher than just the drag and SRP perturbations can account for. This is because the controller is also correcting on the differences in the two-body plus J_2 accelerations.

5.7.4 Rendezvous Scenario Applying SCKS Controller

The second simulation considers a scenario in which the two craft approach in the along-track (HCW-y) direction. Electrostatic actuation is used to place the follower at the nominal HCW state. It is assumed that the follower remains within the plasma wake at all times. The initial conditions are chosen with Eq. (5.72) to place the follower at the nominal position after a quarter of an orbit. It is important to note that, while the initial conditions are chosen using the HCW STM, the control feeds back on the offset from the nominal state, not an HCW trajectory.

The gains in Eq. (5.68) are displayed in Table 5.8.The initial HCW state of the follower — which would arrive at the off-nominal position after a quarter period given only HCW dynamics — is [-0.4000 m, -1.3425 m, 0 m, 0.0003 m/s, 0.0006 m/s, 0 m/s]^T.

Parameter	**Value**
K	0.001 s^{-1}
P	0.05 s^{-1}
$\delta\dot{\rho}_{\text{max}}$	0.001 m/s

Table 5.8: Gains used in SCKS rendezvous control simulation

The difference between the follower state and the nominal for the SCKS rendezvous scenario is displayed in Figure 5.15. Notice the noise is especially noticeable in the velocity picture in Figure 5.12(b), as the enforced limit on $\delta\dot{\rho}_{\text{max}}$ means that the velocity remains near the noise floor. Overall, the settling behavior of the SCKS rendezvous control simulation is far superior to that of the LQT deployment simulation shown in Figure 5.12. Indeed, the follower state remains very near the nominal once achieved, with small deviations resulting from unmodeled perturbations.

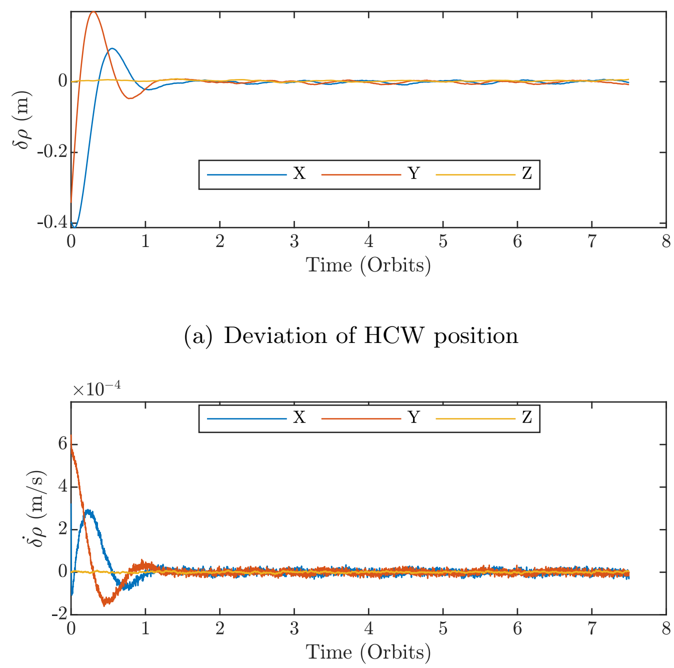

(a) Deviation of HCW position

(b) Deviation of HCW velocity

Figure 5.15: Deviation of HCW position and velocity relative to nominal for SCKS rendezvous control simulation

Note that the system does not settle to the nominal position in a quarter period, even though the initial conditions were intended to place the follower very near that position after that amount of time. This is because the gains and saturated position control are set such that reasonable voltages are sourced. These voltages are displayed in Figure 5.16.

The improved settling behavior relative to the previous simulation comes at the cost of signif-

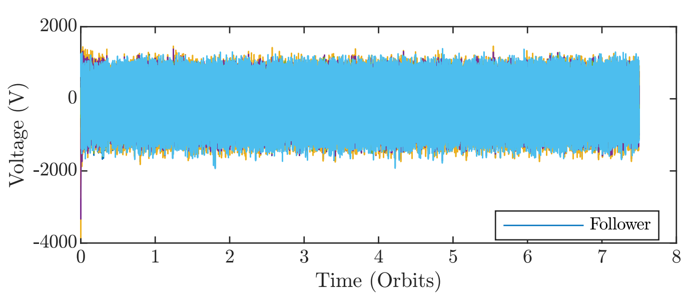

Figure 5.16: Control voltages for simulation 2. Only the Follower's line is called out in the legend because the individual behavior of each of the charge structure's spheres is of no interest.

icant control effort. As before, this controller is likely require significant power and/or collapse the wake. Interestingly, simulations assuming perfect knowledge of the follower location not presented in this dissertation used substantially less voltage (< 1000 V). This indicates the SCKS controller is extremely sensitive to the addition of noise and its magnitude.

An interesting difference between the simulations is the effect of adding noise. Though the same variances were used for both simulations, the SCKS controller does not handle the noise well, as seen in Figure 5.16. Simulations assuming perfect knowledge of the follower craft for simulation 2 (not pictured) sourced lower voltages, especially later in the simulation. This behavior can be understood via comparison with the LQT controller used in simulation 1. For this first controller, the effect of noise is diminished by the selection of a small state-feedback gain because the small position corruptions resulting from system noise do not generate a significant cost. The SCKS controller on the other hand has gains that allow one to shape the saturating function, but none that directly apply to control usage or state feedback.

While the addition of noise significantly impacts the SCKS controller, note that lower voltages are sourced overall relative to the LQT simulation. While the deployment versus rendezvous scenarios make one-to-one comparison impossible, it appears that the saturating controller has significant benefits.

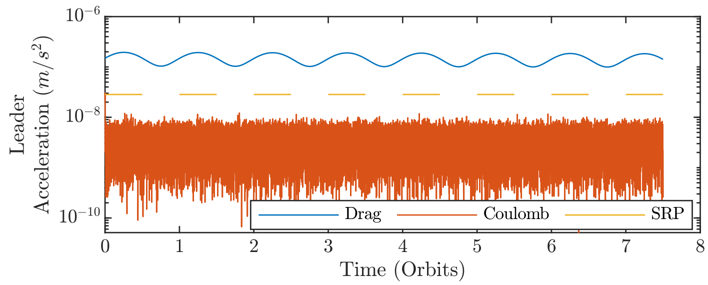

(a) Leader accelerations

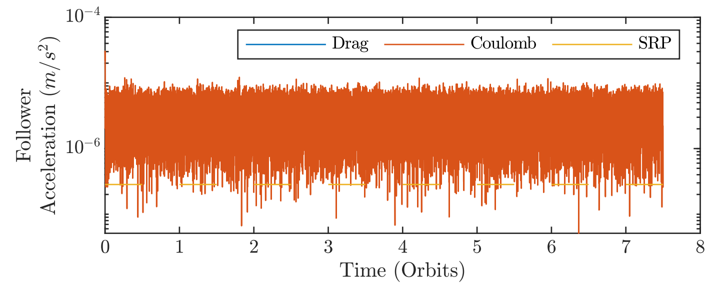

(b) Follower accelerations

Figure 5.17: Accelerations for SCKS rendezvous control simulation

The accelerations for this latter simulation are shown in Figure 5.17. As with the voltages plotted in Figure 5.16, the Coulomb accelerations are extremely noisy, but are of roughly the same magnitude as those in Figure 5.14.

5.7.5 Deployment and Rendezvous Simulation Conclusions

Two different charge product controllers are applied to two formation acquisition simulations. An LQT tracking law is derived using the optimal control framework followed by the SCKS controller which comes from Lyapunov Direct Method. Reference trajectories and initial conditions are generated for both deployment and rendezvous simulations using linearized gravity in the hopes of using passive dynamics to reduce control effort.

The LQT controller is able to settle a cubesatellite through deployment to its nominal position with reasonable accuracy, though some ringing is present. The settling time of 0.5 orbits is achieved almost perfectly by the controller, indicating that the reference trajectory was well adhered to. This is also indicated by the control voltage, though the chosen trajectory zeroed only the position at the desired time, not velocity, resulting in significant control usage after the nominal position was achieved.

Next, a rendezvous scenario is actuated using the SCKS charge product controller. This is a saturating controller, so there is less motivation to track a reference. Therefore, the SCKS controller fed back on the nominal position at all times, using only the HCW STM to generate initial conditions. Though the controller fails to achieve the desired settling time, the settling behavior is far superior to the LQT controller. This is because the saturating controller forces the dynamics to develop more slowly. In simulations not shown here which had no noise on follower position, this controller sourced low ($<$ 1000 V) potentials. Unfortunately, the controller is very sensitive to noise, generating large positive and negative potentials though as indicated above the system settles nicely.

The success of these two techniques in bringing the system — initially with leader and follower moving relative to each-other at ~cm/s velocities — to its nominal configuration indicates that a LEO mission could serve as a proof-of-concept for electrostatic actuation techniques, though a relatively large wake would be required. The addition of noise on the follower positions serves to substantially increase the voltages sourced by both controllers, though it is more noticeable in the SCKS controller. This could prove challenging for a scenario in which the follower craft is near the boundary of the plasma wake as a spike in noise could result in wake collapse. Other scenarios considering, per se, a cubesat in the wake of the International Space Station may handle this better, as potentials can drop off spatially between the follower craft and the wake boundary.

5.8 Control-Only Lagrangian (COL) Controller

The two main challenges identified from the formation acquisition simulations described above are reference trajectory design and noise. The latter of these depends on choices of sensors, lighting conditions, and a host of other variable parameters, and is the province of spacecraft orbit estimate, which is not a focus of this project. Therefore, the remainder of this dissertation focuses on improved reference trajectory design. As the SCKS controller did not seem to depend much on reference trajectory design, but is highly susceptible to noise, the optimal control framework is applied going forward.

5.8.1 Control Development

Consider the LQT cost function in Eq. (5.54). In minimizing this scalar function, the control usage and adherence to reference trajectory are priorities based on the control and state feedback gain, respectively. In general, the allowable state deviation is mission specific, depending on the objective at hand. In the case of electrostatic actuation, however, there are two rules of thumb for control usage: don't collapse the wake and don't charge positive in the wake. Therefore, an augmented cost function is considered which includes only the control usage magnitude. Note that the argument of the cost function is canonically referred to as the Lagrangian, hence the controller derived being named the Control-Only Lagrangian (COL) controller.

$$J = \frac{1}{2}\int_t^\tau \boldsymbol{U}^T\boldsymbol{U}\mathrm{d}t \tag{5.73}$$

While the control technique described below is not a novel of this project, the derivation provides insight into later applications and so is detailed here. The Hamiltonian of the system and the necessary conditions are computed.

$$\mathscr{H} = \frac{1}{2}\boldsymbol{U}^T\boldsymbol{U} + \boldsymbol{\lambda}^T\boldsymbol{X}' \tag{5.74}$$

$$\boldsymbol{X}' = \left(\frac{\partial\mathscr{H}}{\partial\boldsymbol{\lambda}}\right)^T = [A]\boldsymbol{X} + [B]\boldsymbol{U} \tag{5.75}$$

$$\boldsymbol{0} = \left(\frac{\partial\mathscr{H}}{\partial\boldsymbol{U}}\right)^T = \boldsymbol{U} + \left[\frac{\partial\boldsymbol{X}'}{\partial\boldsymbol{U}}\right]\boldsymbol{\lambda} \;\Rightarrow\; \boldsymbol{U}^* = -[B]^T\boldsymbol{\lambda} \tag{5.76}$$

$$\boldsymbol{\lambda}' = -\left(\frac{\partial\mathscr{H}}{\partial\boldsymbol{X}}\right)^T = \left[\frac{\partial\boldsymbol{X}'}{\partial\boldsymbol{X}}\right]\boldsymbol{\lambda} = -[A]^T\boldsymbol{\lambda} \tag{5.77}$$

Note that the lack of state feedback in the COL cost function results in a control law $\boldsymbol{U}^*$ that only feeds forward (i.e. it does not correct on deviations from the predicted nominal behavior). The consequences of this will be demonstrated shortly.

The equations derived from the necessary conditions provide the optimal control in terms of the costate which therefore must be computed. The costate differential equation identified by differentiating the Hamiltonian with respect to the state provides a method to accomplish this, though the initial condition $\boldsymbol{\lambda}_0$ must be determined. Consider the augmented state which stacks the system state and costate.

$$\tilde{\boldsymbol{X}} = \begin{bmatrix} \boldsymbol{X} \\ \boldsymbol{\lambda} \end{bmatrix} \tag{5.78}$$

The linear differential equation for this augmented state $\tilde{\boldsymbol{X}}'$ can be determined by inspection of Eqs. (5.75)-(5.77).

$$\tilde{\boldsymbol{X}}' = \begin{bmatrix} \boldsymbol{X}' \\ \boldsymbol{\lambda}' \end{bmatrix} = \begin{bmatrix} [A] & -[B][B]^T \\ [0] & -[A]^T \end{bmatrix} \begin{bmatrix} \boldsymbol{X} \\ \boldsymbol{\lambda} \end{bmatrix} = [\tilde{A}]\tilde{\boldsymbol{X}} \tag{5.79}$$

The linearity of the system indicates that the final augmented state can be related to its initial by the STM $[\Phi(t_f, t_0)] = [\Phi]$. This equation broken into block components.

$$\tilde{\boldsymbol{X}}_f = [\Phi]\tilde{\boldsymbol{X}}_0 = \begin{bmatrix} [\phi_{XX}] & [\phi_{\lambda X}] \\ [\phi_{X\lambda}] & [\phi_{\lambda\lambda}] \end{bmatrix} \begin{bmatrix} \boldsymbol{X}_0 \\ \boldsymbol{\lambda}_0 \end{bmatrix} \tag{5.80}$$

Given a chosen initial and final spacecraft state, the initial costate is calculated

$$\boldsymbol{\lambda}_0 = [\phi_{X\lambda}]^{-1}(\boldsymbol{X}_f - [\phi_{XX}]\boldsymbol{X}_0) \tag{5.81}$$

Therefore, the development of the optimal control above requires that the STM be computed. For linearized systems, the STM is computed with the matrix exponential of the system state dynamics matrix.

$$[\Phi(t, t_0)] = e^{[\tilde{A}(t)](t-t_0)} \tag{5.82}$$

At this stage a key assumption must be made. Calculation of the STM at a given time requires knowledge of the state dynamics matrix at this same time. While the system has been linearized, up until now no assumption has been made on how it varies in time. For the electrostatic actuation case, the $[\tilde{A}]$ matrix does vary with the control, which will obviously change in time as it seeks to settle the system. Therefore, the COL controller requires that the system is assumed Linear Time Invariant (LTI). One fact supporting this assumption is that the controller is designed to minimize control effort which will minimize variation in $[\tilde{A}]$. This assumption will result in limitations on the performance of the control response.

With the STM at all times calculable, Eq. (5.81) can be evaluated to calculate the initial costate. With initial conditions on the augmented state, the STM can be used to analytically compute the augmented state — and therefore the optimal control — at any time.

5.8.2 Rendezvous Scenario Applying COL Controller

The COL controller is implemented with the same system parameters as the rendezvous simulation described in Section 5.7.4. As a reminder, the initial HCW state is [-0.4000 m, -1.3425 m, 0 m, 0.0003 m/s, 0.0006 m/s, 0 m/s]^T. This is used to calculate the initial costate as in Eq. (5.81). This allows generation of nominal the trajectory and control shown in Figures 5.18 and 5.19. As with the initial conditions, the controller is designed to place the spacecraft at the nominal location in a quarter period.

Note that Figure 5.18(a) does not emulate the characteristic sinusoidal behavior of HCW solutions. Given that the initial conditions of this and the previous simulation are designed to achieve a dynamics-only rendezvous, this is an interesting result.

In practice, this linear, feed-forward-only controller has no mechanism for correcting on nonlinear dynamics or unmodeled perturbations. As evidenced throughout the discussion in this and other chapters, this makes it unsuitable for direct application for electrostatic actuation systems. While the charge product approach does allow for much more accurate approximation of the controlled Coulomb accelerations, they are still nonlinear in the state. Additionally, the extreme difficultly in accurately modeling on-orbit perturbations — particularly drag — will result in significant deviations from the desired trajectory.

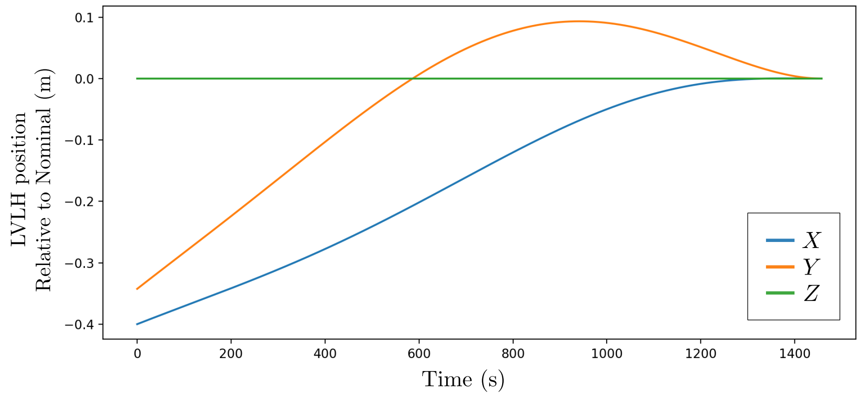

(a) LVLH reference positions

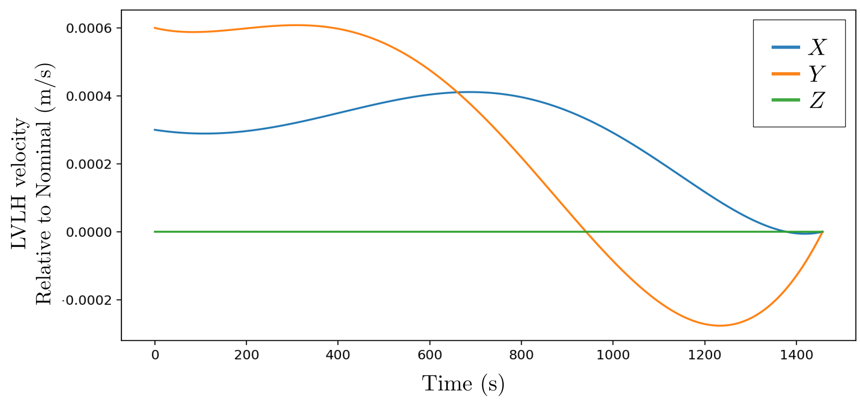

(b) LVLH reference velocities

Figure 5.18: Reference trajectory generated by COL controller

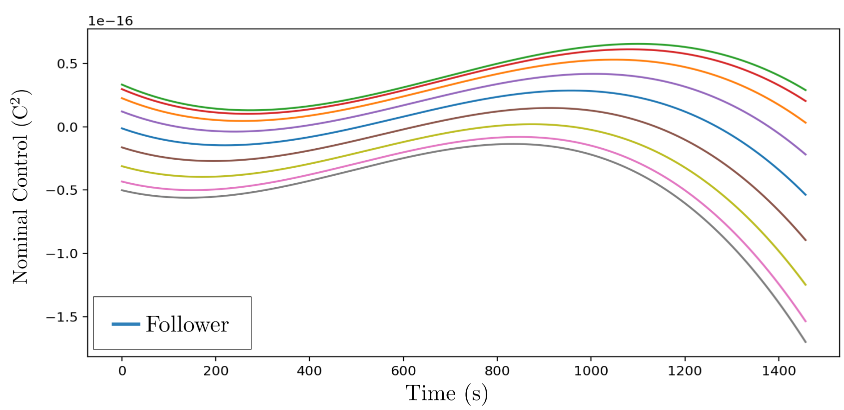

Figure 5.19: Reference charge product generated by COL controller

5.8.3 Rendezvous Scenario Applying LQT + COL Controller

Given the impracticality of implementing a feed-forward controller on a nonlinear system with unmodeled perturbations, a LQT controller as described in Section 5.7.3 is implemented. In this case, differential states and voltages are replaced in the cost function in Eq. 5.54. It should be noted that the reference trajectory shown in Figure 5.18 is augmented for an extended simulation. The nominal trajectory is appended to the end of that shown for the remainder of the simulation. The same noise figures were applied here as in previous simulations.

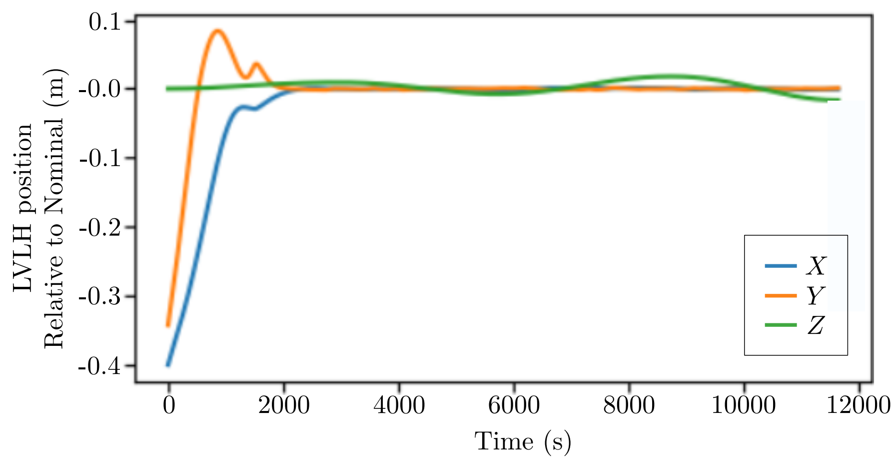

(a) LVLH reference positions

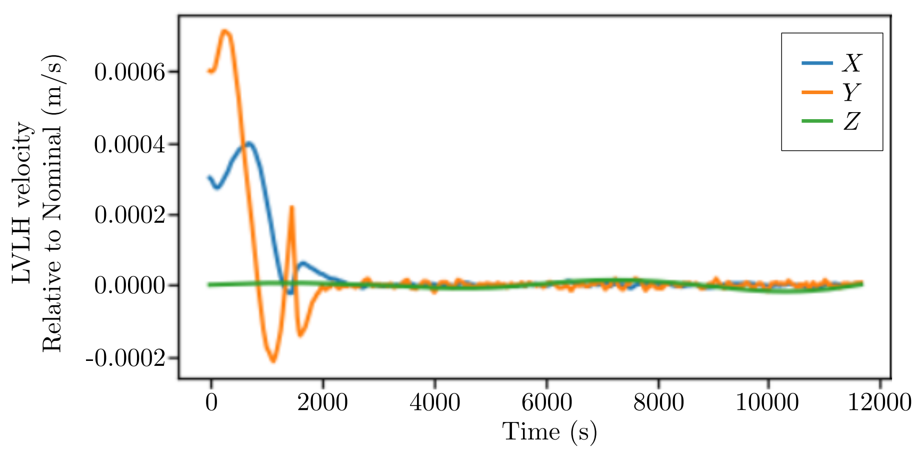

(b) LVLH reference velocities

Figure 5.20: Trajectory of LQT + COL controller

Interestingly, the same gains used in the LQT simulation displayed in 5.7 proved highly effective for this latter simulation, despite the significant differences in initial conditions and trajectory design. The controlled trajectory of this final electrostatic actuation simulation given unmodeled perturbations as described previously are shown in Figures 5.20.

Notice that the controller does not achieve the desired settling behavior at the desired time ($\sim$ 1400 s). This is a result of the chosen gains. Given the nonlinearities in the system, the maximum voltage — which is the limiting case for wake collapse as indicated in Chapter 3 — is reduced by allowing deviations from the reference trajectory.

The control voltages are shown in Figure 5.21. Recall that the controller returns charge products. There are infinitely many charge solutions that satisfy the desired charge product, meaning there are also infinitely many voltage sets. The follower voltage can therefore be chosen and the resulting charge structure voltages that achieve the charge product are calculated. Note a difference from the SCKS rendezvous simulation that the nominal follower voltage is chosen to be -3500 V. This is to minimize the positive voltages sourced by the electrostatic actuation system. Results from all simulations described indicate that significant ($\sim$kV) voltages are required to settle relative dynamics between spacecraft. Therefore, this simulation was tuned according to the assumption that the leader craft is extremely large and the wake is unlikely to collapse. While the follower voltage can be chosen to some degree, then nonlinear charge-to-voltage relationship described in Chapter 2 results in the charge structure spheres going to positive voltages regardless of follower voltage.

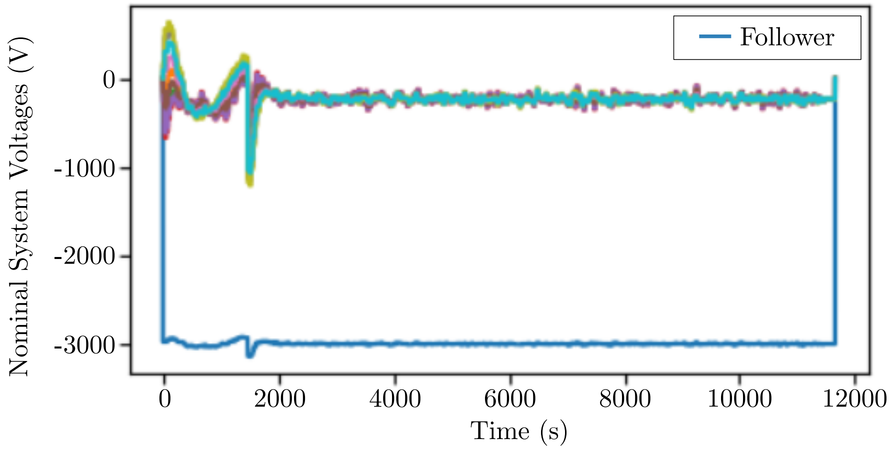

Figure 5.21: Voltages applied in LQT + COL controller given nominal follower voltage of -3500 V

Note from comparison of the LQT + COL control simulation results that the initial conditions and the transition between the COL-defined trajectory and control and the nominal to stabilize at the nominal position result in significant voltage spikes. The initial spike again indicates that the HCW-derived initial conditions are a poor choice. The final spike indicates that there should be some smoothing after the COL-defined trajectory is achieved.

5.8.4 COL + LQT Controller Conclusions

The controller derived in this section makes use of linearized models to generate a control-optimal reference trajectory and control. The feed-forward-only nature of this controller motivated the application of an additional tracking controller. Therefore, and LQT controller is implemented on the COL trajectory and control to guide a craft in for rendezvous.

The controller is designed to combine the best aspects of the previous LQT and SCKS controllers, and the results indicate success in this respect. The desired position is achieved in very nearly the desired time and relative position is maintained well before and after the nominal position has been achieved without massive control spikes. While positive voltages are sourced, a Nascap-2k simulation is run on a representative (large leader) system with these potentials to determine power usage and feasibility. The ion density behind a large (10 m) leader craft is shown with worst-case potentials applied as defined in Figure 5.21 (i.e. V_f =-3500 V, V_{cs}=550 V).

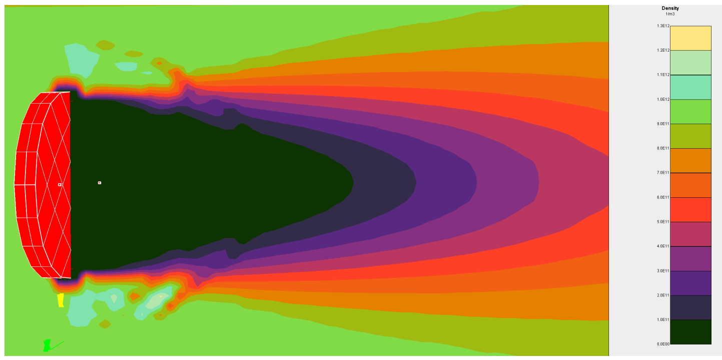

Figure 5.22: Ion density near electrostatic actuation system assuming large leader craft

The Nascap-2k simulation indicates that for a 10 m diameter craft, the wake will not collapse given the worst-case potentials. However, the presence of positive potentials applied in the wake does result in a worst-case power draw of ∼600 W. Given that on-orbit experiments have demonstrated ∼4.5 kV charging with an 800 W electron beam [72] the cited power can feasibly be sourced on orbit. Notably, positive potentials sourced in an electron plasma as in the wake are shielded so theoretically the accelerations would be reduced. However, the simulations in Chapter 3 indicate that all electrons in the vicinity of these positive charges are absorbed so no shielding is expected.

Given these results, feasibility of a cubesatellite-ISS electrostatic actuation demonstration is claimed. The ISS will create a wake much larger than the 10 m modeled in the Nascap-2k simulation. Additionally, the power system can likely take the maximum 600 W expected for the simulation shown. This achieves the overall goal of this dissertation.

5.9 Results & Summary of Goal 4

The foundational knowledge gained from the projects described in previous chapters of this dissertation are applied to investigate the feasibility of electrostatic actuation in LEO. The time-varying MSM technique presented in Chapter 2 is used to determine an analytic expression for the Coulomb acceleration between close-proximity leader and follower craft in LEO. This expression is linearized about a nominal state and voltage control variable and and LQR controller is derived to stabilize the follower state in the leader HCW frame. The controller is able to settle the formation in a relatively short timespan, though unmodeled perturbations and nonlinearities preclude precise convergence. The control voltages sourced were unlikely to collapse the wake given simulation parameters, though the leader craft diameter simulated is large for LEO and wake shaping techniques would likely need to be applied to avoid wake collapse. Only positive voltages were sourced by the controller, so the power requirement assuming no wake collapse would be minimal according to simulations in Chapter 3.

The major limitation on the LQR voltage controller is the nonlinearity of the Coulomb acceleration in voltage. Very large changes in voltages result in very small changes to accelerations. Therefore, large state deviations or increased noise can cause the linearity assumption to become invalid, potentially leading to system instability. This motivated the use of the charge product control variable, in which the Coulomb acceleration is naturally linear.

Two controllers are derived using the charge product control equations and applied to each of two formation acquisition scenarios. Reference trajectories and initial conditions were generated using the HCW STM so that passive dynamics could be leveraged to reduce control effort. The LQT controller derived within the optimal control framework performed well and efficiently under noise until the nominal position was reached, at which point a large amount of control is sourced and significant state deviation are seen. Given the leader craft geometry defined in simulation, the voltages sourced are likely to collapse the wake unless significant expansion efforts are undertaken. The reason for this control spike is that the HCW reference trajectory designed brings the initial state but not velocity to zero at the desired time. The overall take away is that the charge product LQT controller seems robust to noise but sensitive to reference trajectory.

A controller that is robust to reference trajectory is desirable, as generation of good trajectories can be difficult and computationally expensive, often requiring iteration on an initial guess. In the context of electrostatic actuation, a robust controller is one that sources low (preferably negative) voltages regardless of the reference trajectory chosen. The saturating SCKS controller was derived with this in mind. A regulation-type feedback scheme is applied to avoid reference trajectory generation all together. The control simulation is initialized with conditions generated with the HCW STM, but the trajectory resulting from the SCKS control is not an HCW trajectory. The setting behavior is improved relative to previous simulations, in part because the effecting settling time chosen is much longer — formation stabilization takes almost quadruple the time as compared to the LQT system. The control signal lacks any clear dependence on the state, but is instead large and oscillatory, indicating that the SCKS controller — though it avoids the reference trajectory problem — is sensitive to noise. Note the inverse relative to the conclusions on the LQT controller.

The conclusions drawn from the control simulations described indicate that measurements noise and reference trajectory generation are the chief concerns for the electrostatic actuation techniques explored. The problem of measurement noise depends heavily on the sensors being used and filtering techniques, which are considered out of scope. Therefore, the final aspect of this dissertation was to investigate improved methods for creating reference trajectories. The optimal control framework is again applied to derive the COL controller. The analytic expressions for the state and control trajectories are impractical for use on orbit, as they are derived with imperfect dynamics models. However, a LQT controller implemented on the reference state and control is derived for final control simulations.

The results indicate that the designed controller is suitable for the described electrostatically actuated system along the designed trajectories. Resistance to noise and excellent adherence to the desired trajectory are demonstrated by the COL+LQT controller. A Nascap-2k is run with a large 10 m leader craft and the worst-case potentials from the control simulations. Maximum power requirements of ∼600 W are demonstrated. According to these results, feasibility of a cubesatellite-ISS technological demonstration is established.

The goal of this chapter was to combine the knowledge gained from the previously described projects to design electrostatic actuation control techniques feasible for application in LEO plasma wakes. Four control techniques are applied to a variety of scenarios, yielding great insight into the prospects and challenge of this novel actuation techniques. Control simulations showed good settling behavior and feasibility is established, given careful system, controller, and reference trajectory design. A final controller is derived that is robust both to initial conditions and system noise. Nascap-2k simulations applying control simulation results indicate feasibility of electrostatic actuation in LEO plasma wakes. Therefore, the goal of this dissertation has been achieved.

Chapter 6

Conclusions & Summary

6.1 Research Overview & Contributions

The benefits of electrostatic actuation in GEO have been establish in recent years. The technique offers significant fuel savings across a range of close-proximity operations compared with conventional thrusters in addition to reduced risk arising from its touchless nature. However, demonstration in a representative environment is prerequisite to application in the GEO environment. This dissertation describes methods for demonstrating electrostatic actuation in LEO plasma wakes.

The development of electrostatic actuation technologies in any orbit requires an analytic model of Coulomb forces between nearby craft. This is a significant challenge as analytic expressions exist for only extremely basic geometries. Recently the Multi-Sphere Method (MSM) was developed to approximate electric fields around complex geometries. A major contribution of this project was the demonstration that MSM applies over significant reconfiguration. Given this fact, it was established that MSM could be applied to accurately simulate Coulomb forces between spacecraft experiencing relative motion. This result was published in the Journal of Spacecraft and Rockets in March 2020.[57]

The next step in establishing feasibility of electrostatic actuation in LEO was an investigation of charged plasma wake dynamics. Nascap-2k simulations indicated a balance between positive and excessively negative potentials to mitigate power. The conclusion drawn is that small negative potentials should be used when possible unless a large wake can be generated. This motivated studies of techniques for expanding a craft's plasma wake. Thin, positively charged structures are considered to minimize launch mass and area-dependent perturbations. It is shown experimentally that sparse geometries can generate plasma wakes, though with increased ion populations relative to solid objects. The experimental investigation resulted in a publication in IEEE Transactions on Plasma Sciences in October 2019.[56] Further experiments consider the power requirements of electrostatic actuation while applying wake expansion indicating a balance between leader and follower potential to avoid wake collapse.

Lessons learned from these experiments are applied in deriving a novel technique for simulating a LEO-like plasma terrestrially. A variety of design considerations are described and notional parameters for the ECLIPS chamber are establish. Ion telescopes leveraging spacecharge spreading to enhance magnification are described and simulated to inform the design of future experimental LEO plasma wake investigations.

The final aspect of the project is fundamental to the research goal of establishing feasibility for demonstrating electrostatic actuation in LEO plasma wakes. The development of control strategies which minimize the possibility of wake collapse is the main objective. The direct dependence of wake collapse on follower craft potential initially motivated the use of a voltage control variable. This technique proved impractical for significant noise or state deviations as the Coulomb acceleration is highly nonlinear in voltage. This motivated the use of charge-product control schemes which are far more linear than the alternative. The results of the voltage control simulation are detailed in a submission to Acta Astronautic currently under review.

Linear Quadratic Tracking (LQT) and Speed Constrained Kinematic Steering (SCKS) controllers are derived for deployment and rendezvous simulations, respectively. The LQT controller performs well while traveling along a reference trajectory designed to achieve the nominal position, but sources excessive control when this is achieved as the velocity of the reference trajectory is not null at this time. Significant ringing around the nominal state was seen as well. The SCKS controller, on the other hand, follows a smooth trajectory that settles well on the desired position. However, this control strategy is extremely sensitive to noise, resulting in significant large positive and negative potentials throughout the simulation time. These results were combined in a submission accepted by Advances in Space Research and currently under production.

Given these insights, a final controller is designed. The major shortcoming of the LQT simulation described was the dependence on reference trajectory. Therefore, the optimal control framework is leveraged alongside linearized dynamics to yield a control-optimal trajectory to achieve given relative motion — the so-called Cost-Only Lagrangian (COL) controller. An LQT controller is implemented on this trajectory to consider a rendezvous simulation. The results of the COL + LQT controller indicate excellent settling behavior with low potentials sourced despite noise in the system.

The object potentials and rough geometry of this last simulation are simulated in Nascap-2k to establish feasibility of electrostatic actuation in LEO plasma wakes. Based on the results, a cubesatellite-ISS technology demonstration is feasible. Therefore the dissertation goal is achieved.

6.2 Recommendations for Future Work

Given the conclusions drawn from the Nascap-2k simulations, the main obstacle to electrostatic actuation in LEO is plasma wake collapse. Results described in Chapter 3 indicate that a balance between wake size and follower voltage must be struck. Therefore, the primary recommendations for future work are continued investigation of wake shaping techniques and applicable control strategies.

Significant recommendations for continued wake shaping investigations are already recorded in Chapter 4. The construction of a LEO simulation chamber with ideal environmental properties is extremely difficult, indicating that the scaling laws introduced by reference [19] should be applied to achieve similarity. The difficulty here is the extremely large parameter space available in addition to the challenge of precisely achieving any desired plasma parameter.

The final recommendation for continuation of this research is further investigation of applicable control techniques. One challenge with the COL reference trajectory was that the linear assumption failed for long settling times. This makes gain tuning difficult for some scenarios. The

COL controller could be iterated and applied multiple times along a notional trajectory such that linearization is assumed over smaller spatial scales. An additional consideration is the applications of constraints to the COL derivation. While complicating the development, this could allow for controllers which conform better to the limits of LEO electrostatic actuation.

Bibliography

[1] A Adams and FH Read. Electrostatic cylinder lenses iii: Three element asymmetric voltage lenses. Journal of Physics E: Scientific Instruments, 5(2):156, 1972.

[2] Phillip C. Anderson. Characteristics of spacecraft charging in low Earth orbit. Journal of Geophysical Research: Space Physics, 117(7):1–11, 2012.

[3] Vladimir Aslanov and Hanspeter Schaub. Detumbling attitude control analysis considering an electrostatic pusher configuration. AIAA Journal of Guidance, Control, and Dynamics, 42(4):900–909, April 2019.

[4] Vladimir Aslanov and Vadim V. Yudintsev. Motion control of space tug during debris removal by a coulomb force. AIAA Journal of Guidance, Control, and Dynamics, 41(7):1476–1484, 2018.

[5] Vladimir S. Aslanov. Chaotic dynamics of a satellite with flexible appendages in the coulomb interaction. Journal of Guidance Control and Dynamics, 2017. (in review).

[6] Vladimir S. Aslanov. Exact solutions and adiabatic invariants for equations of satellite attitude motion under coulomb torque. Nonlinear Dynamics, 90(4):2545–2556, Dec. 2017.

[7] Vladimir S. Aslanov. Spatial dynamics and control of a two-craft coulomb formation. AIAA Journal of Guidance, Control, and Dynamics, available online 2019.

[8] AA Azooz. Four free parameter empirical parametrization of glow discharge langmuir probe data. Review of Scientific Instruments, 79(10):103501, 2008.

[9] Miles Bengtson, Kieran T. H. Wilson, and Hanspeter Schaub. Experimental results of electron method for remote spacecraft charge sensing. Space Weather, 18(3):1–12, March 2020.

[10] Trevor Bennett and Hanspeter Schaub. Touchless electrostatic three-dimensional detumbling of large axi-symmetric debris. The Journal of the Astronautical Sciences, 62(3):233–253, 2015.

[11] Trevor Bennett and Hanspeter Schaub. Touchless electrostatic three-dimensional detumbling of large geo debris. Journal of Astronautical Sciences, 62(3):233–253, Sept. 2015.

[12] Trevor Bennett and Hanspeter Schaub. Touchless electrostatic detumble of a representative box-and-panel spacecraft configuration. In European Conference on Space Debris, ESOC, Darmstadt, Germany,, April, 18–21 2017.

[13] Trevor Bennett and Hanspeter Schaub. Contactless electrostatic detumbling of axi-symmetric geo objects with nominal pushing or pulling. Advances in Space Research, 62(11), December 2018.

[14] Trevor Bennett, Daan Stevenson, Erik Hogan, Lauren McManus, and Hanspeter Schaub. Prospects and challenges of touchless debris despinning using electrostatics. Advances in Space Research, 56(3):557–568, Aug. 2015.

[15] Trevor Bennett, Daan Stevenson, Erik Hogan, and Hanspeter Schaub. Prospects and challenges of touchless electrostatic detumbling of small bodies. Advances in Space Research, 56(3):557–568, 2014.

[16] John Berryman and Hanspeter Schaub. Analytical charge analysis for 2- and 3-craft coulomb formations. AIAA Journal of Guidance, Control, and Dynamics, 30(6):1701–1710, Nov.–Dec. 2007.

[17] KATHARINE B BLODGETT. Currents limited by space charge between concentric spheres. In Thermionic Phenomena, pages 125–135. Elsevier, 1961.

[18] Sean L Bruinsma and Jeffrey M Forbes. Medium-to large-scale density variability as observed by champ. Space Weather, 6(8), 2008.

[19] CJ Capon, M Brown, and RR Boyce. Scaling of plasma-body interactions in low earth orbit. Physics of Plasmas, 24(4):042901, 2017.

[20] Philip Chow, Joseph Hughes, Trevor Bennett, and Hanspeter Schaub. Automated sphere geometry optimization for the volume multi-sphere method. In AAS/AIAA Spaceflight Mechanics Meeting, Napa Valley, California, Feb. 14–18 2016. Paper No. AAS-16-472.

[21] David L Cooke and Ira Katz. Tss-1r electron currents: Magnetic limited collection from a heated presheath. Geophysical research letters, 25(5):753–756, 1998.

[22] Russell Cooper and Ryan Hoffman. Jumbo space environment simulation and spacecraft charging chamber characterization. Technical report, Air Force Research Laboratory, Space Vehicles Directorate Kirtland AFB United States, 2015.

[23] DA Dahl, JE Delmore, and AD Appelhans. Simion pc/ps2 electrostatic lens design program. Review of Scientific Instruments, 61(1):607–609, 1990.

[24] V.A. Davis and M.J. Mandell. High-voltage interactions in plasma wakes: Simulation and flight measurements from the Charge Hazards and Wake Studies (CHAWS) experiment. Journal of Geophysical Research, 104(A6):12,445–12,459, 1999.

[25] VA Davis and MJ Mandell. Nascap-2k version 4.2 scientific documentation. Technical report, Leidos, Inc. San Diego United States, 2014.

[26] Victoria Davis, Myron Mandell, David Cooke, and Dale Ferguson. Nascap-2k spacecraft-plasma environment interactions modeling: New capabilities and verification. In 45th AIAA Aerospace Sciences Meeting and Exhibit, page 1096, 2007.

[27] Benoit Durand de Gevigney, Thomas Sunn Pedersen, and Allen H Boozer. Debye screening and injection of positrons across the magnetic surfaces of a pure electron plasma in a stellarator. Physics of Plasmas, 18(1):013508, 2011.

[28] Casey Farnell. Magnetic Filter Plasma Source Test Report. Plasma Controls, LLC.

[29] DC Ferguson and GB Hillard. Low earth orbit spacecraft charging design guidelines. NASA Technical Report, 212287(2), 2003.

[30] Henry B Garrett and Albert C Whittlesey. Spacecraft charging, an update. IEEE transactions on plasma science, 28(6):2017–2028, 2000.

[31] William Hall, Philip Leung, Ira Katz, Garya Jongeward, and John Lilley. Polar-auroral charging of the space shuttle and eva astronaut. AGARD, The Aerospace Environment at High Altitudes and its Implications for Spacecraft Charging and Communications 9 p(SEE N 87-26937 21-18), 1987.

[32] Roger F Harrington. Field computation by moment methods. Wiley-IEEE Press, 1993.

[33] Andrew T. Harris, Christopher Petersen, and Hanspeter Schaub. Linear Coupled Attitude-Orbit Control Through Aerodynamic Forces. 2018 Space Flight Mechanics Meeting, (January):1–13, 2018.

[34] D E Hastings. A review of plasma interactions with spacecraft in low Earth orbit. Journal of Geophysical Research, 100(A8):14457–14483, 1995.

[35] DE Hastings. A review of plasma interactions with spacecraft in low earth orbit. Journal of Geophysical Research: Space Physics, 100(A8):14457–14483, 1995.

[36] Erik Hogan and Hanspeter Schaub. Collinear invariant shapes for three-craft coulomb formations. Acta Astronautica, 12:78–89, March–April 2012.

[37] Erik Hogan and Hanspeter Schaub. Relative motion control for two-spacecraft electrostatic orbit corrections. AIAA Journal of Guidance, Control, and Dynamics, 36(1):240–249, Jan. – Feb. 2013.

[38] Erik Hogan and Hanspeter Schaub. General high-altitude orbit corrections using electrostatic tugging with charge control. AIAA Journal of Guidance, Control, and Dynamics, 38(4):699–705, April 2015.

[39] Erik A. Hogan and Hanspeter Schaub. Impacts of tug and debris sizes on electrostatic tractor charging performance. Advances in Space Research, 55(2):630–638, January 15 2015.

[40] Joseph Hughes and Hanspeter Schaub. Rapid modeling of electrostatic forces and torques considering dielectrics. In International Astronautical Congress, Bremen, Germany, Oct. 1–5 2018. Paper No. A6,10-C1.7,6,x42812r.

[41] Joseph Hughes and Hanspeter Schaub. Heterogeneous surface multi-sphere models using method of moments foundations. Journal of Spacecraft and Rockets, 2019. (in press).

[42] Gabriel Ingram, Joseph Hughes, Trevor Bennett, Christine Reilly, and Hanspeter Schaub. Volume multi-sphere-model development using electric field matching. Journal of Astronautical Sciences, 65(4):377–399, 2018.

[43] J. D. Jackson. Charge density on thin straight wire , revisited Charge density on thin straight wire , revisited. American Journal of Physics, 789(68), 2000.

[44] I Katz, BM Gardner, MJ Mandell, GA Jongeward, M Patterson, and RM Myers. of plasma contactor performance. Journal of spacecraft and rockets, 34(6):824–828, 1997.

[45] Lyon B King, Gordon G Parker, Satwik Deshmukh, and Jer-Hong Chong. Spacecraft formation-flying using inter-vehicle coulomb forces. NIAC Phase I Final Report, 2002.

[46] ME Kiziroglou, X Li, AA Zhukov, PAJ De Groot, and CH De Groot. Thermionic field emission at electrodeposited ni–si schottky barriers. Solid-State Electronics, 52(7):1032–1038, 2008.

[47] Shu T Lai. Spacecraft charging thresholds in single and double maxwellian space environments. IEEE transactions on nuclear science, 38(6):1629–1634, 1991.

[48] Shu T Lai. Fundamentals of Spacecraft Charging: Spacecraft Interactions with Space Plasmas. Princeton University Press, 2011.

[49] Helmut Liebl. Applied charged particle optics, volume 2012. Springer, 2008.

[50] Myron J Mandell, Victoria A Davis, David L Cooke, Adrian T Wheelock, and Christopher J Roth. Nascap-2k spacecraft charging code overview. IEEE Transactions on Plasma Science, 34(5):2084–2093, 2006.

[51] John C Mankins. Technology readiness levels. White Paper, April, 6:1995, 1995.

[52] Anthony R Martin. Numerical Solutions to the problem of charged particle flow around an Ionospheric Spacecraft. 22(d):121–141, 1974.

[53] Jordan Maxwell, Andrew Harris, and Hanspeter Schaub. Balancing differential drag with coulomb repulsion in low earth orbit plasma wakes. In International Astronautical Congress, Bremen, Germany, Oct. 1–5 2018. Paper No. C1,6,2,x45169.

[54] Jordan Maxwell, Ryan Hoffmann, and Hanspeter Schaub. Low earth orbit plasma wake shaping and applications to on orbit proximity operations. In SCTC Conference Proceedings, number 1, 2018.

[55] Jordan Maxwell and Hanspeter Schaub. Electrostatic actuation within expanded low earth orbit plasma wakes: Experiments and analysis. In AIAA Science and Technology Forum and Exposition, San Diego, CA, Jan. 7–11 2019.

[56] Jordan Maxwell and Hanspeter Schaub. Low earth orbit plasma wake shaping and applications to on-orbit proximity operations. IEEE Transactions on Plasma Science, 47(10):4760–4769, 2019.

[57] Jordan Maxwell, Kieran T. H. Wilson, Mahdi Ghanei, and Hanspeter Schaub. Multisphere method for flexible conducting space objects: Modeling and experiments. AIAA Journal of Guidance, Control, and Dynamics, 57(2):225–234, Aug. 19–23 2020.

[58] WJ Miloch, VV Yaroshenko, SV Vladimirov, HL Pecseli, and J Trulsen. Spacecraft charging in flowing plasmas; numerical simulations. In Journal of Physics-Conference Series, volume 370, page 012004, 2012.

[59] Wojciech J Miloch. Wake effects and Mach cones behind objects. Plasma Physics and Controlled Fusion, 52(12):124004, 2010.

[60] Y. Miyake, C. M. Cully, H. Usui, and H. Nakashima. Plasma particle simulations of wake formation behind a spacecraft with thin wire booms. Journal of Geophysical Research: Space Physics, 118(9):5681–5694, 2013.

[61] John H Moore, Christopher C Davis, Michael A Coplan, and Sandra C Greer. Building scientific apparatus. Cambridge University Press, 2009.

[62] P Mora. Plasma expansion into a vacuum. Physical Review Letters, 90(18):185002, 2003.

[63] Arun Natarajan and Hanspeter Schaub. Linear dynamics and stability analysis of a Two-Craft Coulomb tether formation. Advances in the Astronautical Sciences, 120(II):1635–1649, 2005.

[64] Arun Natarajan and Hanspeter Schaub. Linear dynamics and stability analysis of a coulomb tether formation. Journal of Guidance, Control, and Dynamics, 29(4):831–839, July–Aug. 2006.

[65] Arun Natarajan, Hanspeter Schaub, Gordon G Parker, Arun Natarajan, Hanspeter Schaub, and Gordon G Parker. Reconfiguration of a Nadir-Pointing 2-Craft Coulomb Tether Journal of British Interplanetary Society. 60(6):209–218, 2007.

[66] Torsten Neubert, PM Banks, BE Gilchrist, AC Fraser-Smith, PR Williamson, WJ Raitt, NB Myers, and S Sasaki. The interaction of an artificial electron beam with the earth's upper atmosphere: Effects on spacecraft charging and the near-plasma environment. Journal of Geophysical Research: Space Physics, 95(A8):12209–12217, 1990.

[67] Max Newport. Jumbo CSU Magnetic Filter Plasma Source Characterization. Spacecraft Charging Instrumentation and Calibration Laboratory.

[68] AV Phelps and Z Lj Petrovic. Cold-cathode discharges and breakdown in argon: surface and gas phase production of secondary electrons. Plasma Sources Science and Technology, 8(3):R21, 1999.

[69] FH Read. Accurate calculations of double-aperture electrostatic immersion lenses. Journal of Physics E: Scientific Instruments, 2(2):165, 1969.

[70] C.M. Saaj, Vaios Lappas, Hanspeter Schaub, and Dario Izzo. Hybrid propulsion system for formation flying using electrostatic forces. Aerospace Science and Technology, 14(5):348 – 355, 2010.

[71] U Samir, R Gordon, L Brace, and R Theis. The Near-Wake Structure of the Atmosphere Explorer C (AE-C) Satellite' A Parametric Investigation. Journal of Geophysical Research, 84, 1979.

[72] Susumu Sasaki, Nobuki Kawashima, Kyoichi Kuriki, Masahisa Yanagisawa, and Tatsuzo Obayashi. Vehicle Charging Observed in SEPAC Spacelab-1 Experiment. Journal of Spacecraft and Rockets, 23(2):194–199, 1986.

[73] Hanspeter Schaub. Stabilization of satellite motion relative to a coulomb spacecraft formation. Journal of Guidance, Control and Dynamics, 28(6):1231–1239, Nov.–Dec. 2005.

[74] Hanspeter Schaub, Christopher Hall, and John Berryman. Necessary conditions for circularly-restricted static coulomb formations. Journal of the Astronautical Sciences, 54(3–4):525–541, July-Dec. 2006.

[75] Hanspeter Schaub and John L Junkins. Analytical mechanics of space systems. American Institute of Aeronautics and Astronautics, 2005.

[76] Hanspeter Schaub and Daniel F. Moorer. Geosynchronous large debris reorbiter: Challenges and prospects. The Journal of the Astronautical Sciences, 59(1–2):161–176, 2014.

[77] Hanspeter Schaub, Gordon G. Parker, and Lyon B. King. Challenges and prospect of coulomb formations. Journal of the Astronautical Sciences, 52(1–2):169–193, Jan.–June 2004.

[78] Hanspeter Schaub and Scott Piggott. Speed-constrained three-axes attitude control using kinematic steering. Acta Astronautica, 174:1–8, June 2018.

[79] Hanspeter Schaub and Zolt'an Sternovsky. Active space debris charging for contactless electrostatic disposal maneuvers. Advances in Space Research, 43(1):110–118, 2014.

[80] Hanspeter Schaub and Daan Stevenson. Prospects of relative attitude control using coulomb actuation. Journal of the Astronautical Sciences, 60(3):258–277, 2013.

[81] Carl R Seubert and Hanspeter Schaub. One-dimensional testbed for coulomb controlled spacecraft. In AAS/AIAA Spaceflight Mechanics Meeting, Savannah, GA, pages 09–015, 2009.

[82] Carl R. Seubert and Hanspeter Schaub. Closed-loop one-dimensional charged relative motion experiments simululating constrained orbital motion. AIAA Journal of Guidance, Control, and Dynamics, 33(6):1856–1865, 2010.

[83] Elvis D. Silva. A Formulation of the Clohessy-Wiltshire Equations to Include Dynamic Atmospheric Drag. AIAA/AAS Astrodynamics Specialist Conference, (August), 2008.

[84] William B Smythe. Static and dynamic electricity. 1988.

[85] Daan Stevenson and Hanspeter Schaub. Multi-sphere method for modeling electrostatic forces and torques. Advances in Space Research, 51(1):10–20, Jan. 2013.

[86] Daan Stevenson and Hanspeter Schaub. Multi-Sphere Method for modeling spacecraft electrostatic forces and torques. Advances in Space Research, 51(1):10–20, 2013.

[87] Daan Stevenson and Hanspeter Schaub. Optimization of sphere population for electrostatic multi sphere model. IEEE Transactions on Plasma Science, 41(12):3526–3535, Dec. 2013.

[88] Daan Stevenson and Hanspeter Schaub. Terrestrial testbed for remote coulomb spacecraft rotation control. International Journal of Space Science and Engineering, 2(1):96–112, 2014.

[89] Daan Stevenson and Hanspeter Schaub. Electrostatic spacecraft rate and attitude control - experimental results and performance considerations. Acta Astronautica, 119:22–33, Feb. – March 2016.

[90] K R Svenes and J Treim. Laboratory simulation of vehicle-plasma interaction in low Earth orbit. 42(1), 2007.

[91] T.S.E Thomas. The Capacitance of an Anchor Ring. Australian Journal of Physics, 7:347, 1954.

[92] Zach Ulibarri, Jia Han, Mihály Horányi, Tobin Munsat, Xu Wang, Guy Whittall-Scherfee, and Li Hsia Yeo. A large ion beam device for laboratory solar wind studies. Review of Scientific Instruments, 88(11):115112, 2017.

[93] Hideyuki Usui, Yohei Miyake, Wojciech J Miloch, and Keisuke Ito. Numerical study of plasma depletion region in a satellite wake. IEEE Transactions on Plasma Science, 2019.

[94] Harsh Vasavada and Hanspeter Schaub. Analytic solutions for equal mass four-craft static coulomb formation. Journal of the Astronautical Sciences, 56(1):7–40, January–March 2008.

[95] ML Vestal, CR Blakley, and JH Futrell. Crossed-beam measurements of differential cross sections for elastic scattering and charge exchange in low-energy ar+-ar collisions. Physical Review A, 17(4):1337, 1978.

[96] Joseph Wang and DE Hastings. Ionospheric plasma flow over large high-voltage space platforms. ii: The formation and structure of plasma wake. Physics of Fluids B: Plasma Physics, 4(6):1615–1629, 1992.

[97] Shuquan Wang and Hanspeter Schaub. Electrostatic spacecraft collision avoidance using piece-wise constant charges. AIAA Journal of Guidance, Control, and Dynamics, 33(2):510–520, Mar.–Apr. 2010.

[98] Shuquan Wang and Hanspeter Schaub. Coulomb control of nonequilibrium fixed shape triangular three-vehicle cluster. AIAA Journal of Guidance, Control, and Dynamics, 34(1):259–270, February 2011.

[99] Kieran T. H. Wilson, Miles Bengtson, and Hanspeter Schaub. X-ray spectroscopic determination of electrostatic potential and material composition for spacecraft: Experimental results. Space Weather, 18(4):1–10, April 2020.

[100] Fuzhen Zhang. The Schur complement and its applications, volume 4. Springer Science & Business Media, 2006.

[101] Fredy R Zypman. Off-axis electric field of a ring of charge. American journal of physics, 74(4):295–300, 2006.